Fermilab

FERMILAB-THESIS-2003-06

SEARCH FOR NEW PARTICLES DECAYING TO TWO-JETS WITH THE DØ DETECTOR

By

CHRISTINA LEE HÉBERT

Submitted to the
Department of Physics and Astronomy
and the Faculty of
The Graduate School of the University of Kansas
in partial fulfillment of the
requirements for the degree of
Doctor of Philosophy

Professor Philip Baringer
Committee Chair

Professor David Lerner
Outside Committee Member

Associate Professor David Besson
Committee Member

Professor Robin Davis
Committee Member

Professor Douglas McKay
Committee Member

Assistant Professor Graham Wilson
Committee Member

Date Submitted: _____

ABSTRACT

SEARCH FOR NEW PARTICLES DECAYING TO TWO-JETS WITH THE DØ DETECTOR

Name: Christina Lee Hébert, Ph.D.
Department: Department of Physics and Astronomy
Term Degree Awarded: May, 2003
University of Kansas

Production of hadronic jets is the dominant contribution to high transverse momentum (p_T) processes in proton-antiproton $p\overline{p}$ collisions. The high (p_T) jets produced by these processes are described by perturbative Quantum Chromodynamics (QCD). Although, the Standard Model does an excellent job of explaining the current state of particle physics, there are many extensions to this model that predict the existence of new massive objects (excited quarks, W' and Z') which couple to quarks and gluons and will form resonant structures in the two jet (dijet) mass spectrum.

The data used in this search is the well understood dijet mass spectrum taken during the 1992–93 and 1994–95 running periods at DØ with an integrated luminosity of 109 pb^{-1} and a center of mass energy of 1.8 TeV. The data was corrected back to the particle level to be compared with Monte Carlo simulated signal (excited quark, W' and Z') models and background (two jet QCD events) model. The signal and background models are corrected for detector resolution effects. A probability distribution for the predicted signal cross section, σ_x, is obtained using Bayesian statistics and a 95% confidence limit is calculated.

We exclude at the 95% confidence level the production of excited quarks (q*) with masses below 770 GeV/c^2, an additional standard model W boson (W') with masses between 300 and 830 GeV/c^2 and an additional standard model Z boson (Z') with masses between 420 and 620 GeV/c^2.

This thesis is dedicated to Linda G. and Normand T. Hébert, a.k.a. mom and dad.

ACKNOWLEDGEMENTS

I would like to thank my family and friends for their support and friendship without which this thesis probably would never have been attempted. My mom, dad and Christopher my brother have always been there to talk to during the good times as well as the bad. I would like to thank Kari for her support as well.

I would also like to thank all of my friends through out the years. Especially, Mary Ann Harrison, Shawn Stone, Jeff McDonald, Kate Frame, Brian Connolly, Naresh, Alice Bean, Don Coppage and last but not least John Gardner.

Additionally, I thank Iain Bertram, whose work was a starting base for this analysis, for his excellent work, advise and help. I thank John Krane and Sharon Hagopian, who were instrumental in ensuring this analysis did not stall.

Finally, I would like to give a special thanks to Dr. Philip Baringer for being my advisor and friend. Your help and support during the past six years has made this thesis possible.

CONTENTS

LIST OF TABLES

LIST OF FIGURES

CHAPTER 1

THE STRUCTURE OF MATTER

The notion that matter is composed of smaller more elementary pieces is not new. Leucippus and his student Democritus proposed that matter consisted of non-divisible bits of matter called atoms in the fifth century B.C.E.. This idea remained purely philosophical until the early 19th century when Dalton developed his ideas on chemical atomic theory. Dalton surmised that chemical elements are made of atoms, atoms of an element are identical in mass, different elements have different atomic masses and atoms combine in whole number ratios. Elements were organized into a periodic table by Dmitri Mendeleev in 1869 which predicted the existence of additional elements. By 1900 there were over 80 known elements which suggested atoms were not the fundamental particles of Leucippus and Democritus.

By 1897, the idea that atoms were indivisible was proven incorrect with the discovery of electrons by J. J. Thomson. Thomson showed that cathode rays were negatively charged particles and that they had a mass to charge ratio $(m/e) = 0.50 \times 10^{-7}$. Comparing this (m/e) to the hydrogen ion with a (m/e) of 1×10^{-4} he showed that the electron had a mass 5×10^{-4} of the hydrogen ion [1] or around .469 MeV/c^2, the current experimental value for the mass of the electron is .511 MeV/c^2 [2]. Thomson was able to liberate light weight negatively charged particles from initially neutral atoms with a positive much heavier remainder, which was determined by Rutherford in 1911 to be the

nucleus. Rutherford realized that the compact positively charged nucleus was surrounded by electrons.

The nucleus was shown to have constituent neutrons by James Chadwick in 1932 and within that same year Enrico Fermi associated β decay with neutron decay which produces a proton, an electron and an anti-neutrino. By 1938 Meitner, Hahn and Strassman showed that nuclei of heavy elements may capture neutrons, become unstable and undergo fission. With the discovery of anti-particles by Dirac and Anderson and the discovery of muons five years later the number of "elementary" particles grew rapidly.

In an attempt to organize these particles they were classified into leptons (light weight), mesons (medium weight) and baryons (heavy weight). Murray Gell-Mann organized these further in 1961 with his Eightfold Way, reminiscent of the periodic table for the elements. Zweig and Gell-Mann postulated that hadrons (mesons and baryons) were composite particles made of quarks which have fractional charge and explain the decay modes of the hadrons.

Currently, there are six quark flavors. Each flavor can be one of three colors. Color was proposed to eliminate Pauli exclusion rule violations within hadrons. For example, a Δ^{++} is composed of three up quarks each with spin 1/2 within a distance of 10^{-15} m but the exclusion principle is maintained since each flavor of up quark has a different color. There are four fundamental forces of nature: strong, electromagnetic, weak and gravitational. These forces are mediated by bosons or force carriers.

The Standard Model encompasses three of the four fundamental forces of nature, see Table 1.1 for properties of the fundamental forces. Unfortunately, the Standard model is unable to unify gravity with the rest of the fundamental forces. Grand unified theories (GUT's) attempt to rectify this shortcoming, some of which predict extended heavy bosons. Additionally, the Standard Model fails

to explain the number of fundamental quark families which indicates that quarks may not be fundamental particles.

An excellent review of the history of particle physics can be found in these References [3].

The next section in this Chapter will discuss the Standard Model and subsequent sections will outline extended bosons and composite quark or "excited quark" models used in this analysis. This chapter will set the theoretical basis for the rest of the analysis. Chapter 2 will discuss the experimental setup of the DØ detector and the accelerator facility at the Fermi National Laboratory. Chapter 3 will expound on the notion of jets how they are measured in the detector and how they are corrected back to the particle level. Chapter 4 will discuss in detail the dijet mass data used in the search. Chapter 5 will discuss the Monte Carlo simulations of the background and the signal models in more detail, it will also discuss the detector resolution smearings applied to these simulations. Chapter 6 will discuss the confidence limit calculations and present results on the limits.

1.1 The Standard Model

The Standard Model states that matter is made up of quarks and leptons whose interactions are mediated by the strong, electromagnetic and weak forces. The quarks and leptons are known as fermions and have half integer spin and the force carriers are known as bosons and have integer spins. There are six quark and six lepton flavors. The leptons and quarks are broken down into three generations as follows:

$$\begin{pmatrix} u \\ d \end{pmatrix} \begin{pmatrix} c \\ s \end{pmatrix} \begin{pmatrix} t \\ b \end{pmatrix}$$
$$\begin{pmatrix} e \\ \nu_e \end{pmatrix} \begin{pmatrix} \mu \\ \nu_\mu \end{pmatrix} \begin{pmatrix} \tau \\ \nu_\tau \end{pmatrix} \tag{1.1}$$

All matter is composed of these quarks and their antimatter counterparts. For example, the proton is composed of two up quarks and one down quark (uud). In order for the proton to have a charge of +1 the quarks must have fractional charge.

Standard Model interactions are invariant under action of the $SU(3)_C \times SU(2)_L \times U(1)_Y$ gauge group. The electromagnetic and weak forces are unified in the electroweak gauge group, $SU(2)_L \times U(1)_Y$. The $SU(3)_C$ gauge group governs the strong portion of the theory. These forces are mediated by the bosons; γ, $W^{\pm}$, Z^0 and gluons. Additionally, there is a scalar boson, the Higgs, H^0, which is necessary to account for the masses of the fermions and the vector bosons. See tables 1.2 and 1.3 for a list of parameters for the fermions and bosons. The theory of electromagnetic phenomena is known as Quantum Electro Dynamics or QED. The unified electromagnetic and weak theory is known as the electroweak theory. The theory of strong force phenomena is known as Quantum Chromo-Dynamics or QCD.

1.1.1 Feynman Diagrams

Quarks interact primarily through the strong force, but they also may undergo weak and electromagnetic interactions. Charged leptons interact through the electromagnetic and weak forces. The neutrinos only interact through the weak force. The rules that limit the possible interactions can be described by Feynman diagrams.

The Fundamental Forces of Nature

Force	Carrier	Range	Strength
Strong	gluon	10^{-13} cm	10
Electromagnetic	photon	∞	10^{-2}
Weak	$W^{\pm}$, Z	10^{-16} cm	10^{-13}
Gravitational	graviton	∞	10^{-42}

Table 1.1. Listed are the fundamental forces of nature with ranges and relative strengths [4]. The "strength" of the force is an ambiguous notion, it depends on the nature of the source and distance from the source. Numbers in this table should not be taken too literally.

Consider, a typical Quantum Electrodynamic (QED) Feynman vertex, where two fermion lines meet a photon line. Let the fermion lines represent an electron and a positron. In Figure 1.1, Diagram one represents an electron and positron annihilating to form a photon and Diagram two represents an electron interacting via a virtual photon with another electron. In both cases time flows to the right. Particles with arrows facing backward in time are anti-particles. Figure 1.2 shows the basic symbols for Feynman diagrams. Note that in both of these figures the photon, γ, can be replaced by a Z vector boson and you have an electroweak interaction.

1.1.2 The Electroweak Model

The $SU(2)_L \times U(1)_Y$ model unifies the electromagnetic and weak interactions in the Standard Model. The $SU(2)_L$ group describes weak isospin (T) and acts only on the left-handed fermion fields where,

$$\psi_L = \frac{1}{2}(1-\gamma^5)\psi \text{ and } \psi_R = \frac{1}{2}(1+\gamma^5)\psi, \tag{1.2}$$

where

Leptons			Quarks		
Flavor	Charge	Mass (MeV/c^2)	Flavor	Charge	Mass (MeV/c^2)
ν_e	0	$<3\times10^{-6}$	up	+2/3	1.5–4.5
e	-1	0.511	down	-1/3	5–8.5
ν_μ	0	<0.19	strange	-1/3	80–155
μ	-1	106	charm	2/3	1000–1400
ν_τ	0	<18.2	bottom	-1/3	4000–4500
τ	-1	1777	top	+2/3	174300 ± 5100

Table 1.2. Listed are the Standard Model fermions (e.g. spin 1/2 particles) with their electric charge and mass [2].

The Standard Model Bosons

Force Carriers		
Name	Charge	Mass (GeV/c^2)
Photon (Electromagnetic)	0	0
$W^{\pm}$ (Weak)	±1	80.423 ± 0.039
Z^0 (Weak)	0	91.1876 ±0.0021
gluon (Strong)	0	0

Table 1.3. Listed are the Standard Model bosons (e.g. integer spin particles) with their electric charge and mass [2]. These particles are responsible for carrying the electromagnetic, weak and strong forces. Not pictured here is the undiscovered Higgs boson.

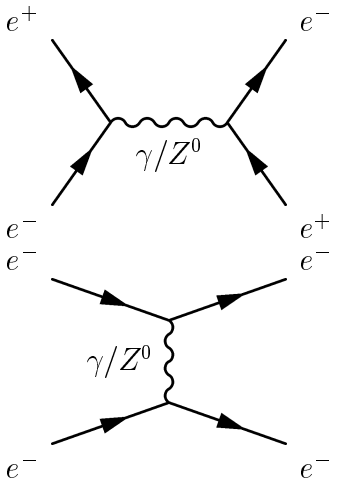

Figure 1.1. Simple QED implementation of Feynman Diagrams. s-channel top, t-channel bottom.

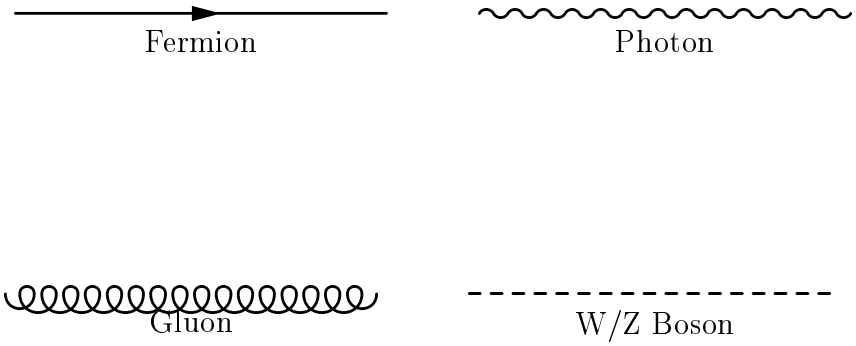

Figure 1.2. Basic Feynman symbols.

$$\gamma^5 = i\gamma^0\gamma^1\gamma^2\gamma^3, \tag{1.3}$$

and

$$\gamma^i = \begin{pmatrix} 0 & \sigma^i \\ -\sigma^i & 0 \end{pmatrix}. \tag{1.4}$$

σ^i are the Pauli matrices. Formulation of ψ_L and ψ_R in this manner preserves chiral symmetry. The fermion mass term $m\overline{\psi}\psi$ is not invariant under $SU(2)_L$ because $\overline{\psi}\psi = \overline{\psi}_L\psi_R + \overline{\psi}_R\psi_L$ so we assume massless fermions at this point.

The $U(1)_Y$ group describes weak hypercharge (Y). The electric charge (Q) is related to weak isospin and weak hypercharge by $Q = T_3 + \frac{Y}{2}$ where T_3 is the third component of weak isospin. This implies that charge is conserved in the electroweak theory.

In the $SU(2)_L \times U(1)_Y$ model quarks and leptons are assigned as left handed doublets and right handed singlets. The left handed quark doublets are

$$\psi_i = \begin{pmatrix} u_i \\ d_i' \end{pmatrix} \rightarrow \begin{pmatrix} u \\ d' \end{pmatrix}_L, \begin{pmatrix} c \\ s' \end{pmatrix}_L, \begin{pmatrix} t \\ b' \end{pmatrix}_L \tag{1.5}$$

The right handed quark singlets are

$$(u_R, c_R, t_R, d_R, s_R, b_R). \tag{1.6}$$

The left handed lepton doublets are

$$\psi_i = \begin{pmatrix} \nu_i \\ l_i \end{pmatrix} \rightarrow \begin{pmatrix} \nu_e \\ e \end{pmatrix}_L, \begin{pmatrix} \nu_\mu \\ \mu \end{pmatrix}_L, \begin{pmatrix} \nu_\tau \\ \tau \end{pmatrix}_L \tag{1.7}$$

The right handed lepton singlets (e_R, μ_R, τ_R).

The massless electroweak Lagrangian can be written as follows,

$$\mathcal{L} = -\frac{1}{4}W^{\mu\nu} \cdot W_{\mu\nu} - \frac{1}{4}B^{\mu\nu}B_{\mu\nu} + \overline{\Phi}i\gamma^\mu D_\mu\psi \tag{1.8}$$

Where

$$W_{\mu\nu} = \partial_\mu W_\nu - \partial_\nu W_\mu - gW_\mu \times W_\nu, \tag{1.9}$$

$$B_{\mu\nu} = \partial_\mu B_\nu - \partial_\nu B_\mu \tag{1.10}$$

and

$$D_\mu = \partial_\mu + igW_\mu \cdot T + i(g'/2)yB_\mu Y \tag{1.11}$$

Where g and g' are the weak charges of the $SU(2)_L \times U(1)_Y$ gauge fields and $\hat{B}^\mu$ is the hypercharge gauge field. The gauge bosons for this model are W^i_μ, $i = 1, 2, 3$ for $SU(2)_L$ and B_μ for $U(1)_Y$.

If we define the isospin raising and lowering operators as $T^\pm = \frac{(T_1 \pm iT_2)}{\sqrt{2}}$. Then $W \cdot T = W^+T^+ + W^-T^- + W_3T_3$. For the electromagnetic interaction to be unified with the weak interaction the term $ieQA$ must be incorporated into the neutral term $i(gW_{3\mu}T_3 + g'\frac{1}{2}B_\mu Y)$. This implies that the W_3 field and the B fields are linear combinations of the A and Z neutral fields such that,

$$\begin{pmatrix} W_3 \\ B \end{pmatrix} = \begin{pmatrix} \cos\theta_W & \sin\theta_W \\ -\sin\theta_W & \cos\theta_W \end{pmatrix} \begin{pmatrix} Z \\ A \end{pmatrix} \tag{1.12}$$

Where θ_W is the electroweak mixing angle. In order for $ieQA = ie(T_3 + \frac{1}{2}Y) = iA[g\sin\theta_W T_3 + g'\sin\theta_W \frac{1}{2}Y]$ then $g = \frac{e}{\sin\theta_W}$ and $g' = \frac{e}{\cos\theta_W}$. For a given θ_W all gauge couplings are determined by e, thus the weak and electromagnetic theories are unified [5].

1.1.2.1 Higgs Mechanism

This theory assumes that the $W^\pm$ and Z^0 bosons and the fermions are massless. To generate the required masses and maintain renormalizability of the gauge theory spontaneous symmetry breaking is necessary. This symmetry breaking is accomplished by the Higgs mechanism. The additions to the massless Lagrangian(Eqn. 1.8) are

$$\mathcal{L}_\Psi = |D_\mu \Psi|^2 - V(|\Psi|^2) + \mathcal{L}^F_\Psi, \tag{1.13}$$

where $|\Psi|^2$ is $\Psi^\dagger\Psi$ and $\mathcal{L}_\Psi^F$ is the Yukawa coupling of Ψ to fermions. The simplest renormalizable form of the scalar potential V is

$$V(\Psi) = -\mu^2\Psi^\dagger\Psi + h(\Psi^\dagger\Psi)^2. \tag{1.14}$$

The isodoublet is :

$$\Psi = \begin{pmatrix} \phi^+ \\ \phi^0 \end{pmatrix}. \tag{1.15}$$

If $\mu^2 > 0$ then the field Ψ will acquire a non-vanishing expectation value $|\Psi|^2$ and the symmetry of $SU(2)\times U(1)$ will be spontaneously broken. In other words the vacuum state fails to exhibit the $SU(2) \times U(1)$ symmetry.

The ground state of $|\Psi|^2$ occurs at $\Psi_0 = (\frac{\mu^2}{h})^{\frac{1}{2}}$. The field is expanded about the vacuum state and the potential is written in terms of the expansion

$$\begin{aligned} \Psi(x) &= \Psi_0 + \frac{1}{\sqrt{2}}(\Psi_1(x) + i\Psi_2(x)), \\ V(\Psi) &= -\frac{1}{2h}\mu^4 + \frac{1}{2}\cdot 2\mu^2\Psi_1^2 + \text{H.O.} \end{aligned} \tag{1.16}$$

The Lagrangian is expanded in terms of $\Psi(x)$. The fields Ψ and A_μ obtain masses in a way which preserves the renormalizabilty of the theory [5–6].

1.1.2.2 Weak Mixing and the CKM Matrix

Weak interactions of quarks do not conserve flavor. The eigenstates of weak interactions are not the same as the mass eigenstates. In the electroweak model weak eigenstates are linear combinations of the mass eigenstates such that $d_i' = \sum_j V_{ij}d_j$. Where V_{ij} is the Cabibbo-Kobayashi-Maskawa (CKM) quark mixing matrix.

$$\begin{pmatrix} d' \\ s' \\ b' \end{pmatrix} = \begin{pmatrix} V_{ud} & V_{cd} & V_{td} \\ V_{us} & V_{cs} & V_{ts} \\ V_{ub} & V_{cb} & V_{tb} \end{pmatrix} \begin{pmatrix} d \\ s \\ b \end{pmatrix} \tag{1.17}$$

The values of the individual matrix elements can be determined experimentally by the weak decays of the relevant quarks.

The standard parameterization is as follows

$$\begin{pmatrix} c_{12}c_{13} & s_{12}c_{13} & s_{13}e^{i\delta_{13}} \\ -s_{12}c_{23} - c_{12}s_{23}s_{13}e^{i\delta_{13}} & c_{12}c_{23} - s_{12}s_{23}s_{13}e^{i\delta_{13}} & s_{23}c_{13} \\ s_{12}s_{23} - c_{12}c_{23}s_{13}e^{i\delta_{13}} & -c_{12}s_{23} - s_{12}c_{23}s_{13}e^{i\delta_{13}} & c_{23}c_{13} \end{pmatrix} \tag{1.18}$$

with $c_{ij} = \cos\theta_{ij}$ and $s_{ij} = \sin\theta_{ij}$ where i=1,2,3 indicates the generation labels. θ_{12} is the Cabibbo angle and relates the mixing between generations 1 and 2. For example, if $\theta_{13} = 0$ then there is no mixing between the first and third generations. The remaining phase $e^{i\delta_{13}}$ reflects the physics of charge conjugation parity (CP) violation [2].

1.1.2.3 The Electroweak Lagrangian

The Lagrangian $\mathcal{L}$ [2] is given by:

$$\begin{aligned} \mathcal{L}_F = & \sum_i \overline{\psi}_i \left(i \not{\partial} - m_i - \frac{g m_i H}{2M_W} \right) \\ & - \frac{g}{2\sqrt{2}} \sum_i \overline{\psi}_i \gamma^\mu (1-\gamma^5)(T^+ W_\mu^+ + T^- W_\mu^-)\psi_i \\ & - e \sum_i q_i \overline{\psi}_i \gamma^\mu \psi_i A_\mu \\ & - \frac{g}{2\cos\theta_W} \sum_i \overline{\psi}_i \gamma^\mu (g_V^i - g_A^i \gamma^5)\psi_i Z_\mu \end{aligned} \tag{1.19}$$

Where $\theta_W = \tan^{-1}(\frac{g'}{g})$ is the weak angle, $e = g\sin\theta_W$ is the positron electric charge, and $A = B\cos\theta_W + W^3\sin\theta_W$ is the massless photon field. $W^\pm = (W^1 \mp iW^2)/\sqrt{2}$ and $Z = -B\sin\theta_W + W^3\cos\theta_W$ are the massive charged and neutral weak boson fields ($W^\pm, Z^0$). T^+ and T^- are the weak isospin raising and lowering operators. ψ represents the fermion fields and γ represents the Dirac matrices. The axial and vector couplings are as follows

$$g_V^i = t_{3L} - 2q_i \sin^2\theta_W, \tag{1.20}$$

$$g_a^i = t_i, \tag{1.21}$$

Where $t_{3L}(i)$ is the weak isospin of fermion i ($\frac{1}{2}$ for u_i and ν_i ; $-\frac{1}{2}$ for d_i and e_i) and q_i is the charge of the fermion in units of e. In the first term of Equation 1.19 m_i represents the quark masses (which are the running $\overline{MS}$ masses with $\mu = 2$ GeV). H is the physical neutral Higgs scalar. $\frac{gm_i}{2M_W}$ represents the Yukawa coupling of H to Ψ_i in the minimal spontaneous symmetry breaking model.

The second term in Equation 1.19 is the charged current weak interaction. For momenta small compared to M_W this term can be used to determine the effective four fermion interaction with the Fermi constant given by

$$G_F = \frac{1}{\sqrt{2}\nu^2} = \frac{g_w^2}{4\sqrt{2}M_W^2}, \tag{1.22}$$

at the lowest order in perturbation theory. The masses of the W, Z bosons and the strength of the interactions are determined by the weak isospin coupling, g_w, hypercharge coupling, g' and the vacuum expectation value for spontaneous symmetry breaking, ν. Where these constants are

$$g_W = \frac{e}{\sin\theta_W}, \tag{1.23}$$

$$g' = \frac{e}{\cos\theta_W}, \tag{1.24}$$

and

$$\nu = \frac{2M_W}{g_W}. \tag{1.25}$$

These values can conveniently be expressed as follows

$$\alpha_{em} = \frac{e^2}{4\pi} = \frac{1}{4\pi}\left(\frac{1}{\frac{1}{g_w^2} + \frac{1}{g'^2}}\right), \tag{1.26}$$

and using the well known fine structure constant(α) and Fermi coupling constant(G_F) [2], respectively

$$\begin{aligned} \alpha &= 1/137.03599976(50)(Q^2 = m_e^2) \\ G_F &= 1.16637(1) \times 10^{-5} GeV^{-2}, \end{aligned} \tag{1.27}$$

with

$$\sin^2\theta_W = 1 - \frac{M_W^2}{M_Z^2} \tag{1.28}$$

and $\sin^2\theta_W = 0.23143(15)$ [2], one can obtain to leading order the M_W and M_Z masses [7].

$$\begin{aligned} M_W &= \sqrt{\frac{\pi\alpha}{G_F\sqrt{2}}}\frac{1}{\sin\theta_W} \approx 78 GeV \\ M_Z &= \frac{M_W}{\cos\theta_W} \approx 89 GeV \end{aligned} \tag{1.29}$$

1.1.3 Quantum Chromodynamics (QCD)

Quantum Chromodynamics (QCD) describes strong interactions by a local non-Abelian gauge theory of quarks and gluons. $SU(3)$ is the gauge group and gluons are the gauge bosons. The Lagrangian is

$$\begin{aligned} L_{QCD} = -\frac{1}{4}F^{(a)}_{\mu\nu}F^{(a)\mu\nu} + i\sum_q \overline{\psi}^i_q \gamma^\mu (D_\mu)_{ij}\psi^j_q \\ - \sum_q m_q \overline{\psi}^i_q \psi_{qi}, \end{aligned} \tag{1.30}$$

The second term represents the quark-gluon interactions where $\psi^i_q(x)$ are the 4-component Dirac spinors associated with each quark field of color i and flavor q. The quark triplets are

$$\begin{pmatrix} u_r \\ u_b \\ u_g \end{pmatrix}, \begin{pmatrix} c_r \\ c_b \\ c_g \end{pmatrix}, \begin{pmatrix} t_r \\ t_b \\ t_g \end{pmatrix}, \begin{pmatrix} d_r \\ d_b \\ d_g \end{pmatrix}, \begin{pmatrix} s_r \\ s_b \\ s_g \end{pmatrix} \begin{pmatrix} b_r \\ b_b \\ b_g \end{pmatrix} \tag{1.31}$$

In equation 1.30

$$F^{(a)}_{\mu\nu} = \partial_\mu A^a_\mu - \partial_\nu A^a_\nu - g_s f_{abc} A^b_\mu, \tag{1.32}$$

$$(D_{\mu\nu})_{ij} = \delta_{ij}\partial_\mu + i g_s \sum_a \frac{\lambda^a_{i,j}}{2} A^a_\mu, \tag{1.33}$$

where g_s is the QCD coupling constant which determines the strength of interaction between colored quanta and the f_{abc}'s are the structure constants of the SU(3) algebra [2]. A^a_μ are the gluon fields which have eight color degrees of freedom and can be expressed as follows [4]

$$\begin{aligned}
|1> &= \frac{(r\overline{b} + b\overline{r})}{\sqrt{2}} & |5> &= -i\frac{(r\overline{g} + g\overline{r})}{\sqrt{2}} \\
|2> &= \frac{(b\overline{g} + g\overline{b})}{\sqrt{2}} & |6> &= -i\frac{(r\overline{b} + b\overline{r})}{\sqrt{2}} \\
|3> &= \frac{(r\overline{r} + b\overline{b})}{\sqrt{2}} & |7> &= -i\frac{(b\overline{g} + g\overline{b})}{\sqrt{2}} \\
|4> &= \frac{(r\overline{g} + g\overline{r})}{\sqrt{2}} & |8> &= \frac{(r\overline{r} + b\overline{b} + g\overline{g})}{\sqrt{6}}
\end{aligned} \tag{1.34}$$

The third term on the right hand side of equation 1.32 is the non-Abelian term which distinguishes QCD from QED, giving rise to triplet and quartic gluon self-interactions and ultimately to asymptotic freedom [8].

Equations 1.30, 1.32 and 1.33 can be used to derive the Feynman rules of perturbative QCD, see Figure 1.3 for these rules.

1.1.3.1 The Running Coupling Constant

Asymptotic freedom and quark confinement can be expressed in terms of the strong coupling constant(α_s), where

$$\alpha_s = \frac{g^2}{4\pi}. \tag{1.35}$$

The perturbative calculation of the theory requires renormalization to remove ultraviolet divergences. This renormalization procedure introduces a renormal-

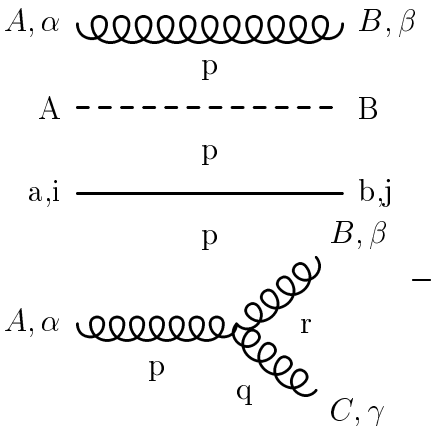

$$\delta^{AB}[-g^{\alpha\beta}+(1-\lambda)\frac{p^\alpha p^\beta}{p^2+i\epsilon}]\frac{i}{p^2+i\epsilon}$$

$$\delta^{AB}\frac{i}{p^2+i\epsilon}$$

$$\delta^{ab}\frac{i}{\hat{p}-m+i\epsilon}$$

$$-g_s f_{ABC}[g^{\alpha\beta}(p-q)^\gamma+g^{\beta\gamma}(q-r)^\alpha+g^{\gamma\alpha}(r-p)^\beta]$$

(all incoming momentum)

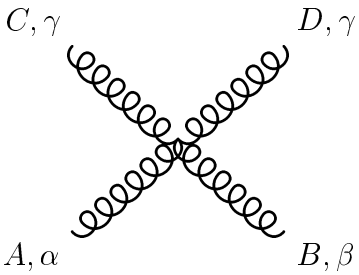

$$-ig_s^2 f^{XAC}f^{XBD}(g_{\alpha\beta}g_{\alpha\gamma}-g_{\alpha\delta}g_{\beta\gamma})$$

$$-ig_s^2 f^{XAD}f^{XBC}(g_{\alpha\beta}g_{\alpha\gamma}-g_{\alpha\gamma}g_{\beta\delta})$$

$$-ig_s^2 f^{XAB}f^{XCD}(g_{\alpha\gamma}g_{\beta\delta}-g_{\alpha\delta}g_{\beta\gamma})$$

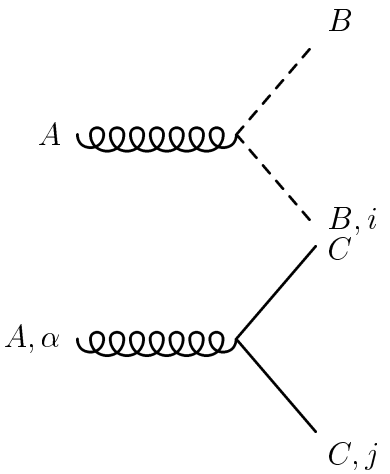

$$g_s f^{ABC}q^\alpha$$

$$-ig_s(t^A)_{cb}(\gamma^\alpha)_{ji}$$

Figure 1.3. Feynman rules for QCD in a covariant gauge, where the dashed line represents the ghost propagator.

Figure 1.4. Graphs which contribute to the β function in the one loop approximation.

ization scale (μ). The renormalization scale dependence of α_s is controlled by the β-function:

$$\mu\frac{\partial\alpha_s}{\partial\mu} = -\frac{\beta_0}{2\pi}\alpha_s^2 - \frac{\beta_1}{4\pi^2}\alpha_s^3 - \frac{\beta_2}{64\pi^3}\alpha_s^4 - ..., \tag{1.36}$$

$$\beta_0 = 11 - \frac{2}{3}n_f, \tag{1.37}$$

$$\beta_1 = 51 - \frac{19}{3}n_f, \tag{1.38}$$

$$\beta_2 = 2857 - \frac{5033}{9}n_f + \frac{325}{27}n_f^2; \tag{1.39}$$

where n_f is the number of quarks with mass less than the energy scale μ. In solving the differential equation a constant of integration is introduced(μ_0). μ_0 is commonly chosen at $\mu_0 = M_Z$ [2]. This constant (μ_0) is the one fundamental constant of QCD that must be determined from experiment. Figure 1.4 shows one loop approximation Feynman diagrams that contribute to the β function.

After solving this equation

$$\alpha_s(Q) = \frac{\alpha_s(\mu^2)}{1 + \frac{\alpha_s(\mu^2)}{12\pi}(11c - 2n_f)\log\frac{Q^2}{\mu^2}}, \tag{1.40}$$

where Q is the magnitude of the momentum transferred in the interaction and c is the number of quark colors. By introducing the renormalization scale (μ),

divergent Feynman integrals either become finite or vanish. The renormalization scale can differ for each divergent diagram. In perturbative QCD calculations, the minimal subtraction scheme (MS) requires a constant μ for all diagrams and usually $\mu \propto Q$. QCD predictions in this analysis employ a modified minimum subtraction scheme ($\overline{MS}$). The strong coupling constant can be expressed as follows [9]

$$\alpha_s(Q^2) = \frac{12\pi}{(11c - 2n_f)\log\frac{Q^2}{\Lambda^2}}, \tag{1.41}$$

where

$$\Lambda^2 = \mu^2 \exp\frac{-12\pi}{(11c - 2n_f)\alpha_s(\mu^2)}. \tag{1.42}$$

Figure 1.5 [10] shows the running behavior of α_s. For $Q^2 > 15\ GeV^2$, $\alpha_s \approx 0.1$ and perturbative QCD expansion in terms of α_s becomes valid. This indicates that QCD is asymptotically free at high energies or short distances (10^{-15}m).

Asymptotic freedom is attributed to the self interaction of the gluon field. The idea is that the emission of virtual gluons by static color sources causes their color charges to leak out into the vacuum. The interaction between charges is weaker when charge distributions overlap which leads to a reduction of the color force at short distances [8]. For more information on this see reference [11].

1.1.3.2 QCD Two Jet Production

During high energy collisions of the proton and anti-proton, quarks and gluons are produced. Quarks and gluons are asymptotically free during the hard collision allowing quarks and gluons from the proton and anti-proton to interact. Asymptotic freedom results from the fact that the strong coupling constant α_s is small and QCD is a perturbative theory. At short distances from the collision, typically the size of a hadron, α_s increases enough to spontaneously

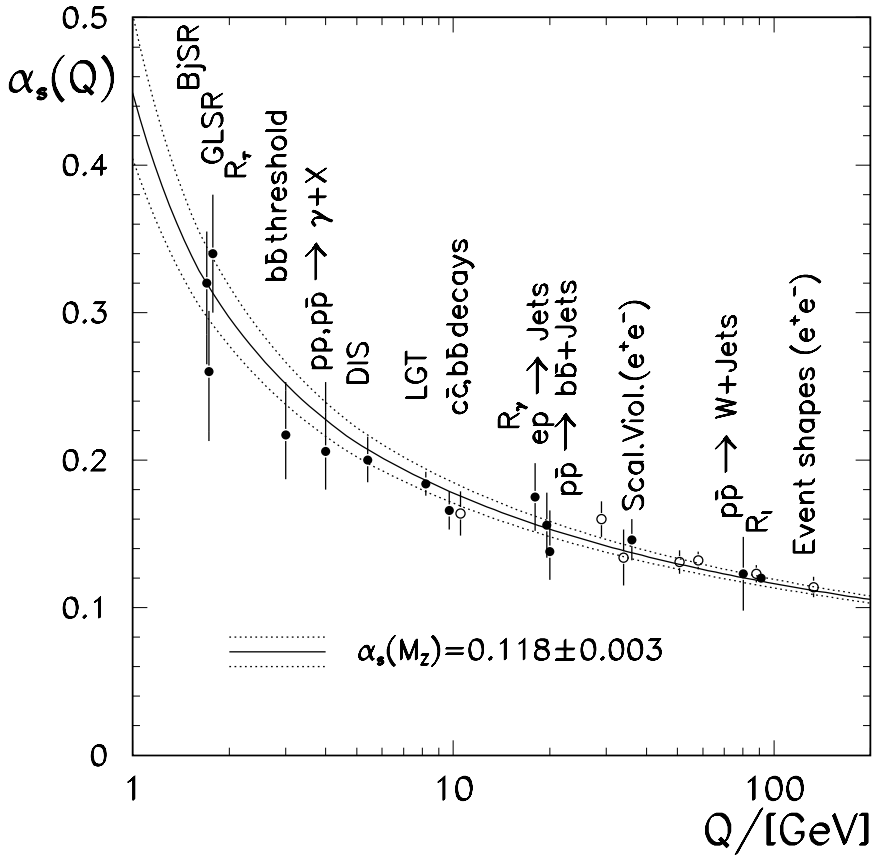

Figure 1.5. Running QCD coupling from reference [10]

create many new gluons and quark- anti-quark pairs. This process is known as parton showering.

The $p\overline{p}$ cross section for two jet production is as follows,

$$\sigma(P_1, P_2) = \sum_{i,j} \int dx_i dx_j f_i(x_1, \mu) \hat{\sigma}_{ij}(p_1, p_2, \alpha_s(\mu), Q). \tag{1.43}$$

Where the momenta of the proton and antiproton are given by P_1 and P_2, the momenta of the interacting partons are given by $p_1 = x_1 P_1$ and $p_2 = x_2 P_2$ where x_i is the momentum transfered from the proton (or anti-proton) to the constituent colliding partons. Transverse jet energies for quarks and gluons at $\sqrt{s} = 1.8$ TeV at $\eta_1, \eta_2 = 0$ are plotted in Figure 1.6. Transverse energy of the jet is related to transverse momentum transfer by, $X_T = \frac{2E_T}{\sqrt{s}}$. The characteristic scale of the hard scattering is given by Q. The functions $f_i(x_1, \mu)$ are the QCD

quark or gluon structure functions for the hadrons (proton or anti-proton) in the interaction. These structure functions are called the hard scattering coefficients. μ is the factorization scale. The cross section of an interaction between partons i and j is given by $\hat{\sigma}$. The scale μ is chosen to reflect the the Q scale of the interaction. The strong coupling constant is small at high values of Q and it is possible to use perturbative QCD to calculate the cross section given by (1.43). The dependence of the perturbative expansion on μ decreases as the number of expansion terms increases. In other words, next to leading order calculations (NLO) are better than leading order calculations [9, 7].

If the Q scale of the reaction is not high enough, the structure function must include non-perturbative effects parameterized by a parton distribution function (PDF). The boundary between the hard-scattering coefficient and the PDF reflects the boundary between short distance effects and long distance effects. This scale is set with factorization scale μ_f. The factorization scale isolates the non-perturbative cross section contributions (PDF) from the perturbative portion of the hard scattering coefficient [9].

A PDF describes the probability to observe a specific parton of a given momentum. The PDF depends on the initial parton and must be determined by experiment. PDF's depend on renormalization scale μ, strong coupling constant $\alpha_s(\mu)$ and the order of the theoretical calculation. PDF's use results from preceding experiments.

After a hard collision one parton from the incoming proton and one parton from the incoming antiproton scatter and produce two high P_T partons which fragment and produce jets, see Figure 1.7 for a representation of this process. These jets are produced with equal and opposite momenta in the center-of-mass frame of the interacting partons. If only two partons are produced and the

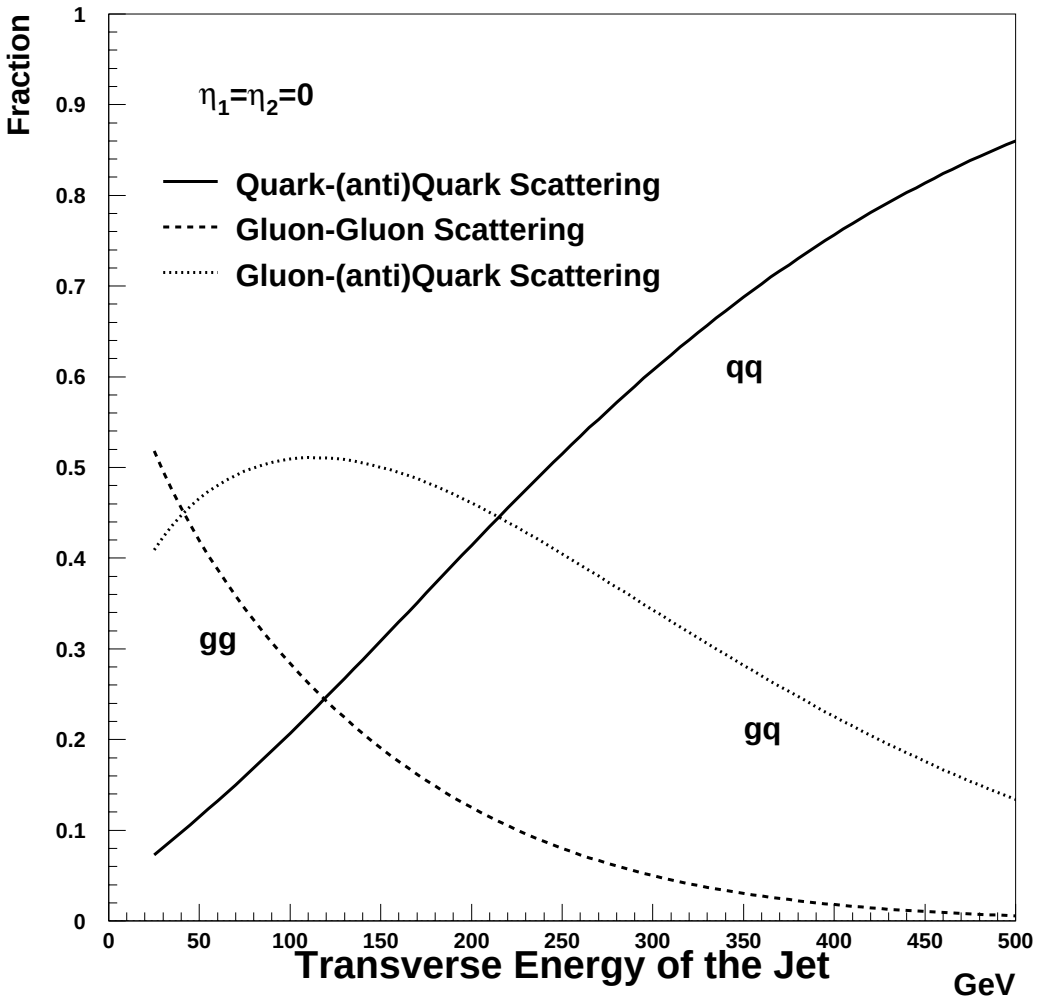

Figure 1.6. Transverse energy of jets for $\sqrt{s} = 1.8$ TeV with $\eta_1 = \eta_2 = 0$.

incoming transverse momentum of the initial partons is ignored then the two jets will be back to back in azimuth and balanced in E_T in the lab frame.

The cross section for a $2 \to 2$ process is as follows

$$\frac{E_3 E_4 d^6\hat{\sigma}}{d^3p_3 d^3p_4} = \frac{1}{2\hat{s}} \frac{1}{16\pi^2} \sum |M|^2 \delta^4(p_1 + p_2 - p_3 - p_4), \tag{1.44}$$

where M is the leading order matrix element for the process, see Table 1.4. We define $\hat{s} = (p_1 + p_2)^2$, $\hat{t} = (p_1 + p_3)^2$ and $\hat{u} = (p_2 - p_3)^2$. See Figure 1.8 for leading

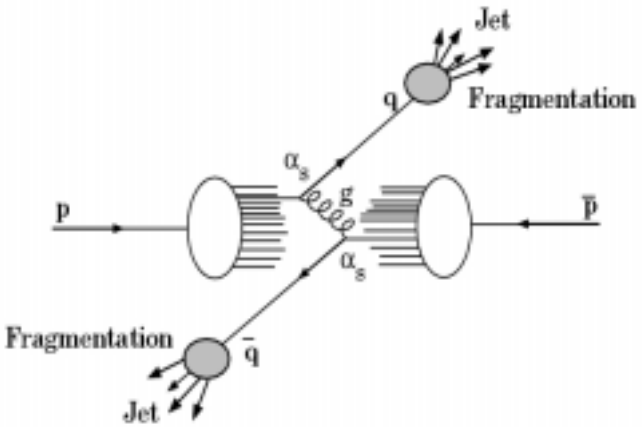

Figure 1.7. A diagram of a proton–antiproton interaction resulting in two jets

Lowest Order Matrix Elements

Process	$\sum \lvert M\rvert^2/g^4$
$q\overline{q} \to q'\overline{q}'$	$\frac{4}{9}\frac{u^2+t^2}{s^2}$
$q\overline{q} \to q\overline{q}$	$\frac{4}{9}(\frac{u^2+t^2}{s^2} + \frac{u^2+s^2}{t^2}) - \frac{8}{27}\frac{u^2}{st}$
$qg \to qg$	$\frac{u^2+s^2}{t^2} - \frac{4}{9}\frac{u^2+s^2}{su}$
$gg \to gg$	$\frac{9}{2}(3 - \frac{ut}{s^2} - \frac{us}{t^2} - \frac{ts}{u^2})$

Table 1.4. Lowest order matrix elements.

order Feynman diagrams describing the $2 \to 2$ processes. Notice that t-channel processes dominate. The discussion of jets will continue in Chapter 4 [7].

1.2 Beyond the Standard Model

Although, the Standard Model (SM), $SU(3) \times SU(2)_L \times U(1)_Y$, agrees well with experimental data many believe that it is inadequate since it fails to unify the fundamental forces, and contains many parameters and features that are incorporated into the theory by hand. Since the failure of the simplest grand

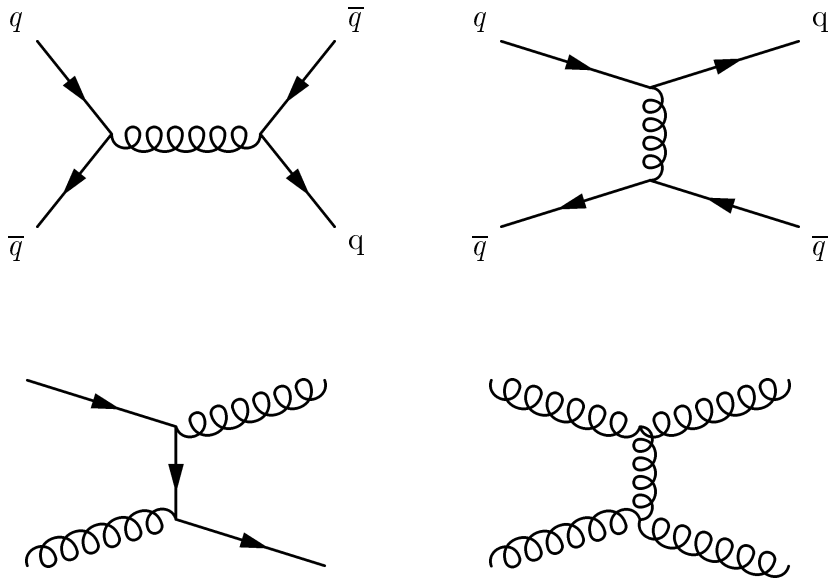

Figure 1.8. Leading order Feynman diagrams for two jet processes at the Tevatron.

unified theory (GUT), $SU(5)$, to deal with the many theoretical difficulties of the SM and to agree with experimental results for the proton lifetime and the electroweak mixing angle theorists have turned to higher order symmetries such as SO(10) and E_6 [12]. These models predict additional heavy vector bosons (W', Z').

The Standard Model assumes that fermions are the fundamental particles of nature. Many have questioned this assumption due to the number of fermion families and the fact that the top quark has a mass close to that of a gold atom.

1.2.1 Heavy Vector Boson (W',Z') Model

W' and Z' production is calculated using the extended model explained in reference [13]. This model assumes that the W' and Z' are heavier versions of the Standard Model W and Z bosons. The W' and Z' have the same vertex couplings as the Standard Model W and Z ($Wq\overline{q}$ and $Wl\nu$) except the triple gauge couplings ($W \rightarrow WZ$ and $Z \rightarrow WW$) are modified by a factor $\xi \propto \frac{M_W^2}{M_Z^2}$.

Without ξ the decay widths for WW and WZ would increase as $M_{W,Z}^5$. ξ ensures that this dependence is only of order M_V. With this feature in place, the branching ratio for ZW and WW remains below 0.02 and is too small to study at the Tevatron. All fermions are the same as their Standard Model counterparts.

1.2.1.1 W and Z Production Cross Section

The W' and Z' production cross sections for the extended model vector bosons are calculated in the same manner as the Standard Model versions. The W and Z production cross section at the Born level can be derived from the equation(1.43) as follows:

$$\sigma_{p\overline{p}\to V} = \int dx_q dx_{\overline{q}'} f_q(x_q,\mu) f_{\overline{q}}(x_{\overline{q}'},\mu)\hat{\sigma}_{\overline{q}' q\to V} \tag{1.45}$$

where the process cross sections are given by [2, 7]

$$\hat{\sigma}_{\overline{q}' q\to W} = \frac{\pi}{3}\sqrt{2}G_F M_W^2 |V_{qq'}|^2 \delta(\hat{s} - M_W^2) \tag{1.46}$$

$$\hat{\sigma}_{\overline{q}q\to Z} = \frac{\pi}{3}\sqrt{2}G_F M_Z^2 (V_q^2 + A_q^2)\delta(\hat{s} - M_Z^2) \tag{1.47}$$

1.2.1.2 W and Z Decays

To leading order in electroweak theory the partial decay widths for gauge bosons decaying to quarks, u_i and $\overline{d}_i$ are as follows [2],

$$\Gamma(W^{\pm} \to u_i \overline{d}_i) = \frac{C G_F M_W^3}{6\sqrt{2}\pi} |V_{ij}|^2 \approx (707 \pm 1)|V_{ij}|^2 MeV \tag{1.48}$$

$$\Gamma(Z \to u_i \overline{u}_i) = \frac{C G_F M_Z^3}{6\sqrt{2}\pi} [g_V^{i2} + g_A^{i2}] \tag{1.49}$$

For quarks $C = 3(1 + \alpha_s(M_V)/\pi + 1.409\alpha_s^2/\pi^2 - 12.77\alpha_s^3/\pi^3)$.

Decay Mode	$\frac{\Gamma}{\sum\Gamma}$ (%)
$l^+\nu$	10.68±0.12
$e^+\nu$	10.72±0.16
$\mu^+\nu$	10.57±0.22
$\tau^+\nu$	10.74±0.27
hadrons	67.96±0.35

Table 1.5. Branching fractions for W^+ decay modes [2].

These width relations can be used to determine the branching fractions (BF) for each decay mode, by simply counting the possible decay modes of W as follows

$$\begin{aligned} BF(W \to e\nu) &= \frac{\Gamma_W \to e\nu}{\Gamma_{total}} \approx 11.1\% \\ BF(W \to \sum_i l_i\overline{\nu_i}) &\approx 33.3\% \\ BF(W \to \overline{q}q') &\approx 66.6\%. \end{aligned} \tag{1.50}$$

The branching fractions for the Z are complicated by the vector and axial coupling (V+A). If one assumes $\sin^2\theta_W = 0.23$ [7] then

$$\begin{aligned} BF(Z \to \sum_i l_i\bar{l}_i) &\approx 10.2\% \\ BF(Z \to \sum_i \nu_i\overline{\nu_i}) &\approx 20.4\% \\ BF(Z \to \overline{q}q) &\approx 69.2\%. \end{aligned} \tag{1.51}$$

These estimates agree reasonably well with the current experimental results. The branching fractions for W' and Z' should be identical to the W and Z branching fractions. The decays $W' \to q\overline{q'}$ and $Z' \to q\overline{q}$. See Tables 1.5 and 1.6 for a listing of experimental results.

Decay Mode	$\frac{\Gamma}{\sum\Gamma}$ (%)
l^+l^-	3.3658±0.0023
e^+e^-	3.363± 0.004
$\mu^+\mu^-$	3.366± 0.007
$\tau^+\tau^-$	3.370± 0.008
$\sum \nu_i\overline{\nu}_i$	20.00± 0.06
hadrons	69.91± 0.06

Table 1.6. Branching fractions for Z decay modes [2].

1.2.2 Excited Quark Model

The Standard Model assumes that quarks are fundamental objects without internal structure. The fact that there are three generations of fermions suggests that quarks may not be fundamental particles, just as the proliferation of elements and hadrons ushered in the concepts of atomic and hadronic structure. The model used here assumes that new fundamental particles (preons) within the quark are governed by a new non-abelian strong interaction (Metacolor) that is asymptotically free within the quark. These preons manifest themselves as quarks and leptons below some characteristic energy scale (Λ_C). Currently, DØ results [14] give the constraint $\Lambda_C > 2.0$ TeV at 95 % Confidence Level.

1.2.2.1 Model Setup

There are numerous models for an excited quark theory. The model used here is described in the papers by Baur *et al.* [15]. In this model the spin and isospin of the excited fermions will be set to $\frac{1}{2}$ to limit the number of parameters. The assignment of left and right-handed components to isodoublets for the first generation is as follows:

$$\begin{bmatrix} u_i \\ d_i \end{bmatrix}, \; u_R \qquad \begin{bmatrix} u^* \\ d^* \end{bmatrix}_L, \begin{bmatrix} u^* \\ d^* \end{bmatrix}_R \tag{1.52}$$

which allows for non-zero masses prior to $SU(2) \times U(1)$ symmetry breaking. See Figure 1.9 for an illustration of the allowed couplings before symmetry breaking.

The coupling of the excited fermion states f^* to gluons, γ, $W^{\pm}$, and Z is given by the Lagrangian:

$$\mathcal{L}_{gauge} = \overline{f}^* \gamma^\mu \left[g_s \frac{\lambda^a}{2} G^a_\mu + g_w \frac{\tau}{2} \cdot W_\mu + g'_W \frac{Y}{2} B_\mu \right] f^* \tag{1.53}$$

The weak hypercharge Y of the excited states is -1 and $\frac{1}{3}$ in the lepton quark sector respectively; g_s, $g_W = \frac{e}{\sin\theta_W}$ and $g'_W = \frac{e}{\cos\theta}$ are the strong and electroweak gauge couplings. G^a_μ, W_μ and B_μ describe the gluon, $SU(2)$ and $U(1)$ gauge fields.

Gauge bosons can also mediate transitions between ordinary (left-handed) and excited (right-handed) fermions. The effective Lagrangian describing these transitions is given by:

$$\mathcal{L}_{transition} = \frac{1}{2\Lambda_C} \overline{f}^*_R \sigma^{\mu\nu} \left[g_s f_s \frac{\lambda^a}{2} G^a_{\mu\nu} + g_W f \frac{\tau}{2} \cdot W_{\mu\nu} + g'_W f' \frac{Y}{2} B_{\mu\nu} \right] f_L + H.C. \tag{1.54}$$

where $G^a_{\mu\nu}$, $W_{\mu\nu}$ and $B_{\mu\nu}$ are the field strength tensors of the gluon, SU(2) and U(1) gauge fields. f_s, f and f' are parameters determined by the composite dynamics. For a purely strong interaction these will be set to 1. Higher dimension interactions can be considered by transforming f_s, f and f' to form factors such as $f_s(Q^2)$.

Excited fermions may also interact with ordinary fermions via contact interactions resulting from strong preon interactions but these interactions produce multijet events and are not studied in this analysis.

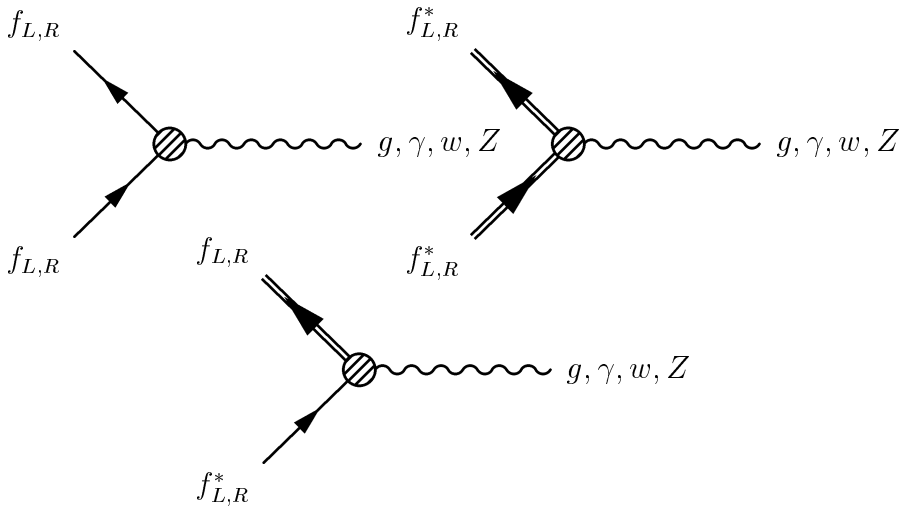

Figure 1.9. (Top) Gauge interactions of the light and excited fermions. The W boson couples to the left and right-handed excited fermions but only to the left-handed Standard Model fermions. (Bottom) Transitions between ordinary and excited fermions through gauge-boson emission.

1.2.3 Widths of the Excited Quarks

Heavy excited fermions can decay into light fermions plus gauge bosons and into quarks and leptons through preon pair creation. Assuming $m^* > m(W, Z)$ and neglecting the ordinary quark masses, the partial widths for the electroweak channels (V=W, Z) are

$$\Gamma(f^* \to fV) = \frac{1}{8}\frac{g_V^2}{4\pi} f_V^2 \left(\frac{m^{*3\,2}}{\Lambda_C}\right) \left[2 + \frac{M_V^2}{m*^2}\right] \left[1 - \frac{m_v^2}{m^{*2}}\right], \tag{1.55}$$

where

$$f_\gamma = fT_3 + f'\frac{Y}{2}, \tag{1.56}$$

$$f_Z = fT_3 + \cos^2\theta_W - f'\frac{Y}{2}\sin^2\theta_W, \tag{1.57}$$

and

$$f_W = \frac{f}{\sqrt{2}}. \tag{1.58}$$

Here, T_3, denotes the third component of the weak isospin of f^* and $g_W = \frac{e}{\sin\theta_W}$ and $g_Z = \frac{g_W}{\cos\theta_W}$ are the Standard Model Z and W coupling constants.

For the decay of excited quarks into ordinary quarks and gluons the partial width is given by

$$\Gamma(q^* \to qg) = \frac{1}{3}\alpha_s f_s^2 \left[\frac{m^*}{\Lambda_C}\right]^2 m^*. \tag{1.59}$$

There is a significant contribution to the width from contact interactions given by (multi-jet events)

$$\Gamma \to (f^* + f'\overline{f}') = \frac{m^*}{96\pi}\left[\frac{m^*}{\Lambda_C}\right]^4 N'_C S', \tag{1.60}$$

where $N'S_C$ is the number of colors of the light fermion and S' is an additional combinatorial factor given by

$$\begin{aligned} &S' = 1 \text{ for } f \neq f' \\ &S' = \frac{4}{3} \text{ for } f = f' \text{ where } f \text{ and } f' \text{ are quarks} \\ &S' = 2 \text{ for } f = f' \text{ where } f \text{ and } f' \text{ are leptons.} \end{aligned} \tag{1.61}$$

The partial widths and branching ratios of these decays are given in Tables 1.7 and 1.8 for the u^* and the d^* with $m^* = 300\ GeV/c^2$, $f_s = f = f' = 1$, $\Lambda_{QCD} = 175\ MeV$, $M_W = 80.35\ GeV$, $M_Z = 91.2\ GeV$, $\sin^2\theta_W = 0.23$, $\alpha^{-1} = 137.04$ and $\alpha_s = 0.097$. These tables were obtained from Reference [7].

1.2.3.1 Excited Quark Production

Excited quarks can be produced in $p\overline{p}$ collisions in many different ways. One way is $q^*\overline{q}^*$ pair creation from quark anti-quark annihilation or gluon-gluon fusion. Unfortunately, the cross section for this process is so small that it will be lost in the QCD and electroweak background processes. The cross section for gluonic excitation of quarks through contact terms such as, $q\overline{q} \to q\overline{q}^*$ or $q\overline{q} \to q^*q\overline{q}^*$ has the largest branching ratio but this channel will be swamped by QCD multijet events. The gluonic excitation of quarks, $g + q \to q^*$ has a large branching ratio and will produce a peak in the two jet spectrum.

Decay Channel	$\Gamma(GeV)$	B.R. $(\frac{\Gamma}{\sum\Gamma})$
$u^* \to ug$	9.69	30.0
$u^* \to u\gamma$	0.24	0.8
$u^* \to uZ$	1.07	3.3
$u^* \to dW$	1.06	3.3
Γ_{gauge}	12.1	37.4
$u^* \to u + f'\overline{f}'$	20.2	62.6
Total	32.3	100

Table 1.7. Partial widths and branching ratios for u^* [7].

Decay Channel	$\Gamma(GeV)$	B.R. $(\frac{\Gamma}{\sum\Gamma})$
$d^* \to dg$	9.69	29.7
$d^* \to d\gamma$	0.06	0.2
$d^* \to dZ$	1.60	4.9
$d^* \to uW$	1.06	3.3
Γ_{gauge}	12.4	38.1
$d^* \to d + f'\overline{f}'$	20.2	62.0
Total	32.3	100

Table 1.8. Partial widths and branching ratios for d^* [7].

The cross section for the gluonic $qg \to q^*$ process is given as follows

$$\sigma = \frac{\alpha_s \pi^2}{3\Lambda_C^2} f_s^2 \tau \frac{d\mathcal{L}^{gq}}{d\tau} \tag{1.62}$$

where

$$\tau = \frac{m^{*2}}{s}, \tag{1.63}$$

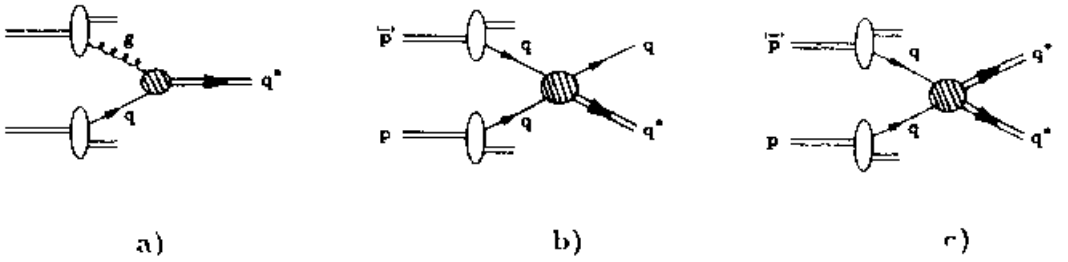

Figure 1.10. Diagrams contributing to q^* production in hadron collisions: (a) quark gluon fusion, (b) qq^* production via contact interactions and (c) q^* pair production via contact interactions.

s is the center-of-mass energy squared and $\frac{d\mathcal{L}_{qg}}{d\tau}$ is the quark-gluon parton luminosity. If gauge interactions are dominant over the contact interactions ($q^* \rightarrow q + f'\overline{f'}$), the signals for singly produced excited quarks are large transverse momentum $jj, j\gamma, jZ$ or jW pairs. In this analysis the reaction to be studied is

$$q + g \rightarrow q^* \rightarrow q + g \rightarrow two - jets \tag{1.64}$$

in which the branching ratio to two jets for gauge interactions is approximately 80%.

CHAPTER 2

THE EXPERIMENTAL APPARATUS

2.1 Introduction

The Tevatron is located at Fermi National Accelerator Laboratory in Batavia, Illinois. The Tevatron collides 900 GeV protons with 900 GeV anti-protons for a center of mass energy $\sqrt{s} = 1.8$ TeV. The Tevatron is the highest energy particle accelerator in the world. DØ is one of two collider detectors used to analyze these collisions. This chapter will describe the Tevatron complex and the DØ experiment. A large portion of the information for this chapter was taken from references [16–17].

2.2 The Tevatron Complex

The acceleration of antiproton and protons up to 900 GeV requires seven accelerators. The process starts with the proton source, hydrogen gas ions, being accelerated to 750 keV by the Cockcroft-Walton a major component of the preaccelerator. Then a linear accelerator or Linac accelerates the protons to an energy of 400 MeV before injecting them into the Booster which boosts them to 8 GeV. The protons are then ready to be injected into the Main Ring. The Main Ring serves to accelerate the protons up to 120 GeV for injection into the Tevatron but it is also the source of energetic protons used to produce antiproton for colliding beam operations. During antiproton production, these protons are

Accelerator Energies

Accelerator Energies			
Accelerator	Initial energy	Final energy	Destination
Preaccelerator	0	750 keV	Linac
Linac	750 keV	400 MeV	Booster and dumps
Booster	400 MeV	8 GeV	Main Ring, dumps and Antiproton source
Antiproton Source	8 GeV	8 GeV	Main Ring
Main Ring	8 GeV	120 GeV for Pbar production	Antiproton source
	8 GeV	150 GeV for Tevatron injection	Tevatron
Tevatron	150 GeV	800 GeV for fixed target	Switch yard
	150 GeV	900 GeV for collider	circulates through Tevatron
Switch yard	800 GeV	800 GeV	Proton, Meson, Neutrino and Muon beam lines

Table 2.1. Table of the accelerators that make up the Fermilab Tevatron Complex

collided into a nickel target and antiproton among other particles are produced. The subsequent antiproton are collected and cooled Then the Debuncher and Accumulator at the Antiproton Source. Once the protons or anti-protons have been accelerated to 120 GeV they are injected into the Tevatron. The protons are accelerated in a clockwise direction to 900 GeV, while the antiproton are accelerated in the counter clockwise direction to 900 GeV for collider operations. For fixed target operations the protons are accelerated to 800 GeV before being split off by the switching yard to the various fixed target beam lines. For an overview of the accelerator complex see figure 2.1 and table 2.1. For an overview on accelerator physics see References [18].

2.2.1 The Preaccelerator

The Preaccelerator consists of a negative ion hydrogen source or Magnetron plasma source, an electrostatic accelerating column or Cockcroft-Walton generator and a transport line for injection into the Linac.

2.2.1.1 Magnetron Plasma Source

The Magnetron plasma source, figure 2.2, produces a pulsed negative hydrogen ion beam of 50 mA and 18 KeV. This source has an oval shaped cathode surrounded by an anode and operates in a magnetic field parallel to the cathode surface. The magnetron is filled with a hydrogen gas to a pressure of a few hundredths of a millitorr and energized with a few hundred volts. The non-varying electric and magnetic fields force the electrons to spiral within the anode-cathode gap around 1 mm, creating a dense plasma. Negative ions are created by positive ions (the plasma) hitting the cathode. The positive ion either acquires two electrons upon entering the cathode surface and becomes a negative ion or sputters atoms from the surface which may leave as negative ions. The

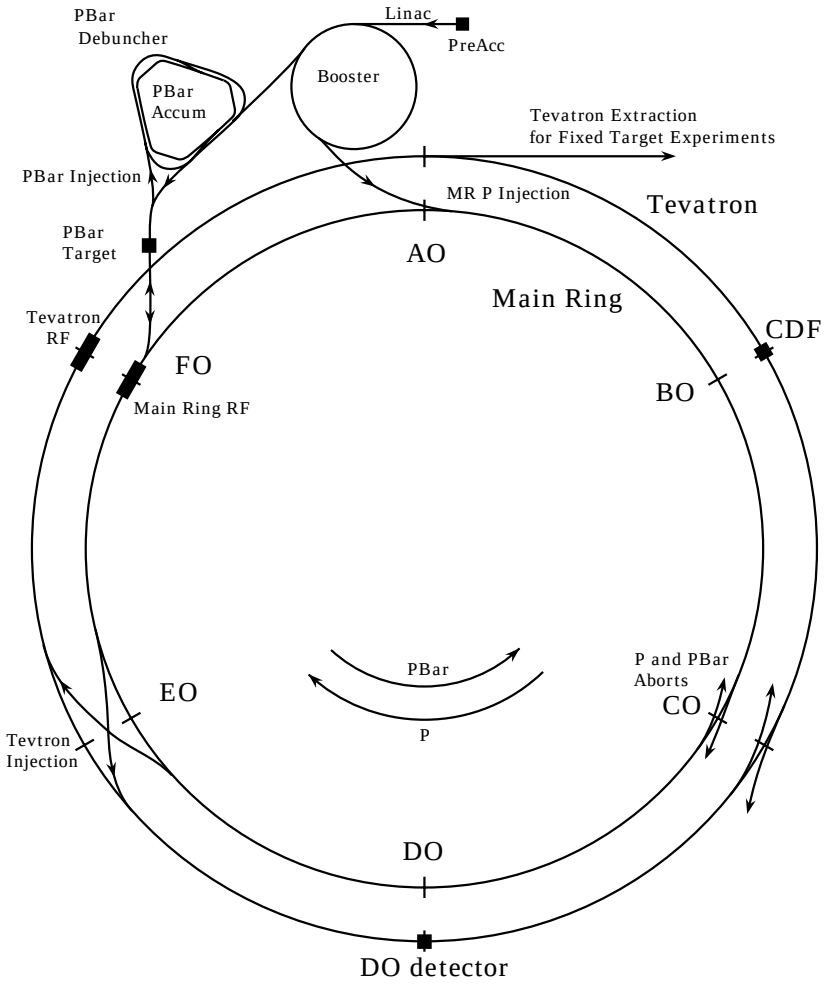

Figure 2.1. The Fermilab Tevatron proton/antiproton synchrotron.

sputtering by hydrogen atoms from the surface of the cathode is a larger effect. Hydrogen atoms leaving the surface of the cathode have a small chance, less than 0.2%, of removing the necessary electrons. Cesium is mixed with the hydrogen gas source and coats the cathode surface decreasing the surface work function of the cathode and improves the efficiency of this process to around 10% [16]. Once the ions are formed they are extracted through the anode and accelerated through the extractor plate. Electrons and other particles are eliminated by a right angle bend magnet. The source operates in a pulsed mode of 15 Hz which matches the Linac cycle. Source operation control systems are operated by

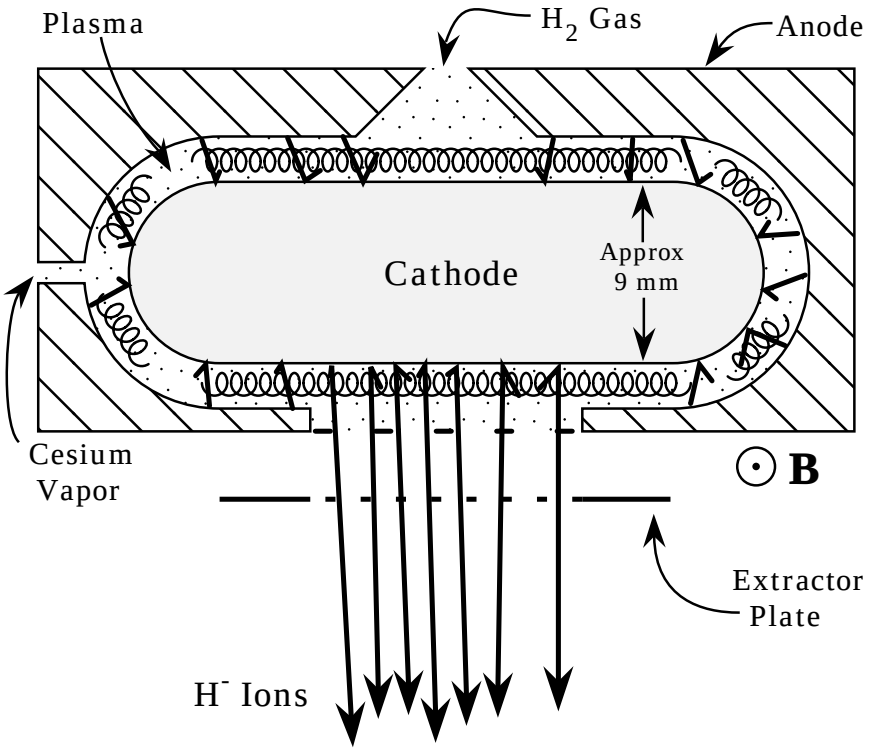

Figure 2.2. The Magnetron source

optical links between the electrically isolated source and the control room. The Magnetron is powered by a 15 kW alternator located inside the Cockcroft-Walton dome.

2.2.1.2 The Cockcroft-Walton Generator

Once the ion is produced it is accelerated through an electrostatic accelerating column. The voltage used for this acceleration is produced by the Cockcroft-Walton generator. This solid state device generates high voltage by charging capacitors in parallel from an AC voltage source and discharging them in series. This is made possible with many diodes. See figure 2.3 for a diagram of the diode voltage multiplier inside the Cockcroft-Walton. The Cockcroft-Walton has five stages each stage adds $2V_0$ to the input voltage for at total output voltage

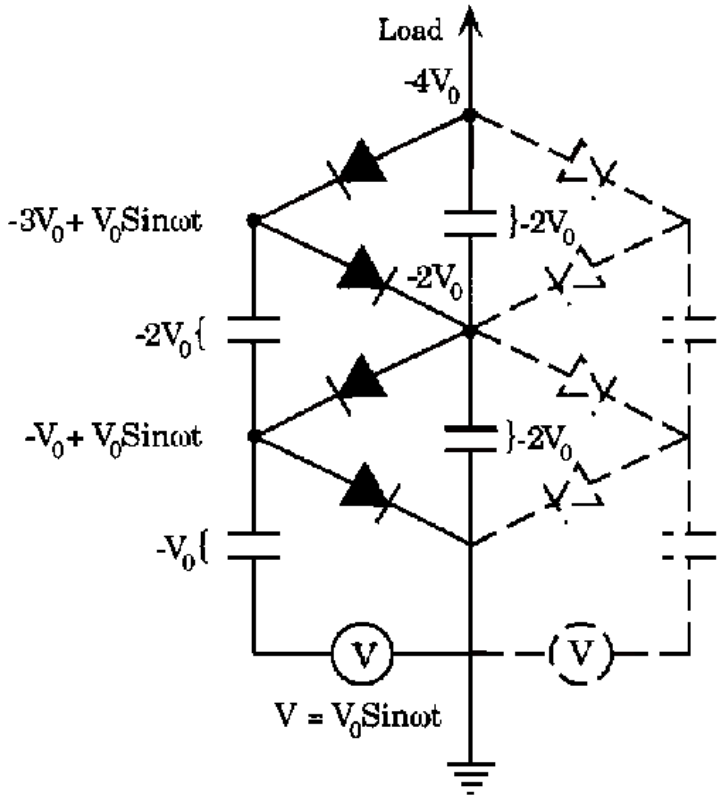

Figure 2.3. Diode voltage multiplier for the Cockcroft-Walton of 750 kV. A second leg is added to the diode multiplier ladder to reduce a ripple effect (dashed lines).

2.2.2 The Linac

The Linac takes the 750 keV H^- ions and accelerates them up to 400 MeV for injection into the Booster. The Linac consists of 14 cylindrical cavities or tanks arranged end to end. The first stage of the Linac is an Alvarez drift

tube accelerator which accelerates the ions to 116 MeV. The second stage is a side-coupled Linac that replaced 67 m of the previous Alvarez drift tube accelerator which accelerates the ions to 400 MeV.

2.2.2.1 The Alvarez Drift-Tube Linac

The Alvarez drift-tube Linac uses five electrically resonant cylindrical OFHC (Oxygen Free High Conductivity) copper clad steel tanks, see figure 2.4. This Linac is approximately 79 m long. Each tank is driven by its own RF system that produces 5 MW of power in 400 μ sec pulses in phase with the Booster cycle of 15 Hz. Each tank consists of between 23 and 59 drift tubes suspended at the center of the tank. The particle should experience an acceleration when it is in the gap between drift tubes and the decelerating fields should occur when the particle is shielded within a drift tubes, see figure 2.5. Ideally, this means the RF should be at its maximum at the gaps this corresponds to a synchronous phase angle ϕ_s of zero. Meaning that particle experiences the electric field at its minimum inside the cavity and its maximum in the gaps between cavities. A bucket is a RF structure. If a bucket is filled with beam it is known as a bunch.contains beam particles.

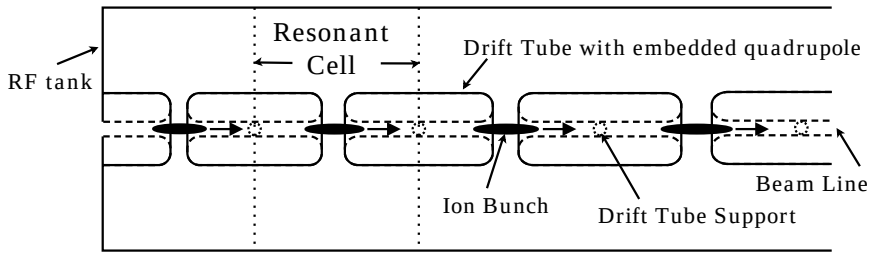

Figure 2.4. Top view of an Alvarez drift tube Linac

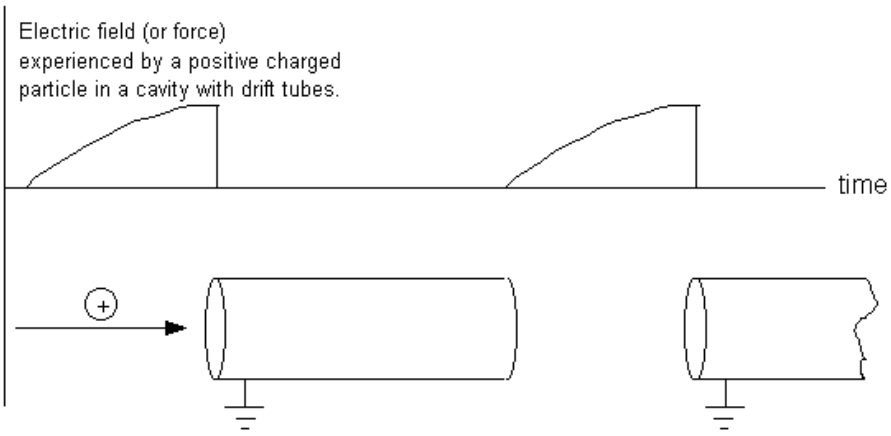

Figure 2.5. The electric field experienced by a charged particle in the Linac

2.2.2.2 The Side-Coupled Linac

The Side-Coupled Linac is an upgrade to the Alvarez Linac. It operates in similar fashion but its cavities are more efficient and resonate with the fourth multiple of the drift-tube linac, therefore in this section every fourth RF cycle or bucket contains beam particles. The power for this section is provided by seven 10 MW, 805 MHz klystrons. This upgrade increases the charge current into the Booster which will improves luminosity.

2.2.3 The Booster

The Booster takes the 400 MeV negative hydrogen ions obtained from the Linac and strips off the extra electrons and accelerates the remaining proton core to 8 GeV. The Booster is a synchrotron accelerator with a radius of 75 meters. In a synchrotron accelerator the RF is synchronized with the bending magnet strengths. Thus as the particles gain energy through the RF the bending magnet strengths are increased to maintain a fixed size orbit. The Booster uses combined function magnets which are magnets that are used for focusing the beam and bending the beam at the same time, see figure 2.6. Whereas, in the Main Ring and the Tevatron the magnets are separated function magnets. Separated

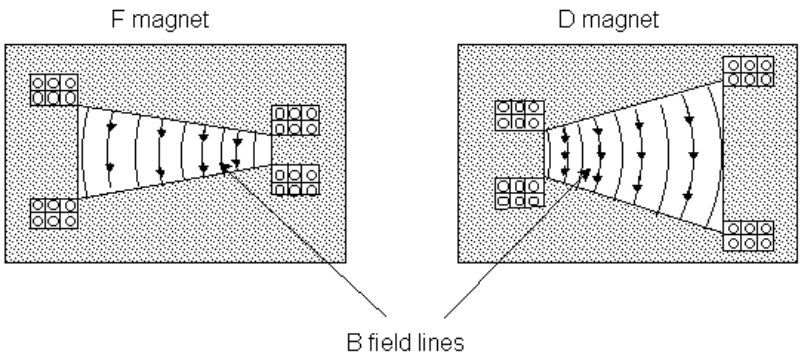

Figure 2.6. Combined Function Booster Magnets

function design means one magnet bends the beam using a dipole, a different magnet focuses the beam using a quadrupole magnet and minor corrections to the beam are made by sextupole or higher order magnets. Combined function magnets are necessary for the Booster because of the frequency with which the Booster completes the acceleration cycle.

The Booster consists of 96 combined function dipole/quadrupole magnets with 17 cavity resonators (RF) arranged in a 151 m lattice. Since the momentum spread from the Linac corresponds to 8mm radius difference in the Booster which fills the small aperture of the Booster beam pipe a Debuncher is placed at the end of the Linac to reduce the momentum spread to an acceptable level.

Injection into the Booster from the linac occurs by multi-turn charge-exchange injection at 15 Hz. In multi-turn charge-exchange, beam from the Booster(protons) and beam from the Linac (ions) are merged after passing through a dog leg or two adjacent dipole magnets with opposite polarity, this is also known as an orbital bump magnet. Once the beams are merged electrons are separated from the hydrogen ions by passing through a carbon foil. This charge exchange is non conservative so the beams can be merged with out violating Liouville's theorem. Orbital Bump Magnet 2 bends the beam back onto the

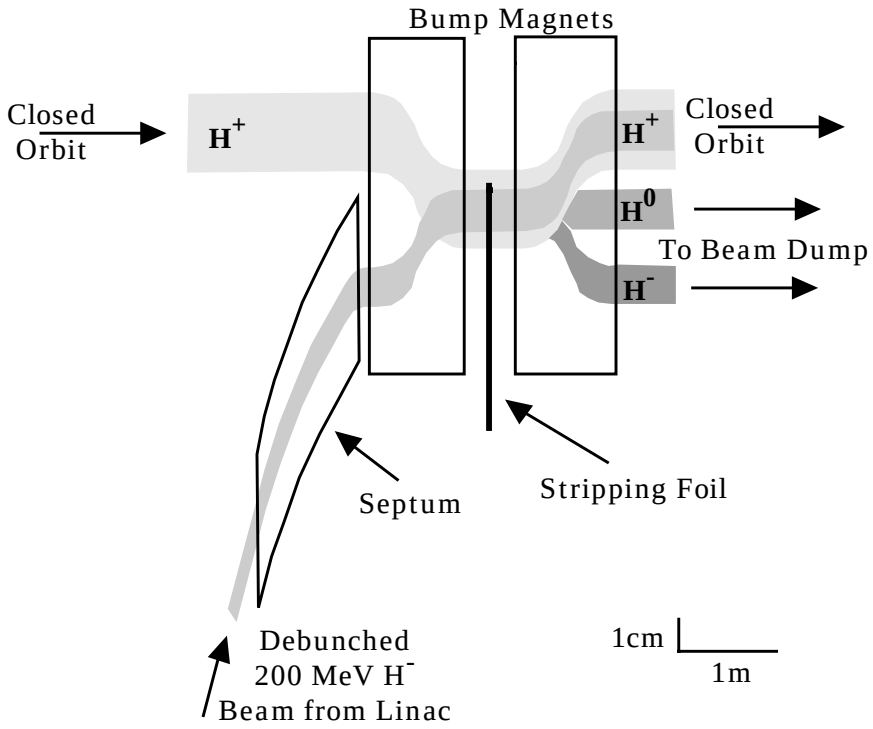

Figure 2.7. Multi turn bump injection.

Booster path while causing the leftover negatively charged ions to be bumped into the beam dump, see figure 2.7. The Booster is usually filled in 6 turns and once filled the orbital bump magnets are turned off to prevent losses.

Once the Booster is filled the RF is phased in order to create a RF bucket structure. The Booster consists of 84 buckets which corresponds to the harmonic number of the Booster. A bucket is a RF structure when particles are inside a bucket it is known as a bunch. Once the appropriate bucket structure is obtained the beam is accelerated to 8 GeV by varying the RF from 37.9 MHz to 52.813 MHz. The beam can be directed to four different places:

- The Main Ring through the 8 GeV line
- The 8 GeV Dump
- The AP4 line, used to make anti-protons at the antiproton source

- The long 3 dump

The Booster injects protons and antiproton into the Tevatron and also injects protons into the antiproton source area. In the first mode 11, 13,or 15 bunches of protons are injected into the Main Ring where they are coalesced into one bunch. The rest of the bunches are sent to a beam dump. In the second mode used for antiproton production the Booster delivers one full batch of protons 83 bunches to the Main Ring approximately every 2.4 μsec. The protons experience transition within the energies of the Booster. Transition is the point at which relativistic effects become important and is a important region of instability. For more information about this see appendix A.

2.2.4 The Main Ring

The Main Ring is a separated function synchrotron with a radius of 1000 m which can accelerate the beam up to 400 GeV. For Run I of the Tevatron the Main Ring was used to inject beam into the Tevatron at 150 GeV. The Main ring consists of 774 dipole or bending magnets, 240 quadrupole magnets for focusing and 18 dual gap RF cavities to accelerate the protons or antiproton. It contains 1113 RF buckets and operates at 53 MHz. The Main ring consists of 6 sectors. Each sector starts with a long straight section or zero section. The straight sections consist of interaction regions like DØ or B0 (CDF) where the collider experiments exist, injection or extraction lines, and RF cavities. The rest of the sector is made of four more sub-sectors. Each sub-sector is a series of magnets called cells. These cells consist of bending or dipole magnets, quadrupole magnets and higher order magnets for trim or minor corrections arranged in the appropriate lattice [19]. Since the Tevatron was built directly under the Main Ring over-passes were built at DØ and B0 to separate the Main Ring from the Tevatron at the interaction regions. The Main Ring completely

detours around CDF but passes through a portion of the DØ detector and shows up in data as the Main Ring hole.

2.2.5 The Antiproton Source

The Antiproton Source is comprised of a target station, two rings called the Debuncher and the Accumulator and the transport lines between those rings and the Main Ring. The following is an outline of what takes place in order to produce an antiproton beam suitable for collider operations.

- About 83 bunches of 120 GeV protons with small time spread are extracted from the Main Ring and directed onto a nickel target.
- Particles of approximately 8 GeV are collected from the secondaries, using a lithium lens.
- The anti-protons go through successive cooling methods for later injection into the Main Ring. These involve stochastic cooling system involving the Debuncher and the Accumulator.

2.2.5.1 Antiproton Target and Lithium Lens

The antiproton target is used in creating anti-protons. The target consists of a stack of nickel disks separated by copper cooling disks with channels for air flow to provide heat transfer. Copper targets were once used but now have been replaced by nickel because it can withstand higher heat deposition before melting. Standard targets are 10 cm in diameter and 2 cm thick. The disks have a hole in the center to facilitate air flow out of the assembly. For further information see [20]. The angular distribution of particles coming off of the target depends on kinematic processes involved and the spatial distribution depends on the proton spot size on the target. Minimizing this spot size

minimizes the phase space occupied by the antiproton emerging from the target. A lithium lens is located downstream of the target module. The lens is designed to collect the secondary particles produced in the target collisions and make them parallel. Electric current passing through the cylindrical lithium conductor produces a solenoidal magnetic field that focuses the negative secondaries. Lithium was chosen because it is the least dense solid conductor. Which minimizes scattering and absorption of the antiproton produced. The lens operates on a peak current of 670,000 a for a gradient of 1,000 Tesla/meter. The lithium conductor is 15 cm long and 2 cm in diameter. The lens is cooled with a closed loop cooling system. See figure 2.10. A Pulsed magnet, a 3-degree pulsed dipole, follows the lens. Its purpose is to select 8 GeV negatively charged particles. Most particles not selected by the pulsed magnet are sent to the beam dump and absorbed by a graphite core dump. About 10^7 antiproton are produced for every 10^{12} protons that hit the target.

2.2.5.2 Debuncher

The Debuncher was designed to reduce the momentum spread of the antiproton coming from the target. This is done by RF bunch rotation and adiabatic debunching to reduce the transverse profile of the beam prior to injection into the Accumulator through stochastic cooling. The Debuncher is 6.6% longer than the Accumulator but both occupy the same tunnel. The Debuncher is approximately triangular in shape with three straight sections with low dispersion and vertices that are smooth arcs. The antiproton cycle takes 2.4 sec which leaves time for stochastic cooling. Cooling reduces the phase space of the beam and the momentum spread by reducing the transverse oscillations of the beam. In regions of low dispersion, areas where the transverse particle position is least affected by the particles longitudinal momentum, beam pickups measure the transverse

position of a particle around the central orbit. Transverse oscillations around the central orbit are known as betatron oscillations. A signal is sent across the central section of the antiproton source ring to correct the oscillation. See figure 2.9. This signal is amplified and kicks the particles whose position was just measured to reduce the amplitude of betatron oscillations. The resultant correction is very small, approximately 1 part in 10^6 but the correction adds up since the beam makes approximately 10^6 turns a second. This is a very simple description of what happens please read [16, 20–21] for more details.

2.2.5.3 Accumulator

The Accumulator is similar in shape and size to the Debuncher but its vertices contain short straight sections. The antiproton are injected in closed injection orbit which is 80 cm outside the central orbit. As the beam is stacked or filled bunches are pushed closer and closer to the central orbit. The Debuncher and Accumulator operate above transition which means differences in particle momentum translates into different path lengths or the length of the closed orbit. Lower momentum particles follow a smaller orbit and higher momentum particles follow a longer orbit, which is opposite to what happens below transition. The injected beam is adiabatically captured by a 53 MHz RF system and decelerated by 60 MeV to the tail of the stack, over 300 ms. For a profile of this stacking process see figure 2.8.

Once the beam is pushed into the core three more stochastic cooling systems work on the beam. First, there is the momentum cooling system which controls the momentum spread. Second, there is the betatron cooling systems which acts to control the vertical and horizontal distributions of the beam about the central core orbit. Finally, additional stochastic cooling occurs.

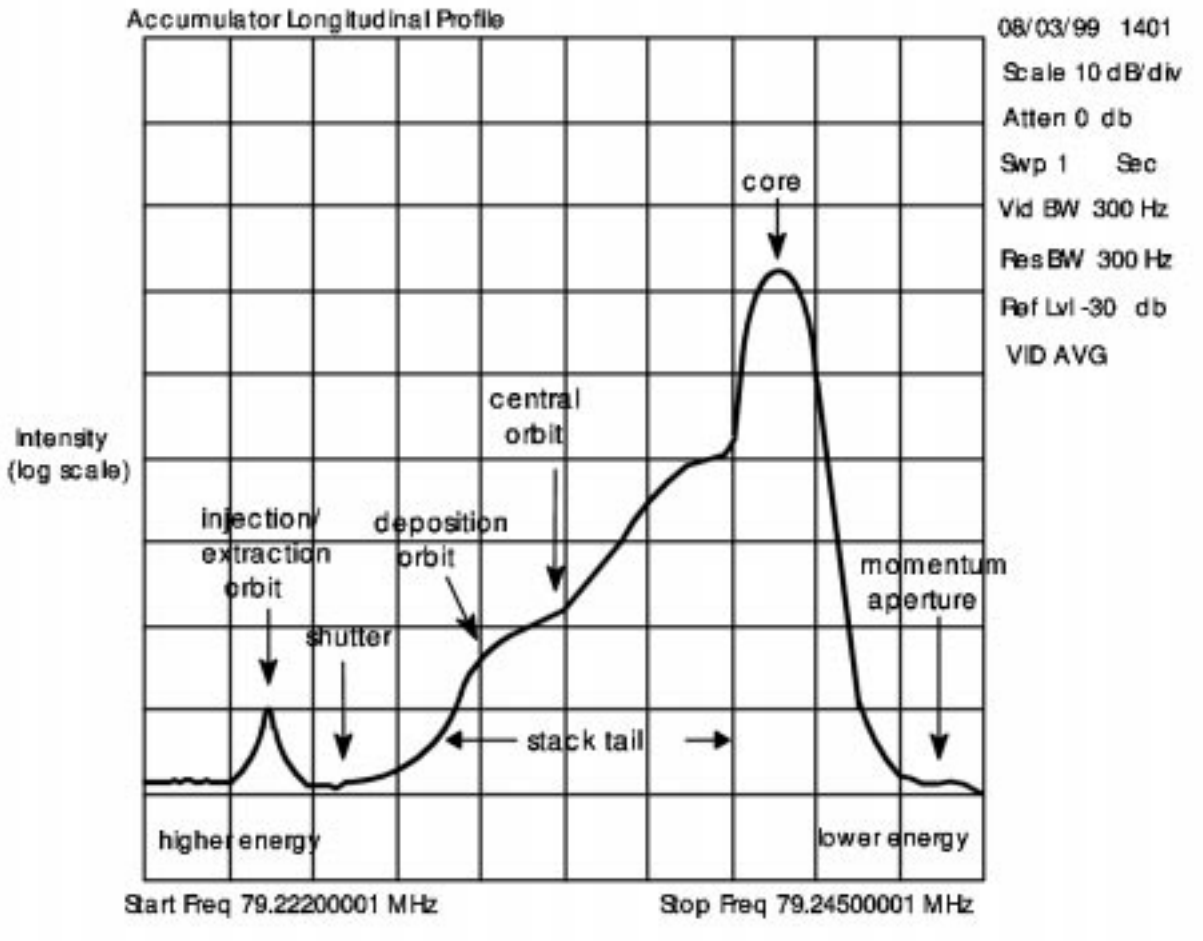

Figure 2.8. Accumulator Longitudinal Stacking Profile

2.2.6 The Tevatron

The Tevatron is a synchrotron accelerating protons and antiproton to a center of mass energy of 1.8 TeV. The Tevatron has 774 dipoles and 216 quadrupoles. Unlike the Main Ring all of the quadrupoles, dipoles and correction magnets are superconducting. These magnets are held at a temperature of 4.6 K and need to be cooled with liquid helium. The RF system operates at 53 MHz yielding 1113 RF buckets the same number as the Main Ring. At the beginning of a store 6 proton bunches and 6 antiproton bunches are injected into the Tevatron from the Main Ring. They are accelerated up to 900 GeV each for collider operations.

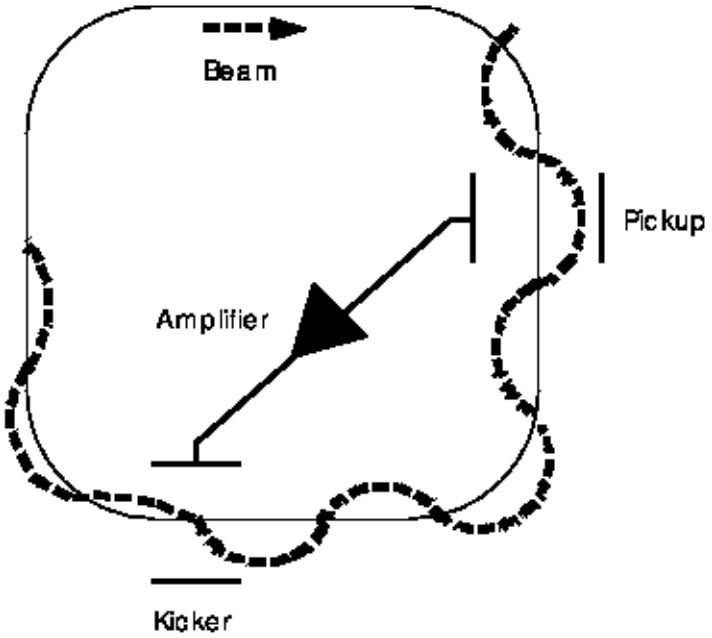

Figure 2.9. Stochastic Cooling.

2.3 The DØ Detector

The DØ Collider Detector was designed to study high center of mass collisions of protons and antiproton at $\sqrt{s}$ of 1.2 TeV.

The general features of the detector are

- Level 0 Detector (twin hodoscopes) used as a hard scattering trigger.
- Small non-magnetic tracking region with a radius of 78 cm.
- A stable, hermetically sealed, finely segmented sampling calorimeter with liquid argon as the active material.
- A muon detector with a thick iron toroid magnet/absorber for good momentum measurement and minimized background due to hadronic punch through.

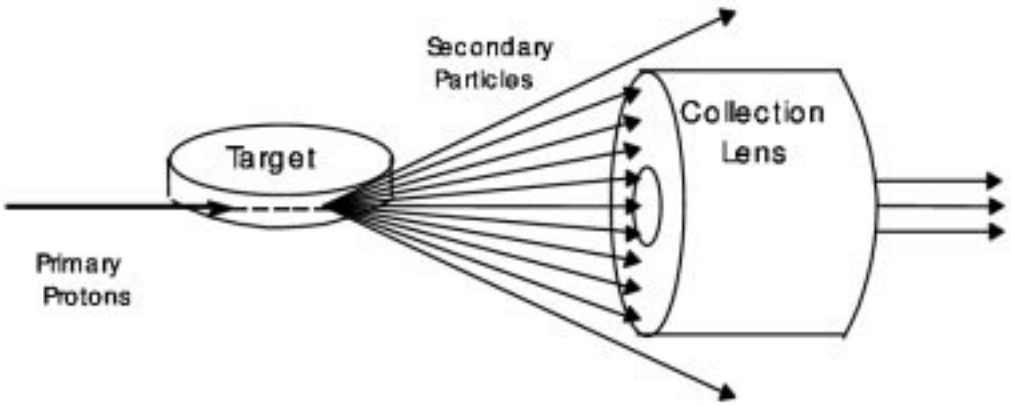

Figure 2.10. The Lithium Lens

The tracking volume is small to accommodate the calorimeter's depth without disrupting the effective less of the muon detector. The detector weighs 5500 tons with a height of 13 meters and a width of 20 meters [17].

2.3.1 Coordinate System

The coordinate systems used for describing the detector and the beam are right handed cylindrical (r, ϕ, z) or sometimes spherical (r, ϕ, θ). The positive z axis is aligned in the direction of protons and the negative z axis is aligned in the direction of the anti-protons. The y axis points up from the center of the beam pipe this is parallel to line from (0,0,0) through $\phi = \pi$. Pseudorapidity , η, is often used instead of θ since it is approximately Lorenz invariant.

The pseudorapidity is an approximation of the rapidity, where

$$y = \frac{1}{2} \ln \frac{E + p_z}{E - p_z}. \tag{2.1}$$

The first derivative of rapidity is Lorenz invariant. This is important because the fraction of beam momentum possessed by the initial state partons varies from event to event. If we assume $p >> m$ the rapidity may be reduced to the pseudorapidity,

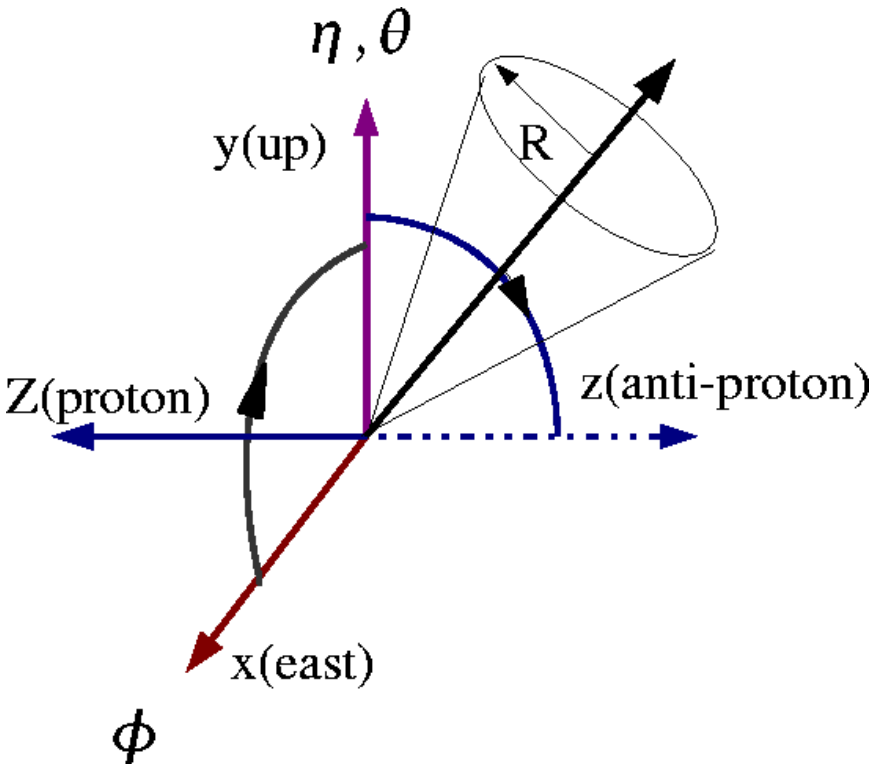

Figure 2.11. The DØ Coordinates.

$$\eta = -\ln tan\frac{\theta}{2}. \tag{2.2}$$

We use E_T to measure energy deposited transverse to the beam. E is used instead of p since the calorimeter measures energy deposited and we do not measure the mass of the particles producing the jets. E_T is useful because the transverse energy of an event should be conserved.

$$E_T = E \sin\theta \tag{2.3}$$

2.3.2 Level Zero Detector

The Level 0 scintillator or twin hodoscope array is used to determine if an inelastic collision has occurred during a bunch crossing and provides a rough estimate of the z position of the collision. The vertex position is described by a Gaussian with width of 25 cm offset from z=0.0 by 8 cm.

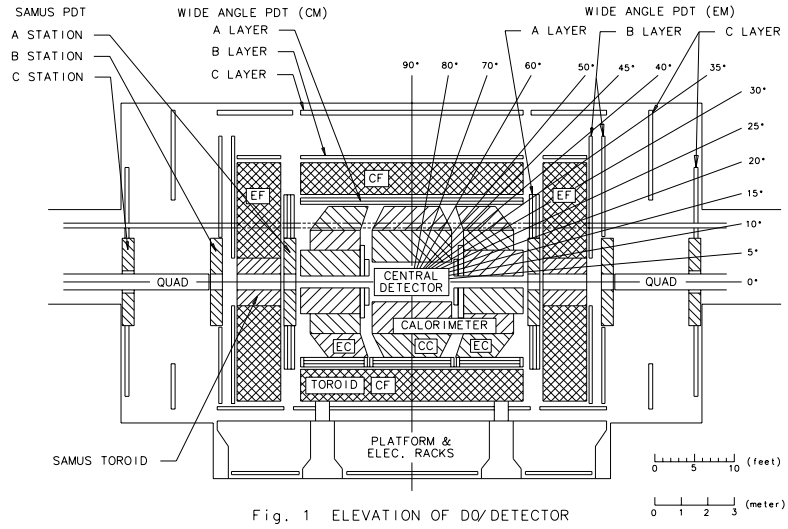

Figure 2.12. The DØ detector.

A scintillating hodoscope array is placed between each end calorimeter and the central calorimeter. These arrays are 140 cm from the center of the detector and perpendicular to the beam axis. These arrays will collect most collision products. These hodoscope arrays cover the full $|\eta|$ range from 2.2 to 3.9 and partially covers down to 1.9 and as high as 4.3. When both arrays detect charged particles within a small time interval an inelastic collision has occurred. The hodoscopes are the level 0 trigger and the start of a three level trigger system used in data acquisition which will be discussed in the next chapter (Triggers and Data Acquisition). Additionally, the Level 0 trigger allows one to monitor the interaction rate which provides a measurement of the instantaneous particle luminosity ($\mathcal{L}$).

2.3.3 Tracking

The Central Detector (CD) is composed of the Vertex Drift Chamber (VTX), the Transition Radiation Detector (TRD), the Central Drift Chamber and two

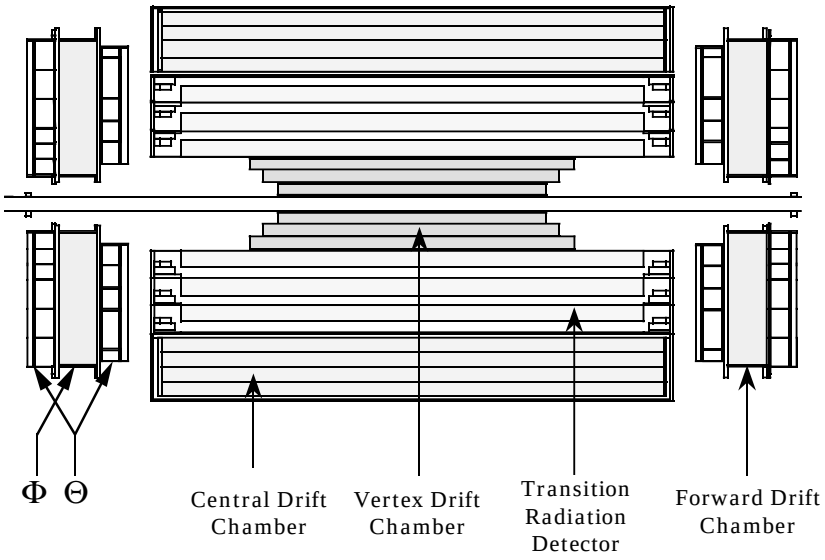

Figure 2.13. The central detectors at DØ.

Forward Drift Chambers (FDC). The main purpose of the CD was two-track resolution, efficiency, good ionization energy measurement and rejection of pions. The Central Detector is cylindrical with 3.5cm<r<78cm and is completely enclosed by the calorimeter.

2.3.3.1 The Vertex Detector (VTX)

The primary function of the Vertex Detector is a precision measurement of the interaction vertex and secondary vertices from particle decays near the beam pipe and the rejection of photons which convert to e^+, e^- after the VTX.

The VTX is the inner most tracking detector and has an inner radius of 3.7cm just outside the beryllium beam pipe and an outer radius of 16.2 cm. The VTX consists of three mechanically concentric layers of cells(see figure 2.14). Each cell has eight sense wires that provide measurement of the r -ϕ coordinate. The inner most layer has 16 cells and the outer two layers have 32 cells each. Each cell consists of sense wires parallel to the beam pipe. Adjacent sense wires are staggered by $\pm$ 100 micro m to resolve left-right ambiguities. Additionally, the

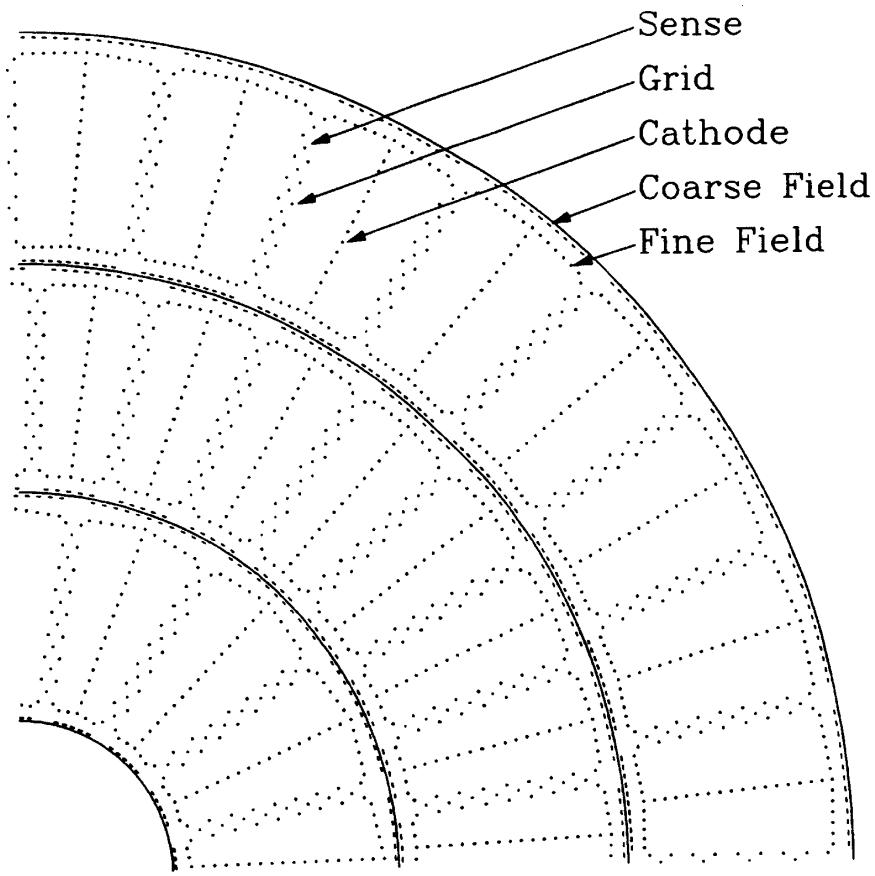

Figure 2.14. The Vertex Detector at DØ.

three layers are offset in ϕ to further aide in pattern recognition and calibration. The gas used within the drift chamber is CO_2 with 5% ethane and 0.5% H_2O at one atmosphere. A low diffusion, low drift velocity gas is required for a high spatial resolution and high resolving power for closely spaced tracks. The spatial resolution of the VTX is 60 μm

2.3.3.2 The Transition Radiation Detector TRD

The Transition Radiation Detector surrounds the VTX. Since DØ does not have a magnetic field inside the tracking area the TRD was designed to distinguish between electrons and hadrons. When a charged particle enters a dielectric material the field configuration surrounding the particle will be altered

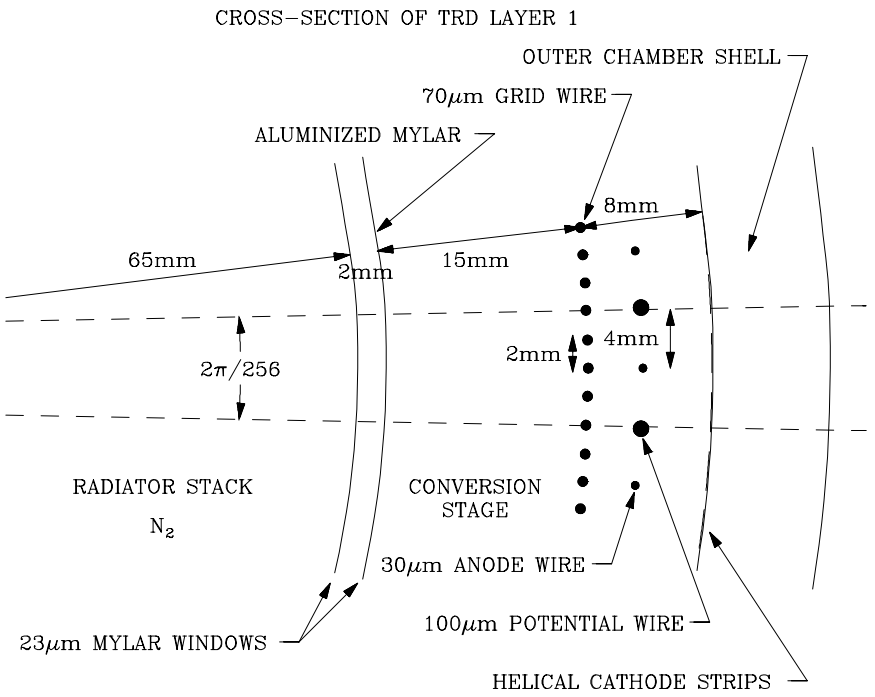

Figure 2.15. The Transition Radiation Detectors at DØ.

due to the presence of an additional polarization field that is a response to the particle's electric field. When there is a transition from one dielectric material to another photon emissions occur(x-rays). This effect becomes appreciable only for highly relativistic charged particles ($\gamma > 10^3$). This provides a way to discriminate between charged particles such as electrons and positrons which are highly relativistic and charged hadrons which are not highly relativistic at the Tevatron. The TRD consists of three concentric stacks of 18 μm polypropylene foils used as the dielectric medium. Each stack consists of 400 foils separated by 150μm gaps. Many foils must be used since the probability of photon emission in a single foil is very low. The x-rays are detected through conversion in a xenon-methane drift chamber following each dielectric stack. Measurement of the arrival time of electron clusters and the total collected charge the TRD can differentiate between electrons and positron and slow moving hadrons.

Vertex Chamber Parameters

Length of active volume: Layer 1	96.6 cm
Layer 2	106.6 cm
Layer 3	116.8 cm
Radial Interval (active)	3.7-16.2 cm
Number of Layers	3
Radial wire interval	4.57 mm
Number of sense wires/cell	8
Number of sense wires	640
Type of Gas	$CO_2(95\%) - ethane(5\%) - H_2O(0.5\%)$
Pressure of Gas	1 atm
Drift Field	1.0-1.6 kV/cm
Average Drift Velocity	7.6-12.8 μm/ns
Gas Gain at Sense Wires	4x10^{-4}
Sense Wire Potential	+2.5 kV
Diameter of Sense Wire	25 μm NiCoTin
Diameter of Guard wire	152 μm Au-plated Al

Table 2.2. Vertex Chamber Parameters

2.3.3.3 The Central and Forward Drift Chambers (CDC) and (FDC)

The Central Drift Chamber CDC is situated between the TRD and the Calorimeter. The CDC consists of a set of wires with a high potential. When an energetic charged particle crosses the chamber atoms from gas inside the CDC are ionized. These charges are attracted to and collected by the wires. The time of flight of these charges is translated into coordinates in space. The track is reconstructed from the hit positions obtained from each wire. The chamber was

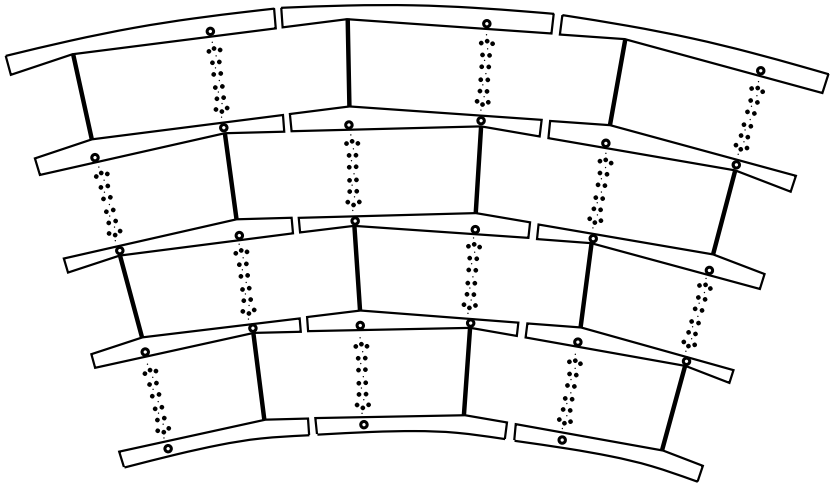

Figure 2.16. The Central Drift Chamber at DØ.

designed for good spatial resolution of individual particles, two track resolving power, high efficiency and good ionization energy measurement. The chamber has a radial dimension of 49.5 to 74.5 cm and is 184 cm long. The pseudorapidity range for the the CDC is -1.2 to 1.2 η. The chamber is composed of four layers each with 32 cells. The second and fourth layers are offset by $\pi/32$ with respect to the first and third layers. The maximum drift distance is 7 cm. Each cell contains 23 wires. See figure 2.16 and table 2.3.

The Forward Drift Chambers (FCD) are located forward and rear-ward of the VTX,TRD, and CDC. Each FDC consists of three separate chambers: the Φ module with radial wires which measures the ϕ coordinates, two Θ modules offset by 45 with azimuthal wires which measures the θ coordinate. The FDC uses the same gas as the CDC and has similar resolution.

2.3.4 Calorimetry

The calorimeter measures the energy released in particle interactions by completely containing all produced particles except muons, neutrinos and additional particles that escape down the beam pipe. Muons with energies less

Central Drift Chamber Parameters

Length of active volume	179.4 cm
Radial Interval (active)	51.8-71.9 cm
Number of layers	4
Radial wire interval	6.0 mm
Number of sense wires/cell	7
Number of delay lines	256
Type of Gas	$Ar(93\%) - CH_4(4\%) - CO_2(3\%) - H_2O$
Pressure of Gas	1 atm
Drift Field	620 V/cm
Average Drift Velocity	34 μm/ns
Gas Gain at Sense Wires	2,6x1-^{4}
Sense Wire Potential	+1.5 kV
Diameter of Sense Wire	30 μm Au-plated W
Diameter of Guard wire	125 μm Au-plated CuBe

Table 2.3. Central Drift Chamber Parameters

than 100 GeV lose their energy primarily through ionization at only 1-2 MeV $g^{-1}cm^2$ which means muons cannot be contained inside the volume of the calorimeter [22]. Neutrinos are weak interacting particles and do not deposit energy within the calorimeter. The DØ Calorimeter is a sampling calorimeter meaning the calorimeter is broken down into materials that absorb incoming particle energy known as passive materials and materials that generate signals or active materials. DØ uses depleted uranium or copper as the passive medium and liquid argon as the active medium.

The energy measurement inside the DØ calorimeter can be described by its response to electrons and hadrons. For the high energy electrons produced

	Θ modules	Φ modules
z interval	104.8-111.2 cm	113.0-127.0
	128.8-135.2 cm	
Radial Interval (active)	11-62 cm	11-61.3 cm
Number of cells in radius	6	
Maximum Drift Distance	5.3 cm	5.3 cm
Sense wire staggering	0.2 mm	0.2 mm
Sense wire separation	8 mm	8 mm
Angular interval/cell		1
Number of sense wire/cell	8	16
Number of delay lines/cell	1	0
Number of sense wires/end	384	576
Number of Delay lines readout/end	96	
Type of Gas	$Ar(93\%) - CH_4(4\%)$ $-CO_2(3\%) - H_2O$	
Pressure of Gas	1 atm	1 atm
Drift Field	1.0 kV/cm	1.0 kV/cm
Average Drift Velocity	37 μm/ns	40 μm/ns
Gas Gain at Sense Wires	2.3,5.3x10^{-4}	3.6 x10^{-4}
Sense Wire Potential	+1.5 kV	+1.5 kV
Diameter of Sense Wire	30 μm Au-plated W	
Diameter of Guard wire	163 μm Au-plated Al(5056)	

Table 2.4. Forward Drift Chamber Parameters

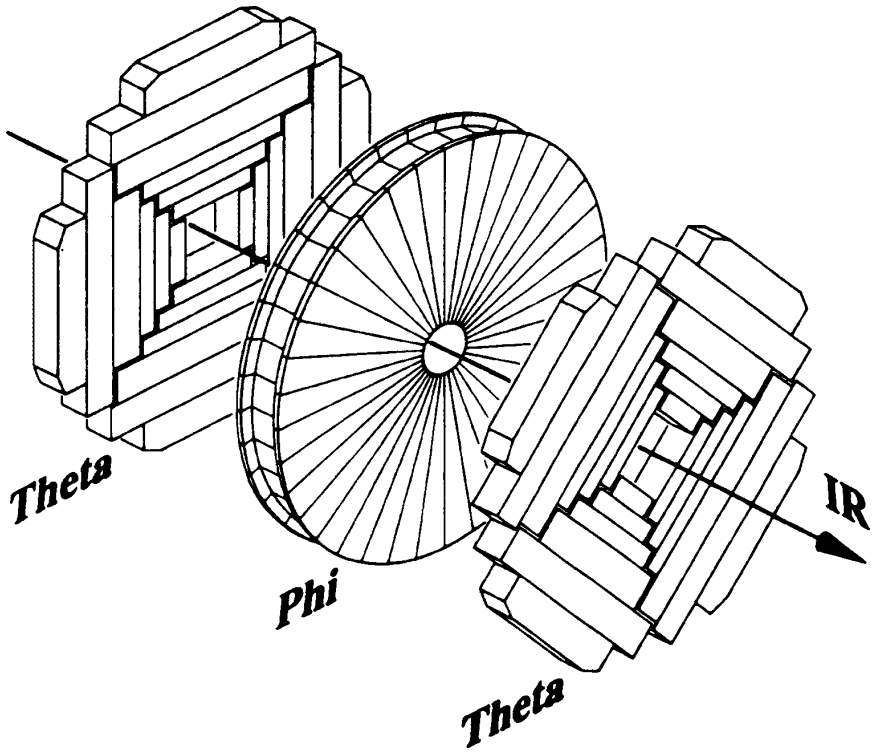

Figure 2.17. The Forward Drift Chamber modules at DØ.

at DØ, with energies greater than 1 GeV the main energy loss mechanism is bremsstrahlung radiation. The electromagnetic shower can be described by QED and depends on the density of the absorbing medium. The radiation length, χ_0, or distance over which an electron or positron loses, on average, 63.2% of its energy can be parameterized as follows,

$$\chi_0 \approx 180\frac{A}{Z^2} \tag{2.4}$$

Where A is atomic mass and Z is the atomic number of the absorbing medium. This supports the use of depleted uranium as the passive medium for the electromagnetic region of the calorimeter.

During a high energy electromagnetic shower many photons are produced most of which are of low energy and are absorbed through Compton scattering and the photoelectric effect. The higher energy photons having more than

5-10 MeV pair produce electrons and positrons. These electrons and positrons my in turn produce more photons, etc. The average energy of these particles decreases as the shower continues and eventually no further multiplication occurs and energy deposition decreases. The point at which this occurs is known as shower maximum. Subsequently, many low energy photons are produced and are absorbed in the passive medium by Compton scattering and are too far from the active medium to be measured. The radiation length for photons is $\frac{7}{9}\frac{A}{N_A\chi_0}$. This loss produces the differences in the response of electrons and minimum ionizing particles or MIPs in the detector (e/mips) [22]. MIPs are theoretical particles that lose energy strictly through ionization. Muon response is usually used in this comparison (e/μ) since muons are the closest thing to a MIPs around. At DØ electromagnetic showers are contained inside the EM portion of the calorimeter.

Hadronic showers involve both electromagnetic interactions and strong interactions and are much more complicated. The complication occurs because strong nuclear reactions with the absorbing media are not entirely detectable by the calorimeter. In hadronic showers mostly pions (π) are produced since these are the lightest hadronic particles. On average 1/3 of the particles produced are π^0's and decay to photons which subsequently decay through electromagnetic showering. That leaves 2/3 of the remaining particles ($\pi^{\pm}$) to decay hadronically into 1/3 π^0's, *etc.* These decays occur until the charged hadrons have lost enough energy to be absorbed by the passive medium. Additionally, a large portion of the hadronic decay energy is dissipated by nuclear binding energy of the passive medium which is not measured. This is because de-excitation of the nuclei is too slow to measure in one beam crossing. Since the amount of energy measured for hadronic showers depends on the production of π^0's which fluctuates from event to event coupled with binding energy losses this measurement has an intrinsically lower energy resolution than electromagnetic

showers. In an attempt to compensate the hadronic response (h/e) it was hoped that by using U^{238} energy could be recovered through fission, unfortunately this process is slow and cannot be fully recorded before the next bunch crossing. Instead, manipulation of passive and active region thicknesses were used to to compensate. The (h/e) response of the DØ detector is 1.1 .

Nuclear interaction length scales as $A^{\frac{1}{3}}$, see figure 2.19 for a profile of interaction lengths in the DØ detector.

The calorimeter at DØ consists of a Central Calorimeter (CC) and two end cap calorimeters (EC). The calorimeter provides a measurement of hadron position and energy as far forward as $|\eta|$ =4.1. The calorimeter is composed of uranium and copper used as absorbers and Liquid argon as the ionization medium. The liquid argon must be cooled to 86 K which requires a cryostat. The EC and CC are composed of three layers the electromagnetic (EM) layer with thin uranium absorber plates, fine hadronic layer (FH) with thicker uranium plates and the coarse hadronic (CH) layer with thick copper or stainless steel plates. The CH layer provides information about the end of hadronic showers while keeping density high and overall radius of the calorimeter small. Each section is composed of many cells that are identified by azimuth, pseudorapidity, and layer. There are 64 divisions on ϕ and 80 divisions in pseudorapidity spanning $-4.0 < \eta < 4.0$. Generally, each cell covers an area in η– ϕ of 0.1 X 0.1, exceptions will be discussed later. These layers are depicted in figure 2.18. Each cell consist of a dense absorber plate (uranium or copper) with a liquid argon gap between plates. A copper readout pad in the center of each gap and 2.3 mm from the absorber plates on each side are held at a potential of 2 kV, see figure 2.20.

Calorimeter Parameters

Active Medium	Liquid argon
Passive Medium	uranium or copper
Coverage	$\|\eta\| < 4.1$
Transverse Segmentation	$\Delta\eta \times \Delta\phi = 0.1 \times 0.1$ (0.05×0.05 at shower max)
Depth Segmentation	4 EM (33 χ_0), 4-5 hadronic (6 λ)
$\frac{e}{\pi}$ Response	1.02 to 1.09
Linearity	$< 0.5\%$
Electron Resolution	$\frac{0.15}{\sqrt{E}} + 0.003$
Hadron Resolution	$\frac{0.50}{\sqrt{E}} + 0.04$

Table 2.5. Calorimeter Parameters

2.3.4.1 Central Calorimeter

The Central Calorimeter (CC) is subdivided into Electromagnetic (EM), Fine Hadronic (FH) and Coarse Hadronic (CH) layers. The third EM layer is more finely segmented because typical EM shower development occurs after 10 radiation lengths. The fine segmentation allows for a more accurate measurement of shower location and shape. See 2.6 for further parameters of the CC.

2.3.4.2 End Calorimeter

The End Calorimeter (EC) is similar to the CC but EM portion of extends radially from 5.7 cm to 104 cm. The Inner Calorimeter Hadronic (ICH) placed after the EM module consists of four FH layers and one CH layer. Surrounding the ICH lies the Middle Hadronic (MCH) which consists of four FH layers and a CH layer. The Outer Hadronic (OCH) module surrounds the MCH and consists of CH layers and has angled cells to improve η coverage. Additionally,

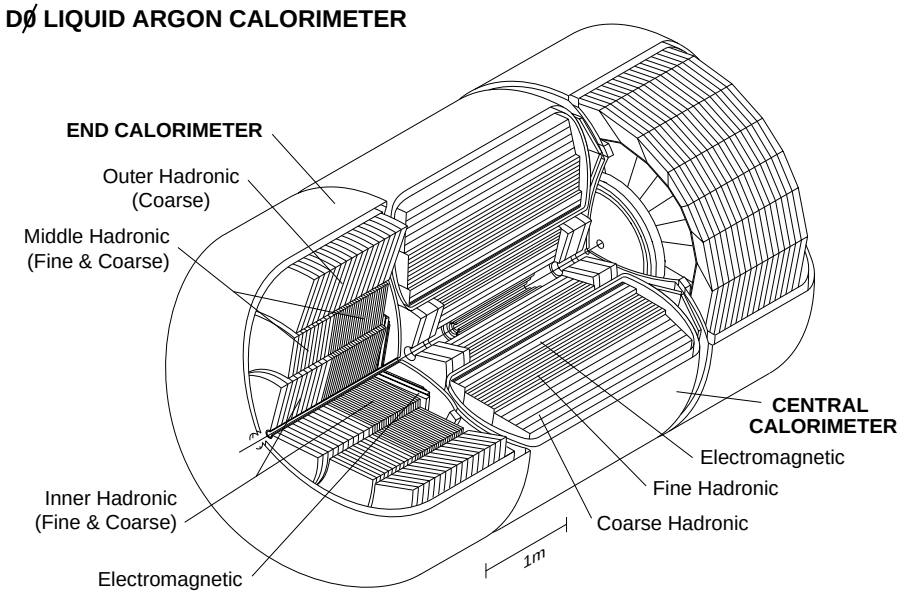

Figure 2.18. The Central Calorimeter at DØ.

segmentation near the beam pipe changes, see table 2.7 and figure 2.22 for more details.

2.3.5 Inter-Cryostat Region (ICR)

The region between 0.8 and 1.4 η is filled by the insulating bulkheads of the calorimeter, the module end plates and detector support structures. To compensate for this dead region the ICR and Massless Gap (MG) detectors were built.

The ICD is comprised of two annular scintillation tile arrays installed on the outer EC walls. The scintillating photons are guided through wavelength shifting optic fibers to photo multiplier tubes (PMT) for readout. The tiles are symmetric in ϕ and cover the range from 0.8 to 1.4 in η.

The MG detectors are mounted on the inside bulkhead surface of both the CC and EC cryostats. The MG has readout pads identical to the calorimeter modules. Unlike the calorimeter the MG has no absorber plates.

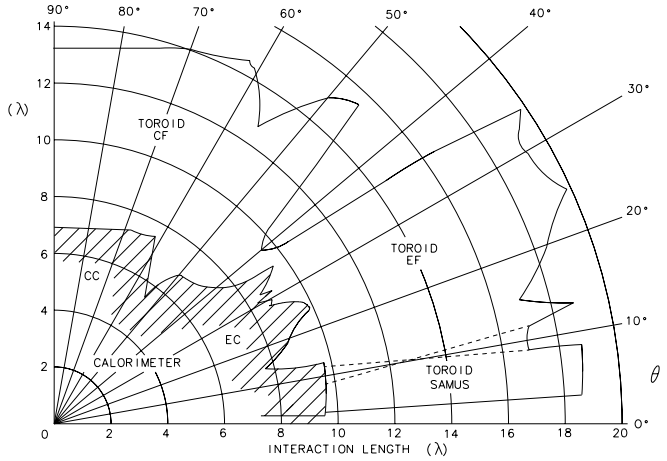

Figure 2.19. Thickness of the DØ detector as a function of θ in nuclear interaction lengths.

2.3.5.1 Muon System

The purpose of the muon system is to identify and track muons coming from the $p\overline{p}$ interaction. Since muons decay later than the hadronic and electromagnetic showers it is possible to identify muons inside the hadronic jets easier than electrons. This is extremely important in b jet identification especially since DØ does not have a magnetic field in the tracking region and cannot use the displaced vertex method.

The Muon system consists of five separate solid iron toroid magnets, with sets of Proportional Drift Tubes (PDT's). There are three layers of PDT's, the inner layer A is located before the 2 Tesla toroid. The B and C layers are located outside the toroid. This allows one measurement before the bend and two measurements after the bend. Minimum ionizing tracks in the calorimeter can confirm the existence of a muon. Timing scintillators above the detector are

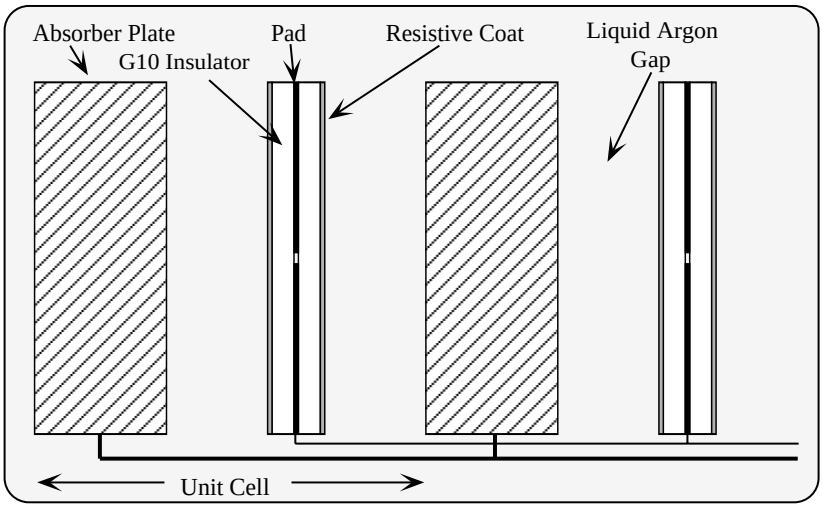

Figure 2.20. Two unit cells of the DØ Calorimeter.

used to eliminate muons from cosmic showers outside the detector. See Table 2.8 for a list of muon system parameters.

The central toroid (CF) covers the $|\eta| < 1.0$ region and is a square annulus 109 cm thick and weighing 1973 metric tons. The three layers described above along with the CF is known as the wide angle muon system or WAMUS. The two end toroids (EF) cover the $1.0|\eta| < 3.6$ region and each EF toroid weighs 800 metric tons. The small angle muons system (SAMUS) toroids fit in the central hole of the EF toroids and cover $2.5 < |\eta| < 3.6$. The SAMUS system is designed to measure muons near the beam pipe or at high η.

2.3.6 Detector Summary

The DØ Detector system is a highly versatile apparatus. Its many subsystems work together to measure a particle's position and energy. No minor feat when many different energy loss processes have to be taken into account not to mention the cost and space factors involved. The DØ Detector is capable of identification and measurement of electrons and muons and measurement of high energy jets with good energy resolution.

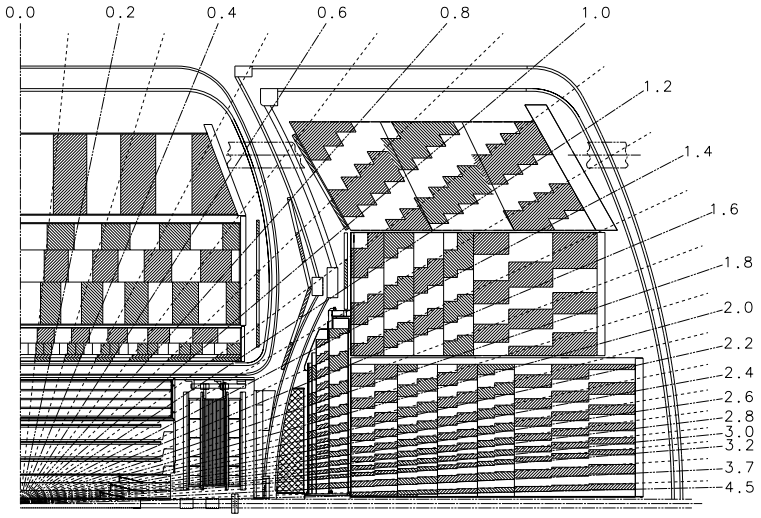

Figure 2.21. η view of the Calorimeter and Central Detector showing the tower geometry. The radial lines indicate detector pseudorapidity. The Inter Cryostat Detectors are visible as lines between 0.8 η 1.2. The Main Ring enters the Coarse Hadronic region near the top.

Central Calorimeter Parameters

	EM	FH	CH
Rapidity coverage	± 1.2	±1.0	±0.6
Number of Modules	32	16	16
Absorber	uranium	uranium	copper
Absorber Thickness(inches)	0.118	0.236	1.625
Argon Gap(inches)	0.09	0.09	0.09
Number of cells/module	21	50	9
Longitudinal depth	20.5 χ_0	3.24 λ_0	2.93λ_0
Number of readout layers	4	3	1
Cells/readout layer	2,2,7,10	20,16,14	9
Total radiation lengths	20.5	96.0	32.9
Radiation Length/cell	0.975	1.92	3.29
Total absorption lengths(Λ)	0.76	3.2	3.2
Absorption length/cell	0.036	0.0645	0.317
Sampling fraction (%)	11.79	6.79	1.45
Segmentation ($\Delta\phi$ x $\Delta\eta$)	0.1 x 0.1	0.1 x 0.1	0.1 x 0.1
Total number of readout cells	10,368	3000	1224

Table 2.6. Central Calorimeter Parameters

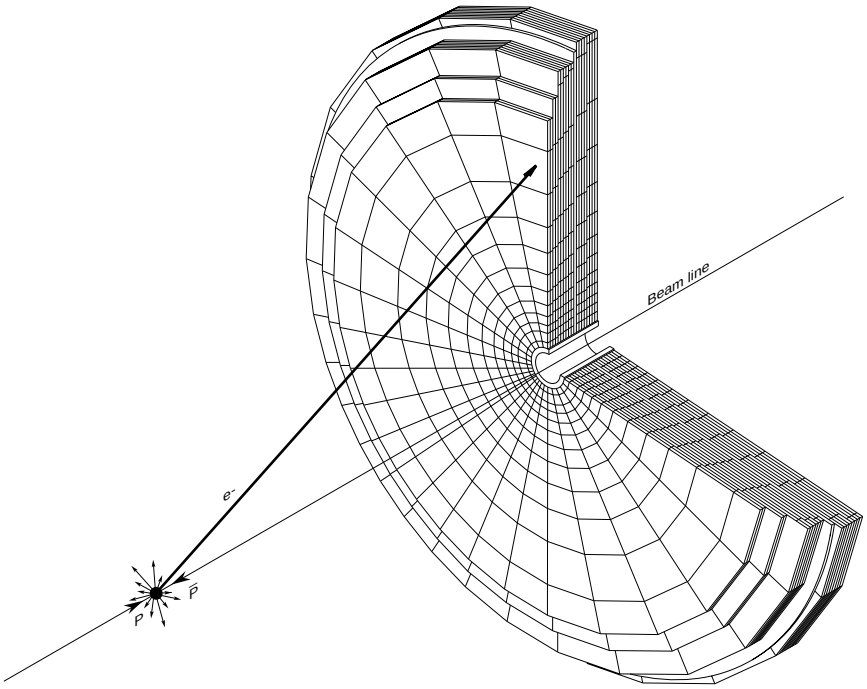

Figure 2.22. End Calorimeter Electromagnetic Module (ECEM). The readout boards form complete disks with no azimuthal cracks. The End Calorimeter Inner Hadronic (ECIH) is similar in construction.

End Calorimeter Parameters

	EM	IFH	ICH	MFH	MCH	OCH
Rapidity coverage	1.3-3.7	1.6-4.5	2.0-4.5	1.0-1.7	1.3-1.9	0.7-1.4
Number of Modules	1	1	1	16	16	16
Absorber	U	U	SS	U	SS	SS
Absorber Thickness(in)	0.118	0.236	0.236	0.236	1.83	1.83
Argon Gap(inches)	0.09	0.082	0.082	0.087	0.087	0.087
Number of cells/module	18	64	12	60	14	24
Longitudinal depth	$20.5\chi_0$	$4.4\lambda_0$	$4.1\lambda_0$	$3.6\lambda_0$	$4.4\lambda_0$	$4.4\lambda_0$
Number of readout layers	4	4	1	4	1	3
Cells/readout layer	2,2,6,8	16	14	15	12	8
Total radiation lengths	20.5	121.8	32.8	115.5	37.9	65.1
Total absorption lengths(Λ)	0.95	4.9	3.6	4.0	4.1	7.0
Sampling fraction (%)	11.9	5.7	1.5	6.7	1.6	1.6
Segmentation ($\Delta\phi$)	0.1	0.1	0.1	0.1	0.1	0.1
Segmentation ($\Delta\eta$)	0.1	0.1	0.1	0.1	0.1	0.1
Total number of readout ch	7488	4288	928	1472	384+64	896+64

Table 2.7. End Calorimeter Parameters for the Electromagnetic (EM), Inner Fine Hadronic (IFH), Inner Coarse Hadronic (ICH), Middle Coarse Hadronic (MFH) and Outer Coarse Hadronic (OCH)

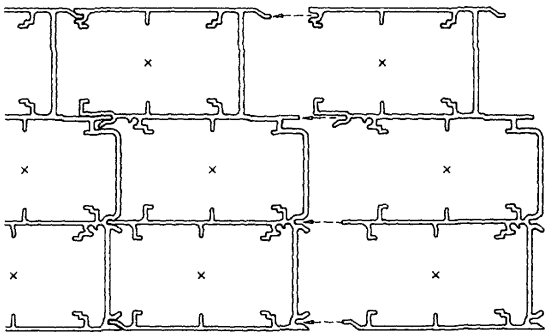

Figure 2.23. Extruded aluminum section from which the B and C PDT chambers are constructed. The A layer chamber extrusions are similar, but have four cells instead of three.

Muon System Parameters

	WAMUS	SAMUS
Rapidity coverage	$\|\eta\| \leq 1.7$	$1.7 \leq \|\eta\| \leq 3.5$
Magnetic Field	2 T	2 T
Number of Chambers	164	6
Interactions lengths	13.4	18.7
bend view resolution	± 0.53 mm	± 0.35 mm
Non-bend resolution	± 3 mm	± 0.35 mm
$\delta P/P$	18%	18%
Gas	$Ar(90\%) - CF_4(5\%)$ $-CO_2(5\%)$ $CF_4(90) - CH_4(10\%)$	
Avg. Drift Velocity	6.5 cm/μs	9.7 cm/μs
Anode Wire Voltage	4.56 kV	4.0 kV
Cathode Pad Voltage	2.3 kV	NA
Number of cells	11386	5308

Table 2.8. Muon System Parameters

CHAPTER 3

JETS

A jet is a spray of collimated particles produced when a high E_T gluon or quark hadronizes. At the Tevatron, these quarks or gluons mainly come from hard scattering of the partons from the proton and antiproton but they also may come from the underlying event. The underlying event is made up of quarks or gluons from the original hadrons (proton–anti-proton) that did not hard scatter and may show up as jets in the event. Since, there is no way to experimentally separate these two types of jet a standard jet definition is used so that experimental results can be compared to theoretical predictions. The Snowmass Jet Algorithm [23–24] was adopted for this purpose.

A "jet" can refer to calorimeter, particle and parton jets. Calorimeter jets are jets that are reconstructed from energy deposits within the calorimeter. Particle jets are jets arising after hadronization without detector effects. Parton jets are produced before hadronization. The calorimeter jets (data) in this analysis will be compared to particle level signal and background Monte Carlo simulations. This requires that the calorimeter jets be corrected back to the particle level, this is done using the jet energy scale to be discussed later in this chapter. Figure 3.1 shows the various types of jets.

3.1 The Snowmass Jet Definition

The Snowmass Jet Algorithm defines a jet as a collection of partons, particles, or calorimeter cells contained within a cone opening angle $\mathcal{R}$, where $\mathcal{R}_i$ =

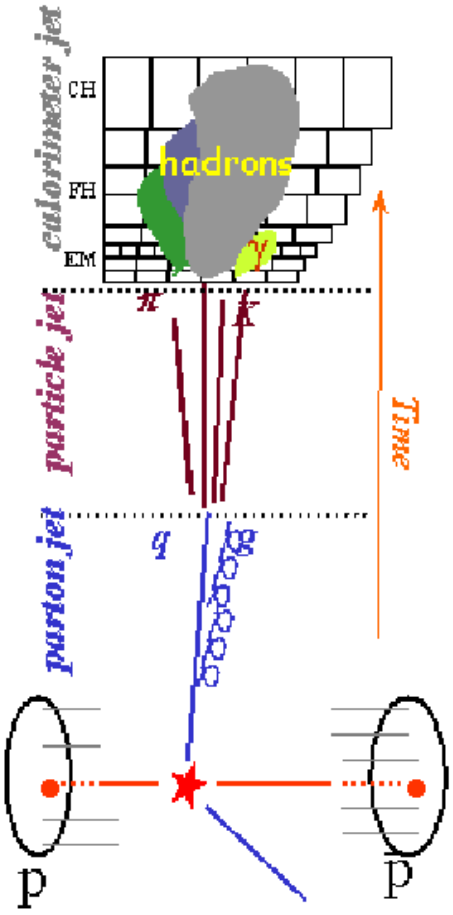

Figure 3.1. A representation of parton, particle and calorimeter level jets.

$\sqrt{(\eta_i - \eta_{jet})^2 - (\phi_i - \phi_{jet})^2}$. η_{jet} and ϕ_{jet} define the direction of the center of a jet and η_i and ϕ_i are the coordinates of the parton, particle or center of the calorimeter cell. If $\mathcal{R}_i \leq \mathcal{R}$ then the object is part of the jet. In this analysis $\mathcal{R} = 0.7$. The E_T and the direction of the jet are

$$\begin{aligned} E_T &= \sum_{i \in \mathcal{R}_i \leq \mathcal{R}} E_T^i \\ \eta_{jet} &= \frac{1}{E_T} \sum_{i \in \mathcal{R}_i \leq \mathcal{R}} E_T^i \eta^i \\ \phi_{jet} &= \frac{1}{E_T} \sum_{i \in \mathcal{R}_i \leq \mathcal{R}} E_T^i \phi^i, \end{aligned} \tag{3.1}$$

where i is the ith parton or cell.

The Snowmass algorithm:

- Calculate a list of seeds with a location η_{jet} and ϕ_{jet}.
- Make a jet cone with direction η_{jet} and ϕ_{jet}.
- Recalculate the direction of the jet.
- Repeat jet forming and direction recalculation until the jet direction is stable.

3.2 The DØ Jet Definition

The DØ jet algorithm collects energy deposits within the calorimeter into clusters. Then, the direction and the transverse energy E_T are determined.
The DØ algorithm:

- Calorimeter towers with $E_T > 1$ GeV are ranked by E_T. A calorimeter tower consists of four calorimeter cells with dimensions of $\Delta\eta \times \Delta\phi = 0.2 \times 0.2$. The highest E_T tower forms the first seed around which preclusters are formed.
- The jet direction is determined by equation (3.2), with energy from a cone of size $\mathcal{R}$ around the precluster's original center.
- The energy deposited within the cone is calculated using the Snowmass definition, equation 3.1.
- The previous step is recalculated until the jet direction is stable. This occurs in about 2-3 iterations.
- Jets with $E_T > 8$ GeV are kept.
- Jets are merged and split accordingly.

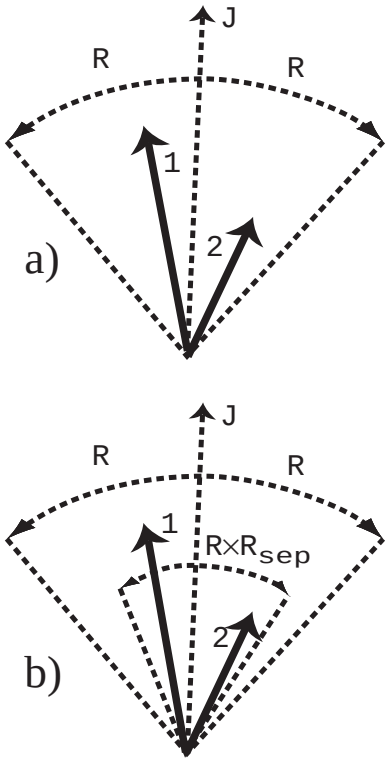

Figure 3.2. Illustration and description of the jet definitions at NLO parton level as used by the DØ experiment. (a) The jet definition in NLO according to Snowmass. Parton -1- and -2- are combined into jet -j-, if the parton distance to the jet axis is less than R. The jet axis is defined by partons 1 and 2, according to the Snowmass definition. (b) The jet definition in NLO according to the modified Snowmass definition with $\mathcal{R}_{sep}$. Use the standard Snowmass clustering but in addition require the distance between the two partons be less than $\mathcal{R} \times \mathcal{R}_{sep}$.

The final direction of the jet is calculated differently than the Snowmass algorithm. At DØ the final direction is calculated as follows:

$$\begin{aligned} \theta_{jet} &= \tan^{-1}\left[\frac{\sqrt{(\sum_i E_x^i)^2 + (\sum_i E_y^i)^2}}{\sum_i E_z^i}\right], \\ \phi_{jet} &= \tan^{-1}\frac{\sum_i E_y^i}{\sum_i E_x^i}, \\ \eta_{jet} &= -\ln\tan\left(\frac{\theta_{jet}}{2}\right). \end{aligned} \tag{3.2}$$

3.2.1 Merging and Splitting

In perturbative QCD calculations of parton-parton scattering at leading order only two partons exist in the final state. These partons are well separated and form two jets when using the Snowmass algorithm. At NLO three partons can be formed in the final state. For example if three jets are formed and two are not well separated, then these two partons seed directions are calculated by applying equation 3.1 in the Snowmass definition. If the partons are within a distance $2\mathcal{R}$ from the seed's direction then the two partons are added together (merged) to form one jet. See figure 3.2a for an illustration of the Snowmass algorithm at NLO. In such a case, the DØ algorithm will produce either one or two jets depending on the splitting and merging rules for calorimeter jets. This illustrates the different treatment of jets at the parton and calorimeter level. To address this jet difference a purely phenomenological parameter has been suggested, $\mathcal{R}_{sep}$. $\mathcal{R}_{sep}$, is the maximum allowed distance ($\delta\mathcal{R}_{sep}$) between two partons in a parton jet, divided by the cone size of the jet,

$$\mathcal{R}_{sep} = \frac{\delta\mathcal{R}}{\mathcal{R}}. \tag{3.3}$$

This is illustrated in fig 3.2b and is known as the modified Snowmass algorithm. After many studies on $\mathcal{R}_{sep}$ a value of 1.3 was found to best simulate DØ merging and splitting rules [25].

The differences in jet direction between the Snowmass definition and the DØ definition were studied [23] and ($|\eta_{snowmass} - \eta_{D\emptyset}|$) < 0.015 for $|\eta| < 1$, see figure 3.3.

3.3 Jet Corrections

Corrections are needed to make the energy of a calorimeter jet correspond to the final state particle jet energy. The jet energy scale is the largest and most important correction made to jets at DØ . The jet energy scale is an

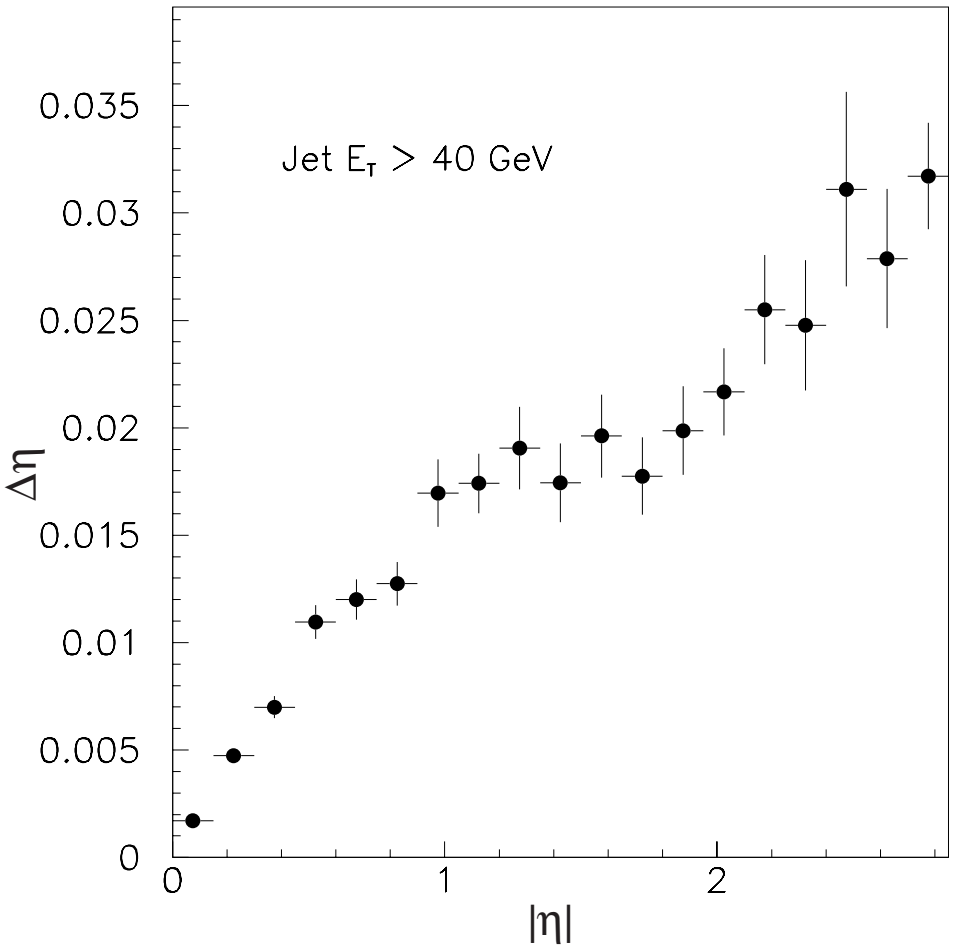

Figure 3.3. The average difference between the $|\eta|$ of jets reconstructed using the DØ algorithm and the Snowmass algorithm for the DØ data.

average correction binned in energy, and pseudo-rapidity. A detailed discussion of this correction can be found in References [26–28]. This section serves as a general overview of the correction. This analysis uses CAFIX 5.1 (Calorimeter Fix Package, version 5.1), a DØ run I jet energy scale correction routine [29]. Once the jet energy scale correction is made, jet energy distributions are smeared by resolution effects. Due to the almost hermetic nature of the DØ calorimeter the jet energy scale correction and the Jet Energy resolutions can be separated. The jet energy resolutions will be discussed in Chapter 5.

3.4 Jet Energy Scale

The original derivation of the jet scale was based solely on calibrations made from "test beam" data. The test beam project attempted to measure the absolute scale of a measured calorimeter cell charge relative to the true particle energy deposited in the calorimeter. This was accomplished by directing particles of known energy into several calorimeter modules. Several factors prevent test beam data from being a perfect model of the DØ calorimeter. Specifically, the test beam did not model the poorly instrumented regions of the current detector, off center cell hits, electronic noise from the $p\overline{p}$ beam and the underlying event. These corrections are not made online or during event reconstruction due to speed issues. These corrections are made offline during the analysis phase.

The true jet energy E_{jet}^{ptcl} is obtained from E_{jet}^{meas} by the following relationship:

$$E_{jet}^{ptcl} = \frac{E_{jet}^{meas} - E_O(\mathcal{R}, \eta, \mathcal{L})}{R_{jet}(\mathcal{R}, \eta, E) R_{cone}(\mathcal{R}, \eta, E)}, \tag{3.4}$$

where:

- $\mathcal{R}$ is the cone size; $\mathcal{L}$ is luminosity.
- $E_O(\mathcal{R}, \eta, \mathcal{L})$ is an energy offset, which includes the effects of the underlying event, uranium noise, energy from previous crossings (pile-up) and the underlying event contributions of extra interactions.
- $R_{jet}(\mathcal{R}, \eta, E)$ is the calorimeter response and is a measure of how the calorimeter measures electromagnetic objects compared to hadronic objects (e/h).
- $R_{cone}(\mathcal{R}, \eta, E)$ is the fraction of the jet shower contained in the algorithm cone.

3.4.1 Response

The energy response is the amount of energy measured versus the true energy of the particle. The response differs from the true energy due to energy losses in sparsely instrumented regions and the differences in electromagnetic and hadronic particle showering ($\frac{e}{h} > 1$). The response is cone size independent but its parameterization depends on cone size since a larger cone encompasses more energy. The response is η dependent because of the specific locations of various detector variations. For example, the effective absorber plate and ionization gap thicknesses depend on η. Most importantly, the response is energy dependent.

Jet energy response was directly measured at DØ making use of the important fact that transverse momentum is conserved in γ-jet events. Since photons and electromagnetic particles in general deposit energy in a mostly linear manner, events with one photon and one jet provide a good way to measure a jet's lost energy or response. The photon energy scale is set by Z to e^+e^-, J/ψ and π^0 resonances. The jet transverse energy measured in the calorimeter must balance the well measured photon energy. The method used to make this response measurement is called the Missing E_T Projection Fraction method (MPF). Using the vector quantities of the transverse energy of the photon and jet then the response is as follows:

$$\overrightarrow{E_T^{\gamma}} + R\overrightarrow{E}_T^{jet} = -\overrightarrow{\not\!\!E_T}, \tag{3.5}$$

where R is the response. If you define n_γ along the transverse direction of the photon then

$$E_T^{\gamma} + R\hat{n}_\gamma \cdot \overrightarrow{E_T}^{jet} = -\hat{n}_\gamma \cdot \overrightarrow{\not\!\!E_T}. \tag{3.6}$$

In a two body system, conservation of momentum means $E_T^{\gamma} = -n_\gamma \cdot E_T^{jet}$. Then

$$R = 1 + \frac{\hat{n}_\gamma \cdot \overrightarrow{\not\!\!E_T}}{E_T^\gamma} = 1 + MPF. \tag{3.7}$$

This method becomes complicated by the fact that energy response varies with energy not transverse energy and photon events may contain additional jets that do not meet the threshold energy of the detector. Finally, jet measurements are affected by resolution smearing effects. Resolution smearing effects are reduced by using the jet energy estimator. The jet energy estimator is highly correlated to the measured energy, E^{meas} but is measured with a much higher accuracy. The jet energy estimator is

$$E' = E_T^\gamma \cdot cosh(\eta^{jet}) \tag{3.8}$$

.

See figures 3.4 and 3.5 for plots of the response. See references [9, 26–28] for further discussion of response and this correction.

3.4.2 Offset Correction

The offset corrects for energy that is not part of the high-p_T interaction. The total offset correction is measured as a transverse energy density in $\eta - \phi$ space and broken down into, $D_0 = D_{ue} + D_\Theta$, where D_{ue} is the contribution due to the underlying event, or the energy associated with the spectator partons in the $p\overline{p}$ event, and D_Θ represents the effects of uranium noise, pile-up and energy from additional $p\overline{p}$ interactions. The offset correction E_0 is given by D_0 multiplied by η–ϕ area of the jet.

D_Θ is obtained from a zero bias sample, which is a random sampling of the detector during a beam-beam crossing. D_{ue} is determined by the difference in average transverse energy density between minimum bias events (events in which a $p\overline{p}$ collision has occurred) and zero bias events. The η dependence of D_Θ and

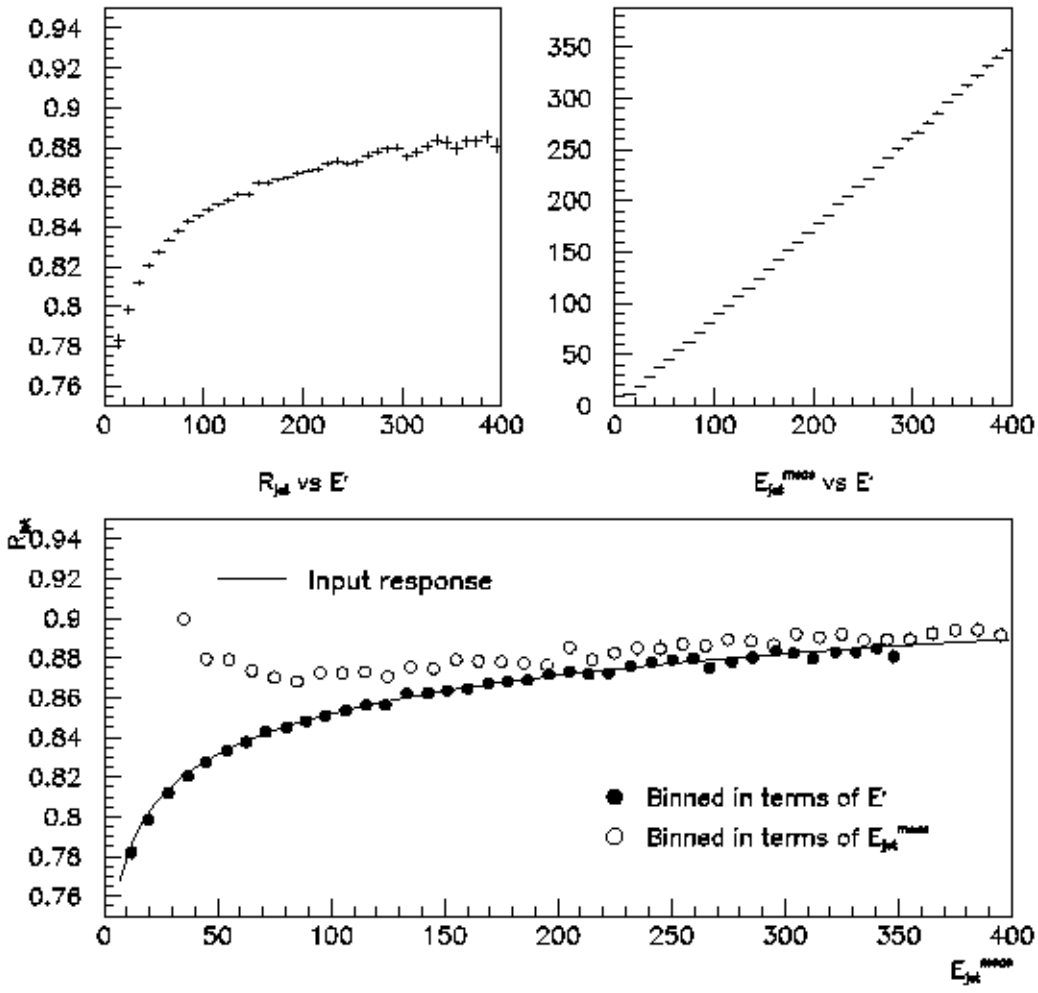

Figure 3.4. (Top) Response versus the energy estimator and the measured jet energy versus the energy estimator. (Bottom) Parametric simulation of the jet response. Open circles are response binned with measured jet energy, E_{jet}^{meas}. Filled circles response binned in terms of the energy estimator, E'.

D_{ue} and the luminosity dependence of D_{Θ} are shown in figures 3.6 and 3.7 [23].

Calorimeter noise is composed of uranium noise, which is the result of nuclear activity in the depleted uranium plates inside the calorimeter. The online data collection system only stores information that is consistent with energies above the average uranium noise thus reducing storage space. The energy distribution

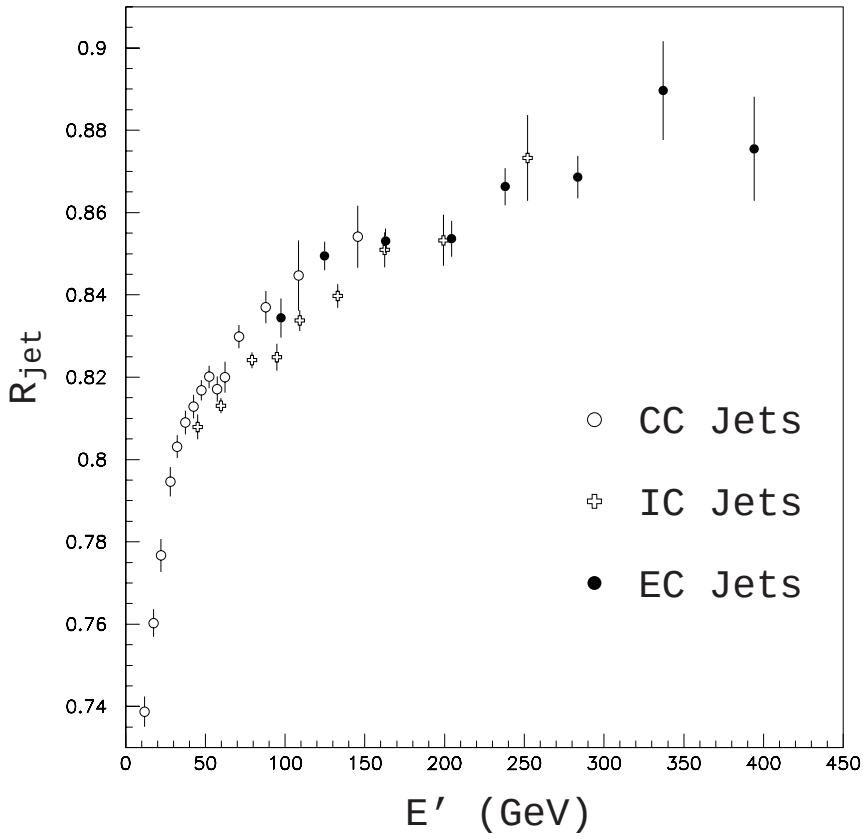

Figure 3.5. The DØ calorimeter response for the central calorimeter (CC) (open circles) and end cap (EC) (filled circles) and intercryostat (IC) (open crosses).

for the uranium noise is not quite Gaussian therefore the correction for this effect will not remove all of the noise. Figure 3.8 shows an example of a skewed Gaussian. The mean is zero though the peak is off center. After removal of the energy between the vertical lines the mean is not zero for the remaining distribution.

Pile-up is energy left over from previous $p\overline{p}$ interactions. Pile-up occurs because of the long shape times in the calorimeter readout cells. This effect is luminosity dependent. The energy of each cell is measured before and after each beam crossing. The difference in the charge density of these two measurements translates into the measured cell energy. This is known as the baseline subtraction scheme (BLS). The problem is that ionization electrons in

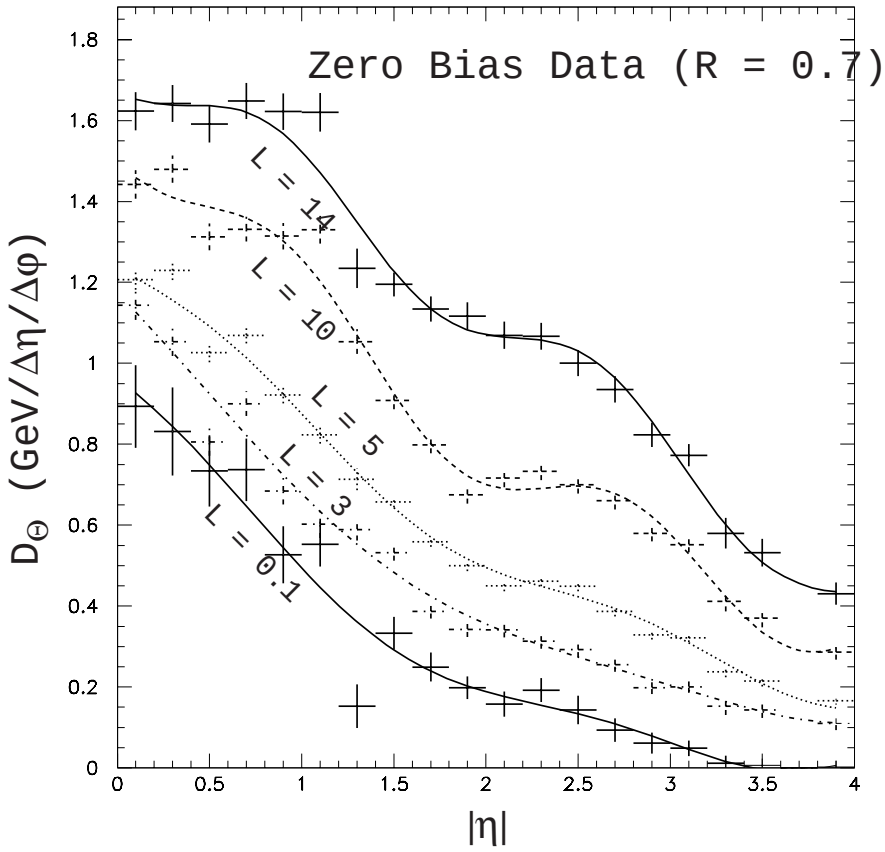

Figure 3.6. D_Θ versus η for different luminosities in units of $10^{30}\ cm^{-2}\ sec^{-1}$.

each cell take more time than the beam crossing to collect. This results in a net negative energy effect from prior crossings. This effect is both luminosity and pseudo-rapidity dependent.

3.4.3 Showering Correction

The showering correction compensates for the energy of the jet lost outside the jet cone or energy gained when the cone overlaps with another jet. The theoretical jet cross section predictions do not include showering effects, the data needs to be corrected back to the same conditions which is known as the particle level. Test beam analysis shows that on average 99.5% of a jet's energy is encompassed within a 0.4 cone. Accordingly, a cone of radius 1 should encompass

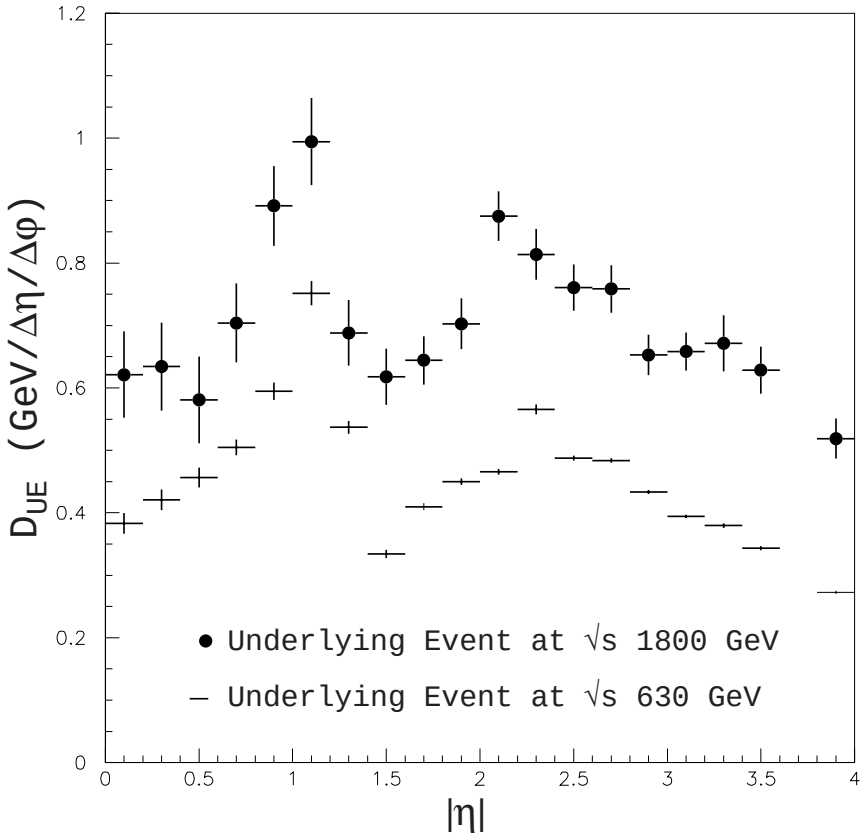

Figure 3.7. The underlying event E_T density D_{ue} versus η for $\sqrt{s}$ = 1.8 TeV and 630 GeV.

all of the secondary particles. The following ratio

$$F_{data} = \frac{E_{R=1.0}}{E_{R=.7}}, \tag{3.9}$$

represents the out of cone correction but it is not possible with data to distinguish true out-of-cone energy or energy from particles outside the cone that deposit energy within the cone.

Monte Carlo data was used to determine this factor in more detail, and

$$\begin{aligned} F_{data} &= \frac{J_7 + \text{true out-of-cone} + \text{net showering Loss}}{J_7}, \\ &= \frac{J_7 + \text{Out} + \text{L}}{J_7}, \end{aligned} \tag{3.10}$$

where J_7 is the energy within the R=0.7 cone. The definition of "true out-of-cone" indicates energy from particles whose vectors were not inside the cone

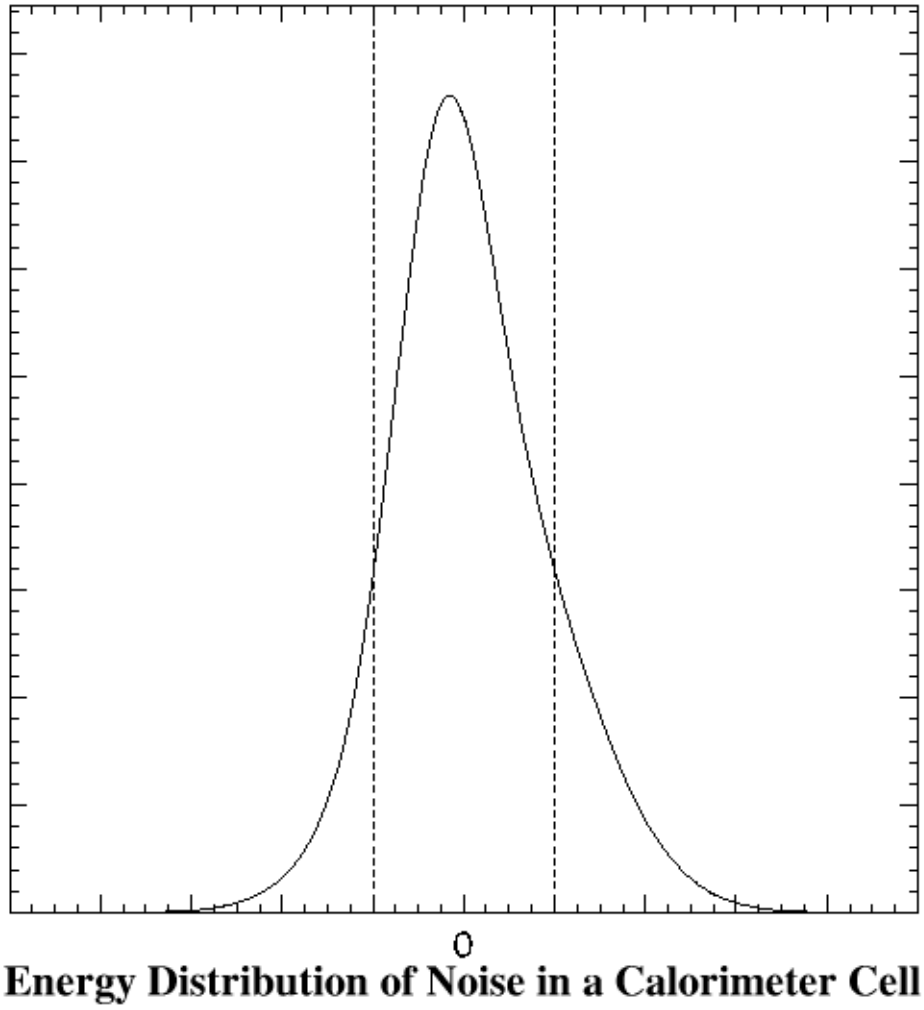

Figure 3.8. Example of a Gaussian skewed by suppression noise. The removal of the portion between the vertical lines results in a non-zero mean.

boundary, and therefore should not be recovered. Measurement of F_{data} indicates that 96.8% of all energy within a R=1.0 lies within the 0.7 cone boundary [9].

3.5 Summary

The jet energy scale corrects for offset, response and showering terms. Uncertainties in the jet energy scale dominate the uncertainty in the final jet cross section. At the lower end of the jet energy spectrum ($\approx$ 250) GeV uncertainty

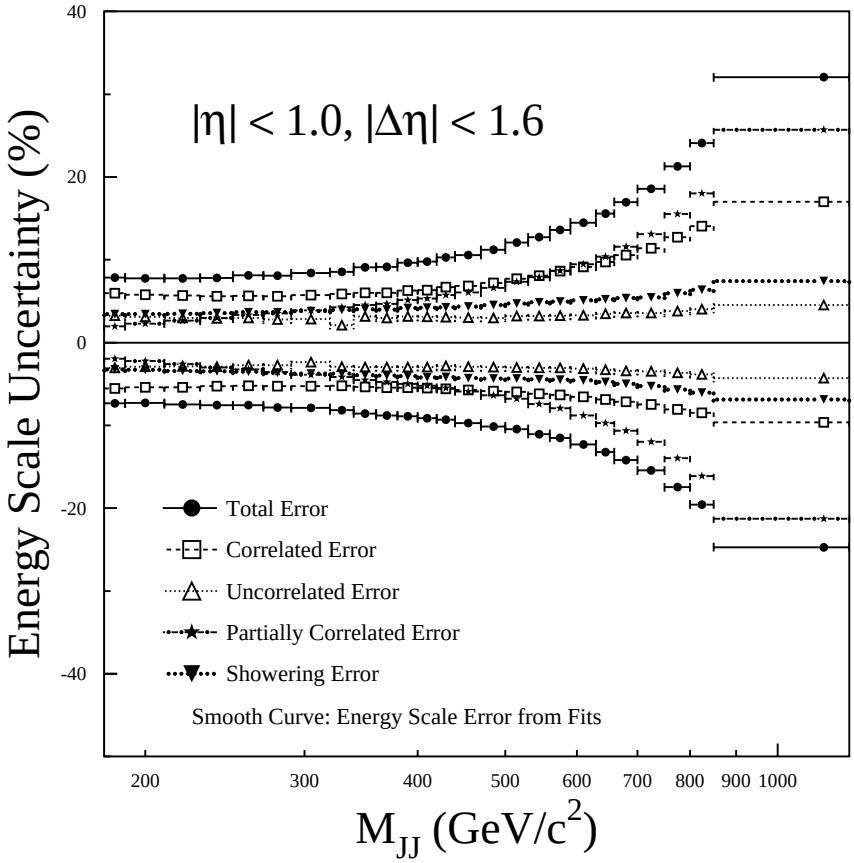

Figure 3.9. The jet energy scale Uncertainties.

in the offset term dominates; at higher energies, uncertainty in the response term dominates. See figure 3.9 for uncertainties in the jet energy scale for dijet masses.

CHAPTER 4

DATA

In a typical run, six proton and six antiproton bunches are accelerated up to 900 GeV and then are focused by the low beta quadrapoles into the collision areas at CDF and DØ. Once the bunches are steered into the collision area the scintillating hodoscopes of Level Ø determine if a hard collision has occurred. Once an event has occurred, then signals from the detector are sent to digital logic circuits consisting of logical AND/OR gates which analyze each crossing, searching for pre-specified "events" that pass certain criteria. This is known as the Level 1 trigger. If an event passes Level 1 it is sent to the VAX workstations, where additional constraints are applied with algorithm software; this is known as the Level 2 trigger. If the Level 2 requirements are met the event is saved to tape for further analysis. The set of hardware and software event selection rules are known as the trigger list.

This chapter will introduce the specific trigger levels, outline the luminosity calculation, and discuss triggers and selection rules for dijet events.

4.1 Trigger Levels

Since the rate at which events can be written to tape (bandwidth) is limited DØ uses three trigger levels to obtain the desired events. The first level, Level Ø determines if a hard scattering has occurred and is purely a hardware trigger. The second level, Level 1, consists of a hardware logic circuits and looks for interesting events without the tracking information which takes too long for this

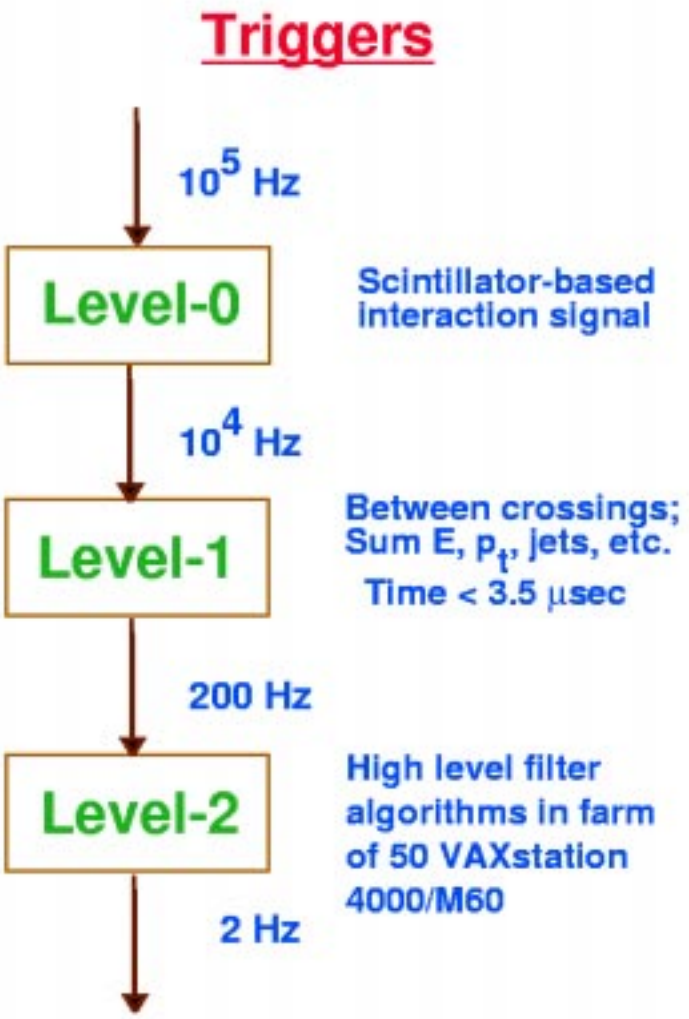

Figure 4.1. The Level Ø, 1 and 2 triggers and their trigger rates.

trigger to gather, more than 3.5 μsec. The final trigger layer, Level 2, is a software trigger and can identify electron, jet, muon and photon objects using custom software algorithms. The Level 2 triggers for this analysis are the specific jet triggers: $Jet_{30}, Jet_{50}, Jet_{85}$ and Jet_{115} which will be discussed later in this chapter. These successive trigger levels reduce the raw event rate from 300kHz down to 2Hz after Level 2, see figure 4.1.

4.1.1 Level Ø

Level Ø is comprised of the twin scintillating hodoscope arrays discussed in the detector chapter. This trigger is the basis for most of the DØ data triggers. For each beam crossing every 3.5 μs the LØ trigger indicates if an inelastic collision has occurred. These hodoscopes partially cover an η range of $1.9 < |\eta| < 4.3$ with almost complete coverage between $2.2 < |\eta| < 3.9$. This is required for providing greater than 99% efficiency in detecting non-diffractive inelastic collisions [30].

Final state particles from spectator partons or the underlying event tend to have low angle trajectories. If both hodoscopes detect these particles within a small amount of time then the event passes. In addition to indicating that an inelastic collision has occurred the LØ trigger provides timing information for determining the position of an event in z. Without the Level Ø trigger the bandwidth into the Level 1 trigger would be equal to the beam crossing rate of 286 kHz. With Level Ø this is reduced to 17 kHz.

4.1.2 Level 1

Level 1 is a quick hardware logic trigger that filters the data stream for interesting physics. This trigger works within the 3.5 μsecs between beam crossings. Information from calorimeter trigger towers and muon hits are used.

A calorimeter trigger tower consists of 2×2 array of calorimeter towers. For example a jet trigger might require a trigger tower with at least 2 GeV of transverse energy in an event. Higher E_T triggers use larger tiles which are entire quadrants of the detector to make these calculations.

If a Level 1 trigger rate is too high, a prescale is used to reduce the rate to an acceptable value. There is also a Level 1.5, primarily used by muon triggers, which uses the muon system to calculate muon momentum without use of the tracking system. Events passing Level 1 are sent to Level 2.

Trigger Thresholds

Trigger	L1 E_T (GeV)	L2 E_T (GeV)	$\mathcal{L}$ (pb^{-1})	Error (%)	Leading Jet E_T cut
JET_30	1 tile $>$ 15 and 1 tile $>$ 6	30	0.36	7.8	45
JET_50	1 tile $>$ 15 and 1 tile $>$ 6	50	4.84	7.8	75
JET_85	1 tile $>$ 35 and 1 tile $>$ 6	85	56.48	5.8	105
JET_115	1 tile $>$ 45 and 1 tile $>$ 6	115	94.87	5.8	170
JET_115(Ia)	1 tile $>$ 45 and 1 tile $>$ 6	115	14.15	5.8	170

Table 4.1. Run Ib triggers Jet_30, Jet_50, Jet_85 and Jet_115 and Run Ia trigger for Jet_115. The leading jet E_T cut ensures a 95 % jet efficiency.

4.1.3 Level 2

Level 2 performs an online reconstruction of the event. It uses 48 VAX workstations working in parallel using customized fast software algorithms to identify objects as electrons, jets, muons or photons [9]. Level 2 uses all information from the detector but object definitions are simplified for faster decisions.

A fast jet algorithm was used at L2; the Level 2 jet trigger receives a list of candidate calorimeter trigger towers from Level 1. The trigger tower candidates, or seeds, are trigger towers whose total E_T is greater than a seed threshold. The Level 2 trigger seed threshold is $E_T > 6$ GeV. The E_T weighted centroid of cells in the vicinity of the seed is the Level 2 center, (η_0, ϕ_0). All towers within $\mathcal{R} < .7$ of this center become a Level 2 jet, where $\mathcal{R} = \sqrt{(\eta_0 - \eta)^2 + (\phi_0 - \phi)^2}$. In order for a jet to pass a specific trigger, JET_X, the summed E_T within the Level 2 jet must be larger than X GeV. The L2 triggers used in this analysis were JET_30, JET_50, JET_85 and JET_115, see table 4.1. A tile is a grouping of calorimeter cells within an area of $\Delta\eta \times \Delta\phi = 0.8 \times 1.6$. These triggers are known as the inclusive jet triggers. For a more complete discussion of Run Ib triggers see [31].

4.1.4 Trigger Efficiencies

A study was done to determine the trigger efficiencies for the jet triggers. The total efficiency is given by the efficiency of an event passing the Level 1 trigger times the efficiency the event will pass the Level 2 trigger [23, 32]:

$$\epsilon_{event}^{total} = \epsilon_{event}^{L1} \times \epsilon_{event}^{L2|L1}, \tag{4.1}$$

where $\epsilon_{event}^{L2|L1}$ is the probability for passing Level 2 given that Level 1 was already passed. The most restrictive trigger's efficiency is the product of the probabilities of all less restrictive triggers. For example,

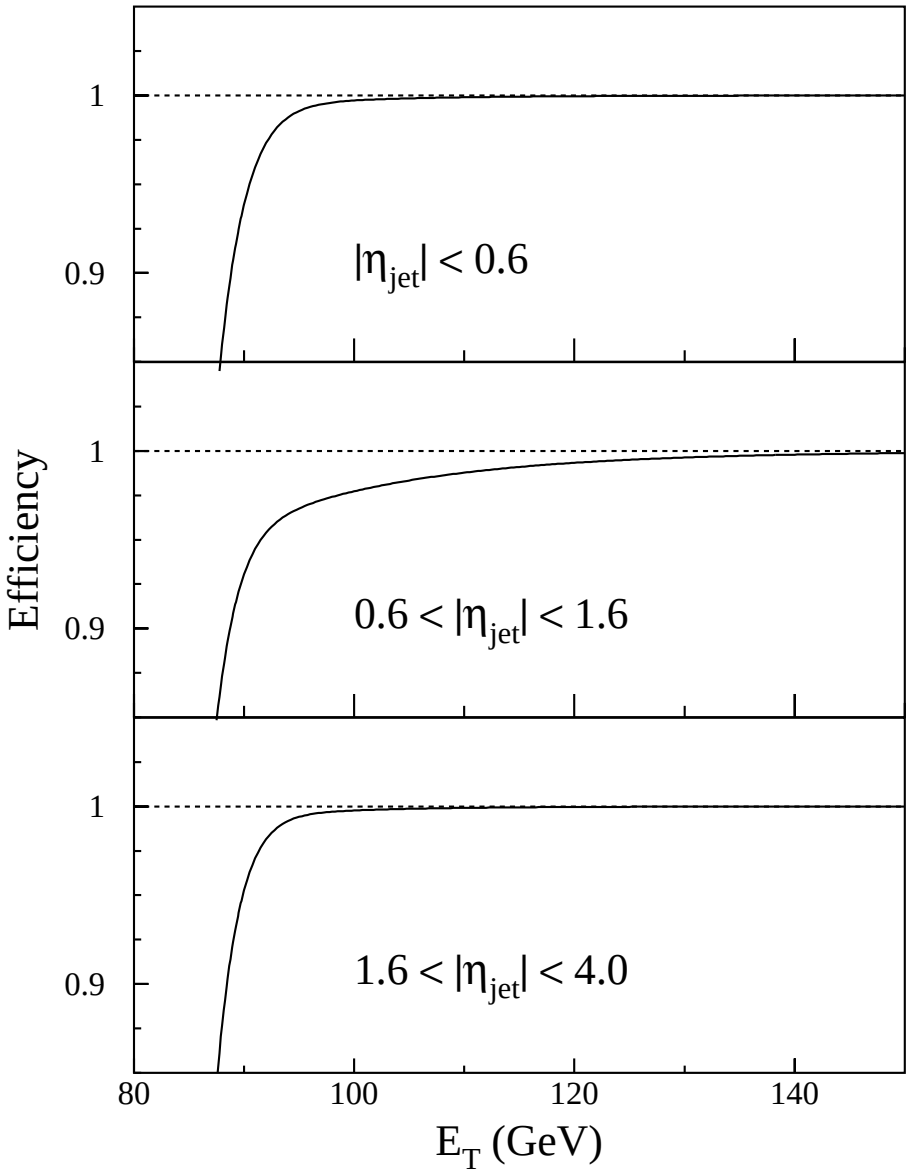

Figure 4.2. The trigger efficiencies for the Jet_85 trigger per transverse energy of the leading jet for different η ranges. Notice the trigger does not become fully efficient until the energy of the leading jet is much greater than 85 GeV.

$$\epsilon^{L1}_{Jet\_85} = \epsilon^{L1}_{Jet\_85,Jet\_50} \times \epsilon^{L1}_{Jet\_50,Jet\_30} \times \epsilon^{L1}_{Jet\_30,L\emptyset} \tag{4.2}$$

The E_T of the leading jet must be well above the trigger cut-off to be fully efficient. Figure 4.2 shows the example of the Jet_{85} trigger efficiency per E_T for various η cuts. In table 4.1 leading jet energy cut-offs that make trigger efficiencies greater than 98% are shown. Specific dijet mass cut-offs which depend on the single jet efficiency and trigger efficiencies for this analysis will be discussed in Section 4.3.

4.2 Luminosity Calculation at DØ

The beam luminosity is calculated from the counting rate of the Level Ø (LØ) counters and the cross section of these counters. The cross section is determined using the geometric acceptance of the LØ hodoscopes, the LØ hardware efficiency, and the world average of the $p\overline{p}$ inelastic cross section measurements. The effective luminosity is determined independently for each trigger on a run-by-run basis taking into account each trigger's prescale, the LØ inefficiency, and the detector dead-time [23, 33]. The measured integrated luminosities with uncertainties for each trigger used in this analysis are listed in Table 4.1.

This section will discuss instantaneous luminosity or the number of $p\overline{p}$ crossings that occur in the beam per second. The second quantity to be discussed in this section is integrated luminosity or the total number of crossings that were observable by the detector during the full data collection period.

Not every crossing produces an observable event because the DØ detector has a certain acceptance and the total $p\overline{p}$ cross section is finite. The instantaneous luminosity $\mathcal{L}$ is related to the counting rate $R_{L\emptyset}$ by

$$\mathcal{L} = \frac{R_{L\emptyset}}{\sigma_{L\emptyset}} \tag{4.3}$$

$\sigma_{L\emptyset}$ is the cross section subtended by the L$\emptyset$ hodoscope counters and is known as the luminosity monitor constant. This equation holds only if the counting rate does not contain multiple interactions. As the luminosity increases the probability of multiple interactions increases. With multiple interaction corrections, $\sigma_{L\emptyset}$ is given by

$$\sigma_{L\emptyset} = \epsilon_{L\emptyset} f_{halo} f_{MSD}(\epsilon_{SD}\sigma_{SD} + \epsilon_{DD}\sigma_{DD} + \epsilon_{HC}\sigma_{HC}) \tag{4.4}$$

where

- σ_{SD} is the single diffractive or single scattering cross section.
- σ_{DD} is the double diffractive or double scattering cross section.
- σ_{HC} is the hard core of the total inelastic cross section(σ_{inelas}).
- $\epsilon_{SD}, \epsilon_{DD}$ and ϵ_{HC} are the acceptances for single diffractive, double diffractive and hard core event acceptances, respectively.
- f_{halo} is a correction factor for beam halo interaction.
- f_{MSD} is a correction factor for multiple single diffraction, or the simultaneous detection of two different single diffractive events in opposite side detectors.
- $\epsilon_{L\emptyset}$ is the trigger or hardware efficiency of L$\emptyset$.

During each bunch crossing, zero, one or more interactions may occur and the Level $\emptyset$ hodoscopes cannot distinguish between the different interactions so the actual event rate R must be inferred from the $R_{L\emptyset}$ rate. Using Poisson statistics,

given the average number of interactions per beam crossing μ the probability of zero interactions is given by

$$P_0 = e^{-\mu}, \tag{4.5}$$

and the Level Ø counting rate is

$$R_{L\emptyset} = \frac{1 - P_0}{\tau} \tag{4.6}$$

where τ is the time between bunch crossings, 3.5 μs. R can be expressed as

$$R = \frac{\mu}{\tau} = \frac{-ln(1 - R_{L\emptyset}\tau)}{\tau}. \tag{4.7}$$

Then the luminosity is finally,

$$\mathcal{L} = \frac{-ln(1 - R_{L\emptyset}\tau)}{\sigma_{L\emptyset}\tau}. \tag{4.8}$$

The number of events expected over a period of time can be expressed as follows,

$$N = \sigma \int \mathcal{L}dt, \tag{4.9}$$

where $\int \mathcal{L}dt$ is the integrated luminosity. The integrated luminosity for this study is 109 pb^{-1} which is the sum of the luminosities for Run Ib (95 pb^{-1}) and RunIa (14 pb^{-1}). The techniques for determining this luminosity are described in the following sections.

4.2.1 $p\overline{p}$ World Average Cross Section, Geometric Acceptance (LØ) and Hardware Efficiency

The world average $p\overline{p}$ cross section was measured at $\sqrt{s}$ =546 and 1800 GeV [23, 34]. The world average for $\sqrt{s} = 1800$ GeV was determined using data from E710 [35], CDF [36] and E811 [37]. See figure 4.3 for three fits to the world average cross section.

SD acceptance ϵ_{SD}	15.1%	$\pm$	5.5%
DD acceptance ϵ_{DD}	71.6%	$\pm$	3.3%
HC acceptance ϵ_{HC}	97.1%	$\pm$	2.0%
SD cross section σ_{SD}	9.54 mb	$\pm$	0.43 mb
DD cross section σ_{DD}	1.29 mb	$\pm$	0.20 mb
HC cross section σ_{HC}	46.56 mb	$\pm$	1.63 mb
Total inelastic cross section σ_{inelas}	57.39 mb	$\pm$	1.69 mb
LØ trigger efficiency $\epsilon_{L\emptyset}$	90.7%	$\pm$	1.7%
Beam Halo and MSD corrections $f_{halo} \times f_{MSD}$	99.97%	$\pm$	0.20%
$\sigma_{L\emptyset}$	43.1 mb	$\pm$	1.9 mb

Table 4.2. Values used in the $\sigma_{L\emptyset}$ calculation. All entries obtained from references [33] appendix A except for $\sigma_{L\emptyset}$ and $\epsilon_{L\emptyset}$ which are obtained from table 1 of the same reference.

Monte Carlo studies determine the acceptances of the Level Ø hodoscopes by calculating the probability that one or more charged particles will pass through the scintillating tiles. See reference [30] for a description of this study. Table 4.2 lists the values for $\epsilon_{SD}, \epsilon_{DD}$ and ϵ_{HD}.

The method used to evaluate the Level Ø hardware efficiency is discussed in reference [33]. $\epsilon_{L\emptyset}$ is defined as the efficiency with which the LØ trigger fires on a single, inelastic interaction. This efficiency should be mostly luminosity independent and is shown in Table 4.2.

4.2.2 Multiple Single Diffractive Correction (f_{MSD})

The calculation of the geometric acceptance assumes that all events are single diffractive events. A single diffractive event has a low probability of firing both LØ hodoscopes because the trajectory of the non-fragmented particle escapes

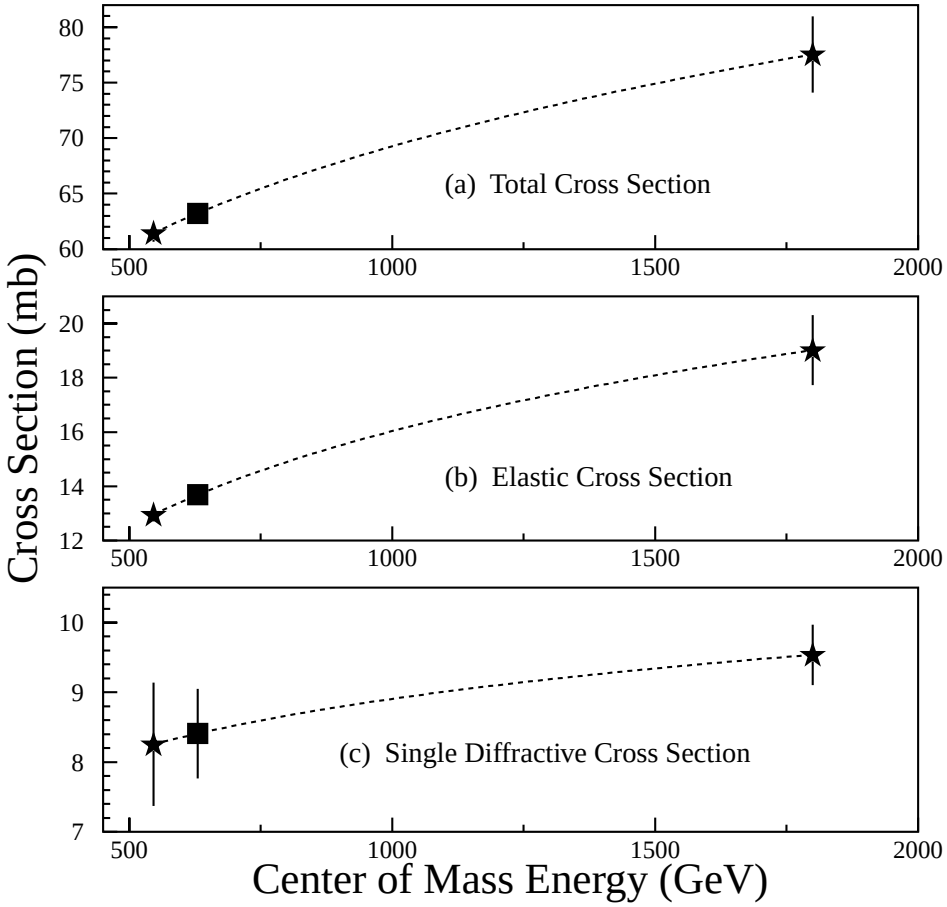

Figure 4.3. The three fits to the world average $p\overline{p}$ cross sections. The stars depict the WA cross sections at $\sqrt{s}$ =546 and 1800 GeV.

down the beam pipe. At high luminosities two or more single diffractive events may occur simultaneously in opposite directions with a calculable probability. This is measured as a double diffractive event and produces a higher acceptance and is corrected by the factor f_{MSD}, see Table 4.2.

4.2.3 Beam Halo Correction (f_{halo})

Beam halo is comprised of particles that have a trajectory within the Tevatron far from the nominal bunch center. When the proton and antiproton are focused at the center of the detector halo beam particles can be deflected outside the

beam pipe and into the detector. Halo events are rejected at the trigger level and affect the luminosity measurement. Beam halo effects depend on beam characteristics and luminosity and therefore vary from run to run. The effect is very slight as can been seen from the combined MSD and halo corrections listed in table 4.2.

4.2.4 Luminosity Summary

The total integrated luminosity for this analysis is 109 pb^{-1} which is the sum of the luminosities for Run Ib (95 pb^{-1}) and RunIa (14 pb^{-1}). Uncertainties in this luminosity calculation are listed in Table 4.3. Additional uncertainties in the luminosity are luminosity matching between the Jet_{50} and Jet_{85} triggers and luminosity matching between RunIa and RunIb also listed in Table 4.3. All luminosity uncertainties were taken care of within the limit calculation to be discussed in Chapter 6.

4.3 Data Selection

4.3.1 Determining the Vertex of an Event

Once a hard scattering has occurred and the appropriate trigger has recorded an event, it is very important that you have a good measurement of the interaction vertex. The vertex is the point at which the interaction occurs.

The interaction vertex is determined by the tracking chambers. The x–y position of the vertex is calculated with tracks reconstructed by the vertex chamber (VTX) in the r–ϕ plane. The vertex position in the x–y plane is an average over all events for that run because the beam position remains very stable throughout a run.

On the other hand, the z coordinate of the vertex has an approximately Gaussian distribution centered around $z \approx$ -10 cm with an rms of $\approx$ 30 cm. The

Sources of Uncertainty in Luminosity Calculation

Source of Uncertainty	Uncertainty %
World Average $p\overline{p}$ Cross Sections	2.37
Hardware Efficiency	1.7
Geometric Acceptance	2.73
Time Dependencies	0.70
Total	5.81
Trigger Matching between Jet_{30} and Jet_{50}	4.9
Run Matching between RunIa and RunIb	0.08

Table 4.3. Uncertainties in the luminosity calculation. Trigger matching and run matching uncertainties are applied separately.

z position is obtained from extrapolating CDC or FDC tracks, reconstructed in the r–z plane, out until they intersect the z axis. The z vertex resolution varies from 0.65–0.95 cm. For multiple interaction events, the two vertices are resolved if the clusters of tracks are separated by more than 7 cm on the z axis [38].

At high instantaneous luminosity more than one interaction per beam crossing can occur. The event reconstruction retains at most two vertices. The parameter

$$H_T = |\sum_{jets} \overrightarrow{E_T}^{jet}| \tag{4.10}$$

was calculated for both vertices. The vertex with the minimum H_T is selected as the event vertex. The vertex is also required to be within 50 cm of the detector center [32]. These cuts and procedures are reflected in the vertex efficiencies described in Section 4.3.6.

There is a possibility the H_T vertex selection criteria is biased in events where the first two leading jets have the same absolute rapidity. In this case the minimized H_T parameter may describe the wrong vertex. See Reference [32] for the detailed study on this bias.

4.3.2 Event Quality Selections

Quality selections are made to ensure the event has two well-reconstructed calorimeter jets and to reject non-dijet background. The quality selections used for this analysis are the standard jet quality selections for Run I [39].

These selections are applied in the order listed below.

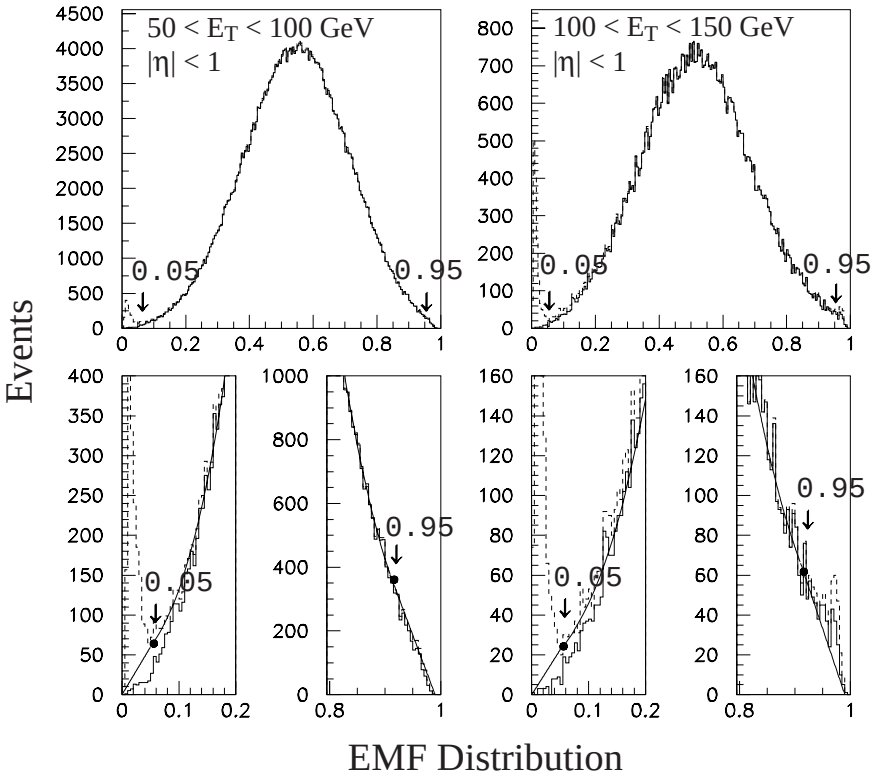

Figure 4.4. The measured EMF distributions for different E_T ranges. The lower plots show the cut values and the fit used to calculate the efficiency of the cut. The dashed histogram shows the full data sample and the solid histogram shows a data sample with minimal noise contamination. The arrows indicate the cut values. The peaks at EMF 0 or 1 are due to contamination.

Standard Quality selections

- $0.05 \leq \text{EMF} \leq 0.95$

  The electromagnetic fraction of a jet (EMF) is the fraction of a jet's transverse energy deposited in the electromagnetic modules of the calorimeter. EMF is sensitive to large depositions of fake energy by a noisy cell located within the electromagnetic or hadronic layers of the calorimeter. A selection at the high end of the EMF distribution reduces fakes from a noisy cell in the electromagnetic modules and removes jets from electromagnetic object (e, γ), while a selection at the low end of the distribution reduces noise from the hadronic region of the calorimeter, see figure 4.4.

- $\text{CHF} < 0.4$

  The coarse hadronic fraction (CHF) is the fraction of a jet's transverse energy deposited in the coarse hadronic layers of the calorimeter. This selection is used to remove jet-like objects resulting from main ring losses into the calorimeter, since the main ring enters the coarse hadronic region of the calorimeter.

- $\text{HCF} < 10$

  The hot cell fraction selection (HCF) is the ratio of the transverse energy of the most energetic cell in a jet to that of the second most energetic cell. A good jet has its energy distributed over many calorimeter cells due to longitudinal as well as lateral shower development in the calorimeter. High values of HCF indicate a fake due to a single noisy cell (hot cell) see figure 4.5a.

- $\frac{\not\!\!E_T}{E_T} < 0.7$

  The missing transverse energy fraction of the event is the total amount of missing transverse energy in an event divided by the transverse energy

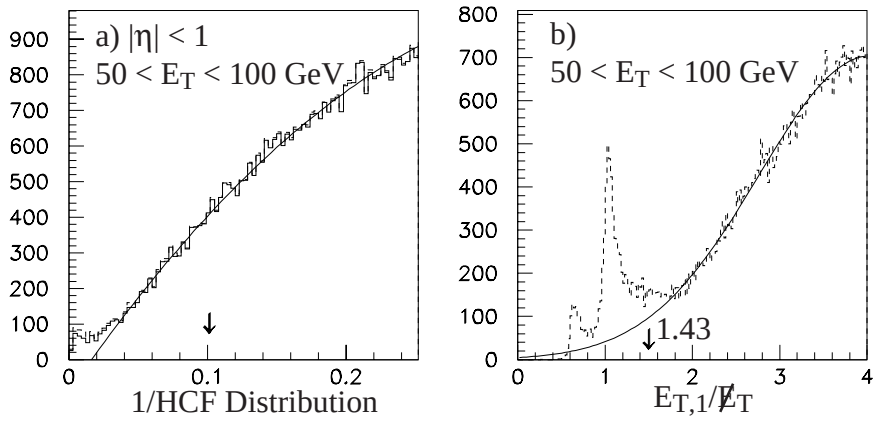

Figure 4.5. (a) The 1/HCF distribution. The arrow shows the location of the cut for $\sqrt{s} = 1800$ GeV. (b) The distribution of $\frac{E_T^{jet1}}{\not\!\!E_T}$. The arrow at $\frac{E_T^{jet1}}{\not\!\!E_T} = 1.43$ corresponds to the $\frac{\not\!\!E_T}{E_T^{jet1}}$ cut of 0.7. The peak at 1.0 is due to contamination from cosmic rays and the main ring. The dashed histograms show the distributions for the full data samples. The curve is a fit to the histogram.

of the leading jet. This cut gets rid of events where large amounts of jet energy are lost through cracks in the calorimeter. See 4.5b for a plot of this distribution and see 4.6b for the efficiency of this cut.

- $E_T > 15$

  Jets are required to have more than 15 GeV in E_T.

- $|z_{vertex}| < 50$ cm

  The z vertex selection is used to ensure the event is well contained in the fiducial region of the detector.

The efficiencies for these selections range from 97.25 % at 100 GeV to around 96 % at 400 GeV [23], see Figure 4.6.

4.3.3 Dijet Mass Calculation and Additional η Selections

Assuming that the individual jets are massless, the dijet mass is given by:

$$M_{jj}^2 = 2 \cdot E_{T_1} \cdot E_{T_2} \cdot (\cosh(\Delta\eta) - \cos(\Delta\phi)) \tag{4.11}$$

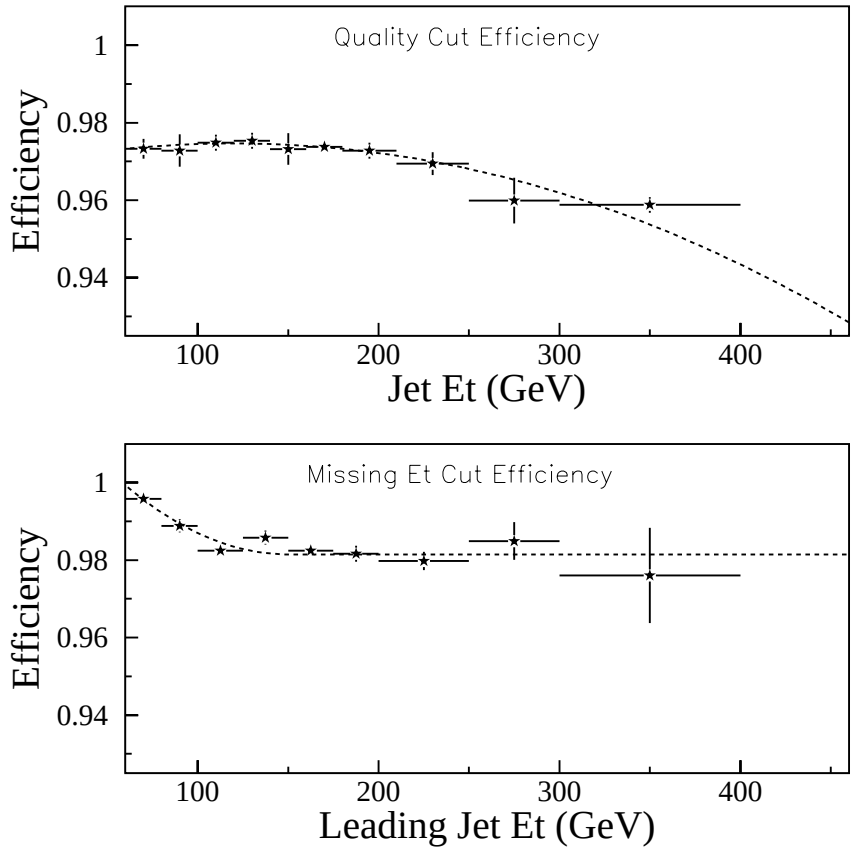

Figure 4.6. Top: The efficiency of the standard jet quality cuts for $|\eta| < 0.5$ at $\sqrt{s}$= 1800 GeV. Bottom: The efficiency of the $\not\!\!E_T$ used in the inclusive jet analysis at $\sqrt{s}$ = 1800 GeV. The dotted curves show the fits to the measured efficiencies.

where E_{T_1} and E_{T_2} are the transverse energies of the two jets with the highest E_T.

The following selections are made to restrict the two leading jets to a region of the detector where jet energies are well measured and the triggers are fully efficient.

$$|\eta_{1,2}| < 1.0 \qquad (4.12)$$
$$\Delta\eta = |\eta_1 - \eta_2| < 1.6$$

The $|\eta| < 1.0$ selection is applied to the two leading jets to contain the jets in a region where the jet energy scale is well understood and to maximize the signal to noise (heavy objects will decay more centrally than QCD dijet production). The selection on $\Delta\eta = |\eta_1 - \eta_2|$ is used to improve signal/background; QCD production has a large t-channel component which means it is peaked toward the beam direction with a large $\Delta\eta$, while the signal events are s-channel and tend to have a flatter, more centralized production. The dijet angular distribution gives the characteristic angular distribution of Rutherford scattering: $\frac{dN}{d\cos\theta^*} \propto (1 - \cos\theta^*)^{-2}$. The pole at $\cos\theta^* = 1$ causes problems so the χ variable is introduced into the dijet angular distribution in which $\chi = e^{2|\eta^*|}$, where $\eta^* = \frac{1}{2}(\Delta\eta)$. $\Delta\eta < 1.6$ corresponds to $\chi < 5$. The measured dijet angular distributions [14] show an increased rate above $\chi = 5$ in figure 4.7, which makes $\Delta\eta < 1.6$ ($\chi < 5$) a good cut to clean up the QCD background in this region. The s-channel signal events are expected to have a flatter distribution in χ because $\frac{dN}{d\cos\theta^*} \propto (1 + \cos\theta^*)^2$ for these events.

4.3.4 Trigger Efficiencies

A dijet mass range where each of the Level 2 jet triggers is efficient is determined by calculating the ratio of dijet mass events passing a more restrictive trigger to those from a less restrictive trigger. This ratio should approach one if the more restrictive trigger is a complete subset of the less restrictive trigger and both triggers are fully efficient. For example, the unprescaled trigger, Jet_{85}, is a complete subset of the unprescaled trigger, Jet_{115}, as shown in Figure 4.8. If this ratio does not approach one then the ratio will approach some constant

determined by the relative prescales of the two triggers. The point at which the ratio becomes constant is the point where the more restrictive trigger is unbiased by the less restrictive trigger and is known as the mass turn-on [32]. Table 4.4 shows the dijet mass selections for each trigger. Figures 4.8 and 4.9 show the mass turn-ons and the subsequent efficiencies for this analysis.

4.3.5 Event Weighting

Each event is weighted by ω, where ω is defined as:

$$\omega = \frac{1}{\epsilon_{Jet_1}\epsilon_{Jet_2}\epsilon_{trigger}}, \tag{4.13}$$

where $\epsilon_{trigger}$ is the trigger efficiency and ϵ_{Jet_1} and ϵ_{Jet_2} are the jet efficiencies.

4.3.6 Vertex Efficiencies

The vertex efficiencies reflect the effect of the cut on the vertex position, $z_{vertex} < 50$cm. The small differences in ϵ_{vertex} are due to the different filter prescales used to collect the data. These prescales mean that the data sets were obtained over different periods during which the collision points moved which changed the vertex distributions. Table 4.5 lists these efficiencies.

4.4 Dijet Data Set

The data sample used in this analysis was collected during 1992–93 (Run Ia) and 1994–95 (Run Ib) and corresponds to an integrated luminosity of 109 pb^{-1} . During Run Ib, data was collected using four triggers with E_T thresholds of 30, 50, 85 and 115 GeV. The Run Ia data was collected with an E_T threshold of 115. Tables 4.6 and 4.7 list the data for RunIb and RunIa used in this analysis. Figure 4.10 shows the fully corrected dijet mass spectrum used in this analysis.

4.5 Summary

In this chapter the selection of data was discussed. At this point the data has been selected and corrected by the jet energy scale and efficiencies and can be compared to the signal and background predictions once these predictions are smeared by detector resolution, which will be discussed in the next chapter.

Trigger Thresholds

Trigger	M_{JJ} Turn-on (GeV/c^2)		Number of
	$\Delta\eta cut$	w/o $\Delta\eta cut$	Events
Jet_30	180	200	2840
Jet_50	250	270	6655
Jet_85	320	350	24330
Jet_115	470	550	4064
Jet_115(Ia)	470	NA	1184

Table 4.4. Run Ib triggers Jet_{30}, Jet_{50}, Jet_{85} and Jet_{115} and Run Ia trigger for Jet_{115}. The Run Ia trigger M_{jj} selection was chosen to match the Run Ib M_{jj} selection.

Table 4.5. Efficiency of the vertex selection. The errors are statistical.

Trigger	ϵ_{vertex} (%)
Jet_{115}	91.32 ± 0.73
Jet_{85}	91.02 ± 0.21
Jet_{50}	90.17 ± 0.41
Jet_{30}	90.06 ± 0.68

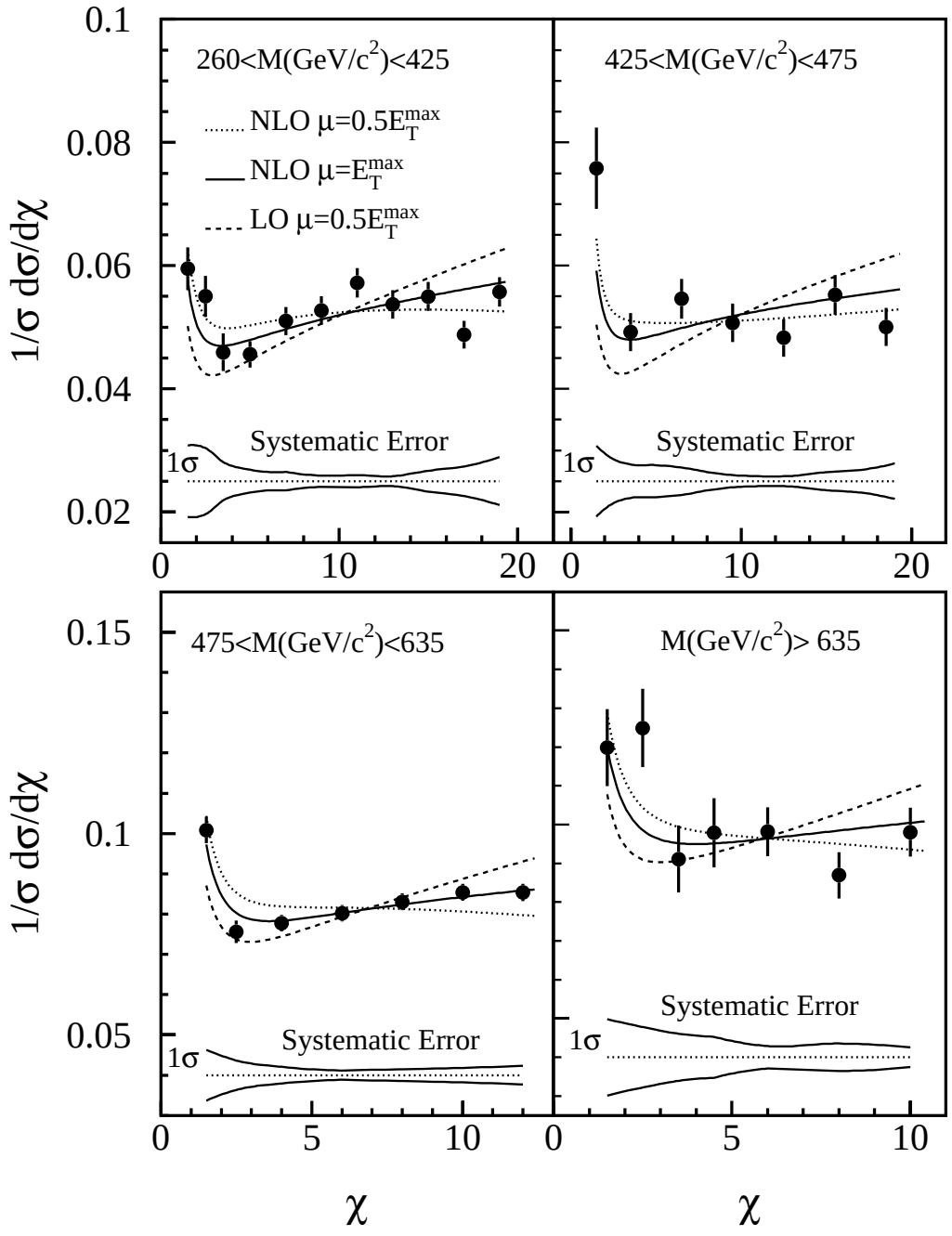

Figure 4.7. Measured dijet angular distributions at various dijet masses.

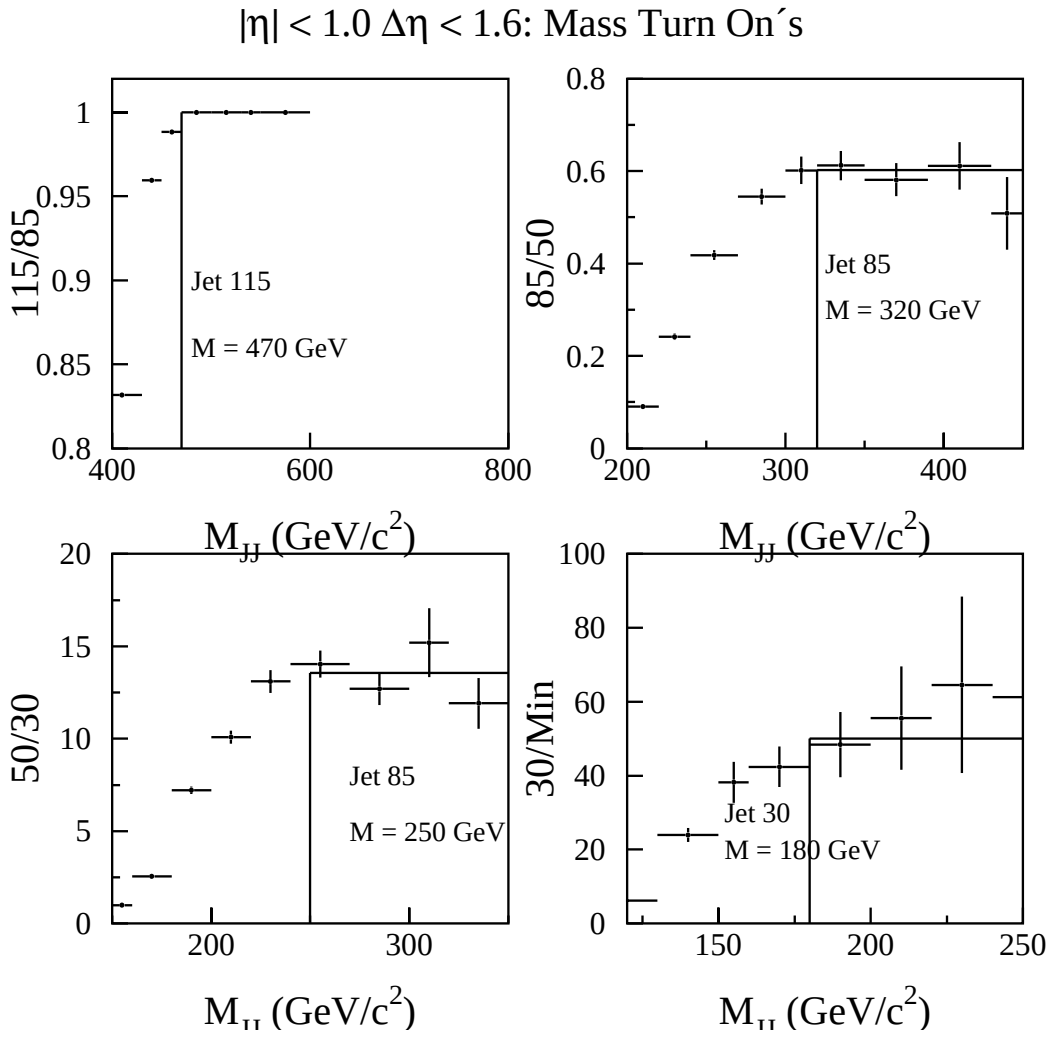

Figure 4.8. Ratios of the number of dijet events passing a more restrictive jet energy trigger to that of a less restrictive trigger versus dijet invariant mass. The line shows the point where the ratio is statistically consistent with being constant indicating that the more restrictive trigger is unbiased by the less restrictive trigger beyond this point. This point is known as the mass turn-on.

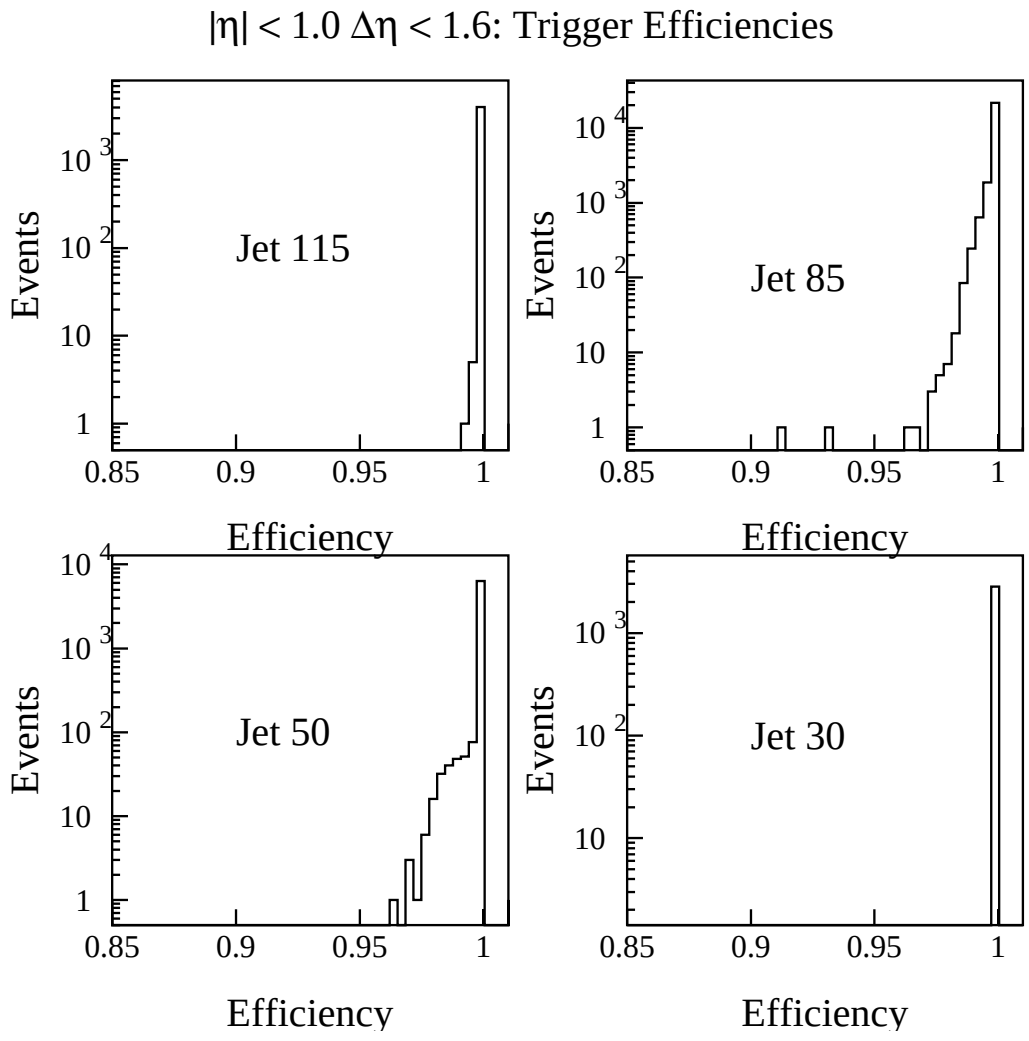

Figure 4.9. The efficiencies after making the dijet mass selections

Table 4.6: Data used in this analysis from Run Ib

M_{min} (GeV/c^2)	M_{max} (GeV/c^2)	Number of Events	ω	$\epsilon_{vert}(\%)$ $\pm$	$\mathcal{L}(pb^{-1})$	Corrected Events
180.	190.	778.	1.06	90.06±0.07	0.36	274502.
190.	200.	625.	1.06	90.06±0.07	0.36	220843.
200.	210.	464.	1.06	90.06±0.07	0.36	164218.
210.	220.	370.	1.07	90.06±0.07	0.36	131140.
220.	230.	251.	1.07	90.06±0.07	0.36	89125.
230.	240.	199.	1.07	90.06±0.07	0.36	70782.
240.	250.	153.	1.07	90.06±0.07	0.36	54478.
250.	260.	1710.	1.07	90.17±0.04	4.84	45822.
260.	270.	1314.	1.08	90.17±0.04	4.84	35264.
270.	280.	1101.	1.08	90.17±0.04	4.84	29016.
280.	290.	855.	1.08	90.17±0.04	4.84	22561.
290.	300.	672.	1.08	90.17±0.04	4.84	17743.
300.	310.	559.	1.08	90.17±0.04	4.84	14771.
310.	320.	444.	1.08	90.17±0.04	4.84	11748.
320.	330.	4291.	1.08	91.02±0.02	56.48	9671.
330.	340.	3525.	1.08	91.02±0.02	56.48	7945.
340.	350.	2940.	1.08	91.02±0.02	56.48	6631.
350.	360.	2501.	1.09	91.02±0.02	56.48	5643.
360.	370.	2113.	1.09	91.02±0.02	56.48	4768.
370.	380.	1775.	1.09	91.02±0.02	56.48	3857.
380.	390.	1456.	1.09	91.02±0.02	56.48	3164.
390.	400.	1244.	1.09	91.02±0.02	56.48	2704.
400.	410.	992.	1.09	91.02±0.02	56.48	2157.
410.	420.	859.	1.09	91.02±0.02	56.48	1869.
420.	430.	738.	1.09	91.02±0.02	56.48	1606.
430.	440.	605.	1.09	91.02±0.02	56.48	1316.
440.	450.	508.	1.09	91.02±0.02	56.48	1106.
450.	460.	446.	1.09	91.02±0.02	56.48	971.
460.	470.	337.	1.09	91.02±0.02	56.48	734.
470.	480.	593.	1.09	91.32±0.07	94.87	768.
480.	490.	492.	1.09	91.32±0.07	94.87	637.
490.	500.	402.	1.09	91.32±0.07	94.87	520.
500.	510.	381.	1.09	91.32±0.07	94.87	523.
510.	520.	282.	1.09	91.32±0.07	94.87	387.
520.	530.	251.	1.09	91.32±0.07	94.87	345.
530.	540.	234.	1.09	91.32±0.07	94.87	321.
540.	550.	203.	1.09	91.32±0.07	94.87	279.

Table 4.6: continued

M_{min} (GeV/c^2)	M_{max} (GeV/c^2)	Number of Events	ω	$\epsilon_{vert}(\%)$ $\pm$	$\mathcal{L}$ (pb^{-1})	Corrected Events
550.	560.	146.	1.09	91.32±0.07	94.87	201.
560.	570.	142.	1.09	91.32±0.07	94.87	195.
570.	580.	126.	1.09	91.32±0.07	94.87	173.
580.	590.	101.	1.09	91.32±0.07	94.87	139.
590.	600.	82.	1.09	91.32±0.07	94.87	113.
600.	610.	90.	1.10	91.32±0.07	94.87	124.
610.	620.	73.	1.09	91.32±0.07	94.87	100.
620.	630.	43.	1.09	91.32±0.07	94.87	59.
630.	640.	62.	1.09	91.32±0.07	94.87	85.
640.	650.	55.	1.09	91.32±0.07	94.87	76.
650.	660.	44.	1.09	91.32±0.07	94.87	61.
660.	670.	31.	1.10	91.32±0.07	94.87	43.
670.	680.	23.	1.09	91.32±0.07	94.87	32.
680.	690.	33.	1.09	91.32±0.07	94.87	45.
690.	700.	18.	1.10	91.32±0.07	94.87	25.
700.	710.	32.	1.10	91.32±0.07	94.87	44.
710.	720.	20.	1.09	91.32±0.07	94.87	27.
720.	730.	13.	1.09	91.32±0.07	94.87	18.
730.	740.	12.	1.09	91.32±0.07	94.87	16.
740.	750.	9.	1.10	91.32±0.07	94.87	12.
750.	760.	16.	1.09	91.32±0.07	94.87	22.
760.	770.	6.	1.09	91.32±0.07	94.87	8.
770.	780.	2.	1.09	91.32±0.07	94.87	3.
780.	790.	8.	1.10	91.32±0.07	94.87	11.
790.	800.	2.	1.09	91.32±0.07	94.87	3.
800.	810.	7.	1.11	91.32±0.07	94.87	10.
810.	820.	2.	1.09	91.32±0.07	94.87	3.
820.	830.	5.	1.09	91.32±0.07	94.87	7.
830.	840.	2.	1.09	91.32±0.07	94.87	3.
840.	850.	3.	1.09	91.32±0.07	94.87	4.
850.	1400.	18.	1.09	91.32±0.07	94.87	23.

M_{min} (GeV/c^2)	M_{max} (GeV/c^2)	Number of Events	ω	ϵ_{vert} $\pm$	$\mathcal{L}$ (pb^{-1})	Corrected Events
470.	480.	94.	1.09	87.78 $\pm$0.07	14.15	953.
480.	490.	72.	1.09	87.78 $\pm$0.07	14.15	730.
490.	500.	48.	1.09	87.78 $\pm$0.07	14.15	488.
500.	510.	45.	1.09	87.78 $\pm$0.07	14.15	431.
510.	520.	42.	1.09	87.78 $\pm$0.07	14.15	402.
520.	530.	35.	1.09	87.78 $\pm$0.07	14.15	334.
530.	540.	34.	1.09	87.78 $\pm$0.07	14.15	325.
540.	550.	26.	1.09	87.78 $\pm$0.07	14.15	248.
550.	560.	38.	1.09	87.78 $\pm$0.07	14.15	365.
560.	570.	21.	1.09	87.78 $\pm$0.07	14.15	202.
570.	580.	20.	1.09	87.78 $\pm$0.07	14.15	192.
580.	590.	12.	1.09	87.78 $\pm$0.07	14.15	115.
590.	600.	18.	1.09	87.78 $\pm$0.07	14.15	172.
600.	610.	14.	1.09	87.78 $\pm$0.07	14.15	134.
610.	620.	11.	1.09	87.78 $\pm$0.07	14.15	105.
620.	630.	8.	1.10	87.78 $\pm$0.07	14.15	78.
630.	640.	10.	1.10	87.78 $\pm$0.07	14.15	96.
640.	650.	5.	1.12	87.78 $\pm$0.07	14.15	49.
650.	660.	3.	1.09	87.78 $\pm$0.07	14.15	29.
660.	670.	4.	1.09	87.78 $\pm$0.07	14.15	38.
670.	680.	4.	1.10	87.78 $\pm$0.07	14.15	39.
680.	690.	7.	1.09	87.78 $\pm$0.07	14.15	67.
690.	700.	2.	1.12	87.78 $\pm$0.07	14.15	20.
700.	710.	1.	1.20	87.78 $\pm$0.07	14.15	11.
710.	720.	5.	1.10	87.78 $\pm$0.07	14.15	48.
720.	730.	2.	1.09	87.78 $\pm$0.07	14.15	19.
730.	740.	0.	1.00	87.78 $\pm$0.07	14.15	0.
740.	750.	1.	1.09	87.78 $\pm$0.07	14.15	10.
750.	760.	1.	1.09	87.78 $\pm$0.07	14.15	10.
760.	770.	0.	1.00	87.78 $\pm$0.07	14.15	0.
770.	780.	0.	1.00	87.78 $\pm$0.07	14.15	0.
780.	790.	1.	1.09	87.78 $\pm$0.07	14.15	10.
790.	800.	2.	1.09	87.78 $\pm$0.07	14.15	19.
800.	810.	1.	1.09	87.78 $\pm$0.07	14.15	10.
810.	820.	1.	1.09	87.78 $\pm$0.07	14.15	10.
820.	830.	1.	1.09	87.78 $\pm$0.07	14.15	10.
830.	840.	0.	1.00	87.78 $\pm$0.07	14.15	0.
840.	850.	0.	1.00	87.78 $\pm$0.07	14.15	0.
850.	1400.	3.	1.00	87.78 $\pm$0.07	14.15	29.

Table 4.7. Data used in this analysis from Run Ia.

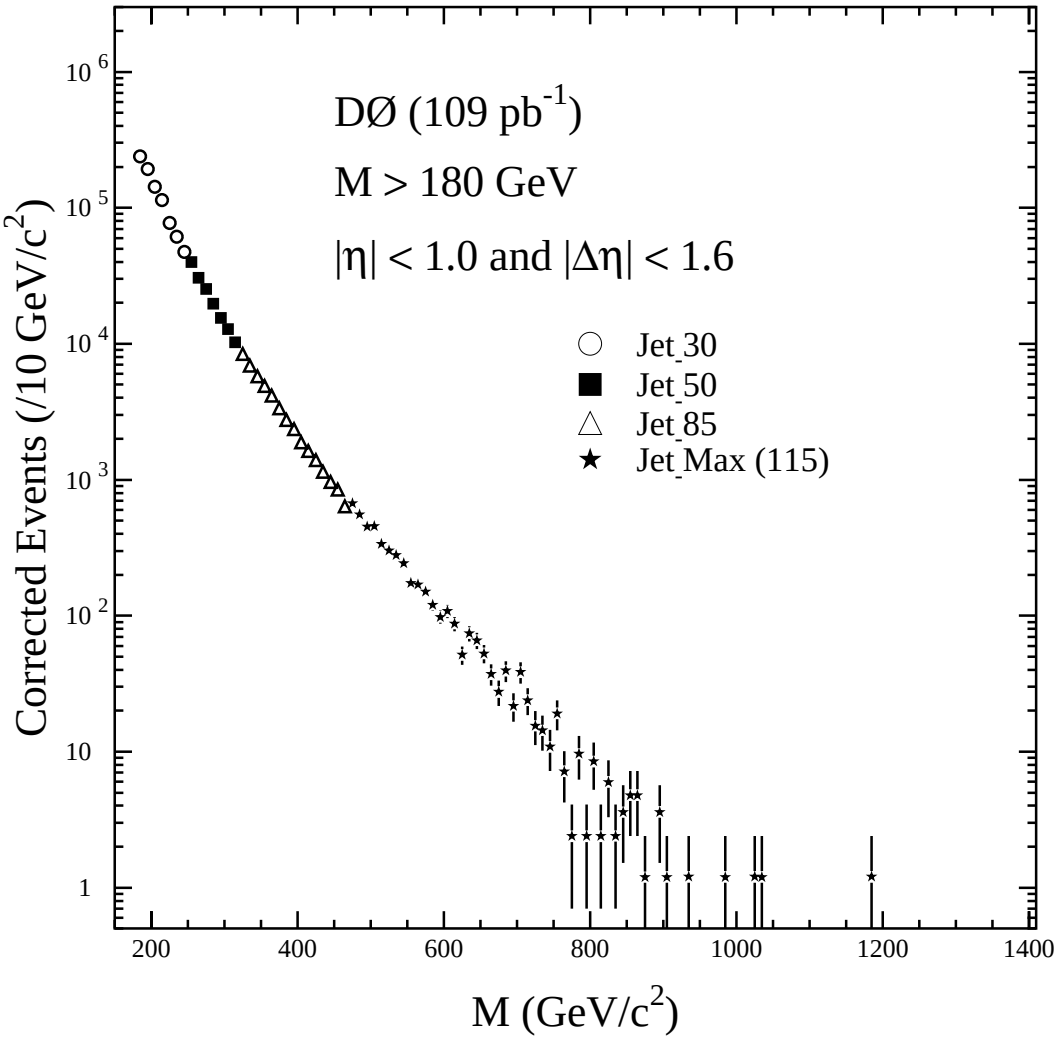

Figure 4.10. The dijet mass spectrum for Run1a and Run1b

CHAPTER 5

SIGNAL AND DATA MODELING

5.1 Simulation of Signal

Three different models are considered as possible signals in the dijet mass spectrum. These models are chosen to correspond to three different types of resonance decays. The first model is the decay of an excited quark to a quark and a gluon ($q^* \to qg$). The second and third models are additional W and Z bosons with similar properties to their Standard Model counterparts ($W' \to q\overline{q}'$, $Z' \to q\overline{q}$). These models are described in more detail in Chapter 1.

The q^*, W' and Z' models are simulated using the PYTHIA [40] Monte Carlo with the CTEQ6 [41–42] parton distribution function (PDF). For each model, the particle masses are generated in 25 GeV intervals from 200 GeV to 1 TeV. For each mass interval 50,000 events are generated. Each jet is smeared with the single jet resolutions [43] to be discussed in Section 5.3.1. The subsequent q^*, W' and Z' invariant mass distributions (line shapes) are plotted in Figure 5.1.

5.1.1 Excited Quark Simulation ($q^* \to qg$)

The excited quark model used in this analysis is described in Reference [15], and we use the following model parameters:

$$f = f_s = f' = 1.0,$$

$$\Lambda^* = M_{q^*}.$$

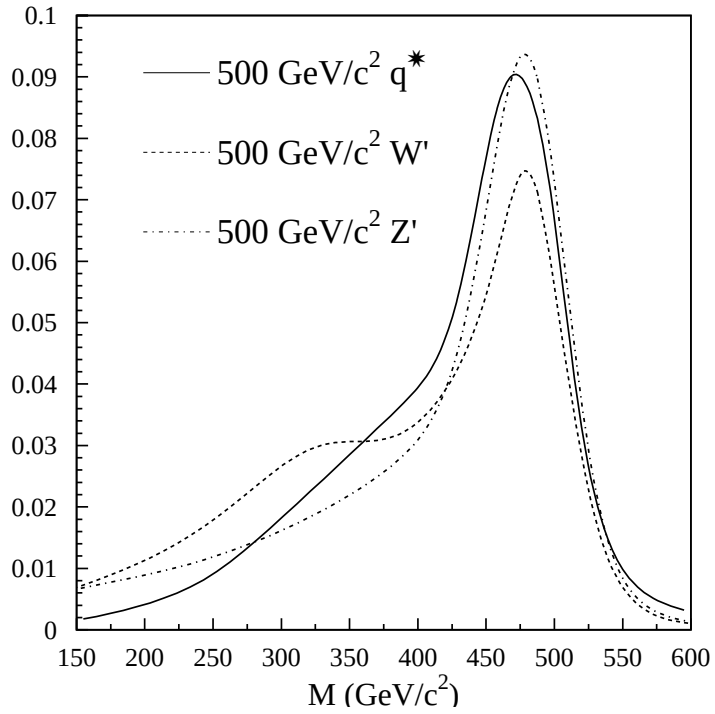

Figure 5.1. The resolution smeared line shapes for a 500 GeV q^*, $Z'$and W'signal. The line shapes have been smoothed and normalized to unit area.

The production cross section for the q^* model has been determined at leading order using the PYTHIA generator with the CTEQ6 PDF's [42].

5.1.2 W' and Z' Simulation

The W' and Z' are allowed to decay via the kinematically accessible quark channels only. The W' and Z' production cross sections are calculated to leading order using the PYTHIA generator with the CTEQ6 PDF's [42]. Factors (known as K factors) [44] are used to estimate the NLO W' cross section from the LO cross section, see Table 5.1 for the K factors.

Table 5.1. The K-factors used for the W' search

Mass Range (GeV/c^2)	k-factor
300.	1.336
400.	1.381
500.	1.431
600.	1.483
700.	1.532
800.	1.568
900.	1.608

5.1.3 Calculation of Theoretical Signal predictions (σ × Branching Ratio × acceptance)

The theoretical σ × (BR) is taken directly from the Pythia Monte Carlo at the particle level. The acceptance (a) for each model is the percentage of generated events that pass the selections

$$\begin{aligned} |\eta| &< 1. \\ |\Delta\eta| &< 1.6. \end{aligned} \tag{5.1}$$

See Figure 5.2 and Table 5.2 for the signal acceptances for each model. See Table 5.3 for the production cross sections and $\sigma \times BR \times a$ for each model.

5.2 Background

The inclusive dijet events are simulated using JETRAD [45]. For this analysis the NLO calculations of the dijet mass spectrum used the CTEQ6M [41–42] parton distribution function (PDF) with a renormalization scale (μ) of $0.5 \times E_T$, where E_T is that of the highest E_T parton. The parton clustering algorithm clusters partons within $1.3\mathcal{R}$ of one another and within $\mathcal{R} = 0.7$ of their E_T weighted η,ϕ centroid [25](cone algorithm).

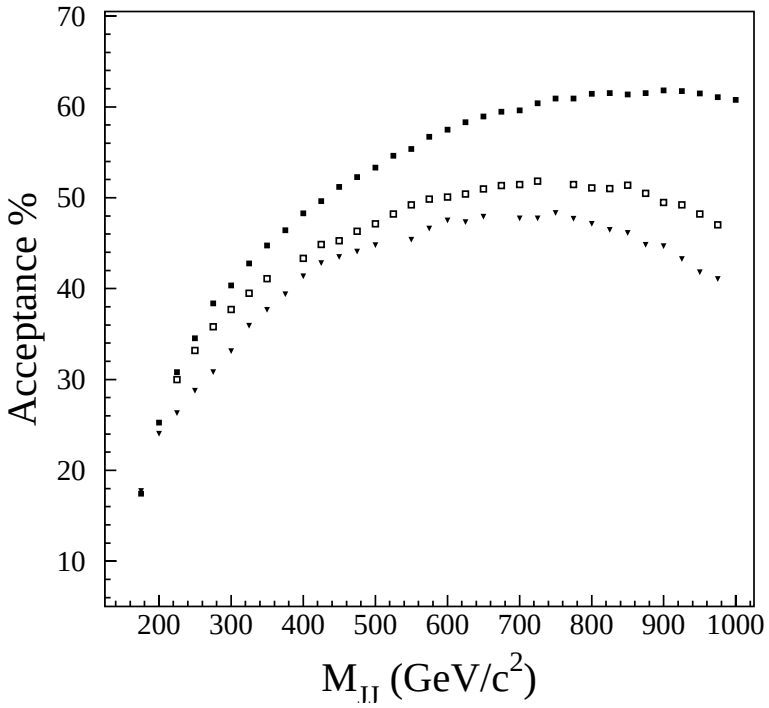

Figure 5.2. The acceptances for q^*(solid squares), Z'(open squares) and W'(triangles).

5.3 Resolution Smearing

The jet energy response or the ratio of true jet energy to energy measured in the calorimeter is limited by calorimeter noise, pile-up, out of cone showering and non-linearities in the calorimeter. The corrections made are average corrections per jet which are binned in terms of jet physical properties such as pseudo-rapidity and energy and are taken care of by the jet energy scale corrections discussed in Chapter 3. Additionally, the jet energy distributions are smeared by resolution effects which are predominantly energy dependent and can be separated from jet energy scale corrections.

The single jet resolution is applied directly to the signal Monte Carlo and is based on the single jet resolution parameters in Reference [32]. The background

Monte Carlo is smeared by a dijet mass resolution based on the single jet resolutions using a convolution method. In this analysis background Monte Carlo is smeared to match the data.

5.3.1 Single Jet Energy Resolution

The fractional single jet energy resolution $\frac{\sigma_E}{E}$ can be parameterized as follows:

$$\frac{\sigma_E}{E} = \sqrt{\frac{N^2}{E^2} + \frac{S^2}{E} + C^2}. \tag{5.2}$$

The nature of incident particles, sampling fluctuations and the intrinsic energy resolution contribute to the $\frac{S^2}{E}$ term. Detector non-linearities and electron/hadron response deviations from unity affect resolution at high energy and are represented mostly by C. Noise fluctuations affect the low energy range and are represented by the $\frac{N^2}{E^2}$ term [43].

During Run I the single jet resolutions were determined using the methods described in Reference [43]. The following is a summary of this study.

The energy resolution fraction should be uniform in the same uniform calorimeter sections. If different regions are used then there is some non-uniformity due to differences in the Central Calorimeter (CC), End Cap Calorimeter (EC) and the Inter-Cryostat region (ICR) sub-detectors. Therefore, the CC calorimeter with $|\eta| < 1$ is used to determine the jet resolutions. Instead of measuring $\frac{\sigma_E}{E}$ we will be using $\frac{\sigma_{E_T}}{E_T}$, where $E_T = \frac{E}{\cosh(\eta)}$. E_T will be used through out this analysis to take advantage of the conservation of energy in the plane transverse to the beam. In the case of $\frac{\sigma_{E_T}}{E_T}$ there will be a slight η dependence convoluted into the resolution determination since,

$$(\frac{\sigma_{E_T}}{E_T})^2 = (\frac{\sigma_E}{E})^2 + |sinh\eta|^2\sigma_\eta^2. \tag{5.3}$$

The effect on the resolution from η is very small in the central region but is more significant in larger η regions.

5.3.1.1 Dijet Balance Method

Data selection for this study is similar to the data selection used for the thesis analysis (see Chapter 4). The jet energies were corrected using CAFIX 5.1 [29].

The applied quality cuts [46–47] are

$$\begin{aligned} 0.05 \leq \text{EM Fraction} \leq 0.95 \\ \text{EM Fraction} \leq 0.95 \ (1.0 < |\eta_{detector}| < 1.5) \\ \text{CH Fraction} < 0.4 \\ \text{Cell ratio} < 20.0 \\ \frac{\not{E}_T}{E_T} < 0.7 \\ |z_{vertex}| < 50cm \end{aligned} \tag{5.4}$$

Energy conservation in the transverse energy plane is used in determining the single jet energy scale. Therefore, it is very important that effects due to low energy jets are eliminated as much as possible. A perfect event for this study would be two large E_T jets back-to-back, so for this study we require that the events are back-to-back to within 5 degrees and jets with reconstructed energies of less than 8 GeV are eliminated. The jets are required to be in the same $|\eta|$ region so that their resolutions are approximately the same.

An asymmetry variable, A, is defined:

$$A = \frac{E_{T,1} - E_{T,2}}{E_{T,1} + E_{T,2}}, \tag{5.5}$$

where $E_{T,1}$ and $E_{T,2}$ are the transverse energies of the two leading E_T jets. The variance of A can be written as

$$|\frac{\partial A}{\partial E_{T,2}}|^2 \sigma^2_{E_{T,2}} + |\frac{\partial A}{\partial E_{T,2}}|^2 \sigma^2_{E_{T,2}}. \tag{5.6}$$

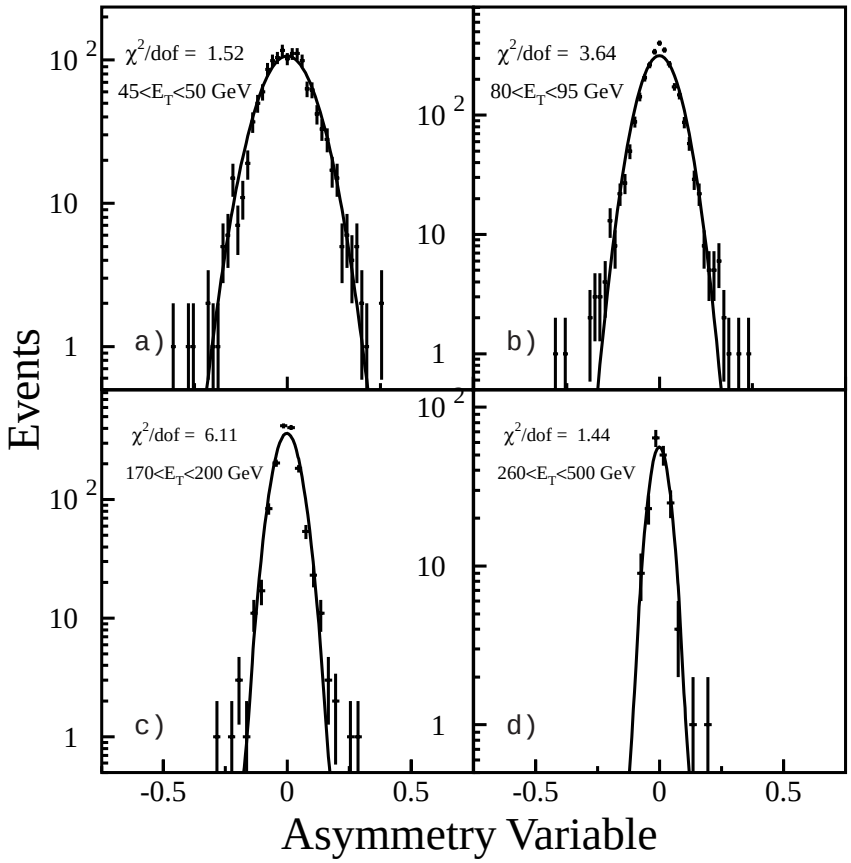

Figure 5.3. Asymmetry distribution in several E_T bins for jets with $|\eta| < 0.5$ and $E_T^{jet3} < 8$ GeV.

Assuming $E_T = E_{T,1} = E_{T,2}$ and $\sigma_{E_T} = \sigma_{E_{T,1}} = \sigma_{E_{T,2}}$, the resolution can be expressed as

$$\frac{\sigma_{E_T}}{E_T} = \sqrt{2}\sigma_A. \tag{5.7}$$

See Figure 5.3 for a plot of some asymmetry distributions. Additional, non-resolution effects are included within the single jet resolutions due to the effects of additional soft radiation, noise and underlying event fluctuations, detector effects, etc. Many of these effects need to be included for physics analyses but these soft radiation effects need to be removed for the particle-level dijet imbalance method.

Soft Radiation Correction

The ϕ and dijet cuts ($\Delta\phi < 5°$) and ($E_{T,3} < 8GeV$) attempt to reduce the number of jets to two. Unfortunately, jets remain that contain soft radiation and prevent the leading jets from balancing in E_T. This causes the measured resolutions to be overestimates. To correct for this effect resolutions were determined from samples with different third jet cuts: 8, 10, 12, 15 and 20 GeV, see Figure 5.4. If we plot the ratio between resolutions for third jet energy threshold x GeV and 8 GeV as follows,

$$(\frac{\sigma_{E_T}}{E_T})^{Thresh=xGeV}/(\frac{\sigma_{E_T}}{E_T})^{Thresh=8GeV} \tag{5.8}$$

we can parameterize each ratio with a suitable function and extrapolate the fit down to x=0, where x represents the cut on the third jet. We obtain the resolution from an ideal dijet sample without a cut on the third jet. Let the correction factor,

$$K(E_T) = (\frac{\sigma_{E_T}}{E_T})^{Thresh=0GeV}/(\frac{\sigma_{E_T}}{E_T})^{Thresh=8GeV}, \tag{5.9}$$

then the unbiased fractional resolution is as follows,

$$(\frac{\sigma_{E_T}}{E_T}) = K \times (\frac{\sigma_{E_T}}{E_T})^{Thresh=8GeV}. \tag{5.10}$$

This procedure is done for every E_T bin. The soft radiation bias should be larger for small values of E_T and negligible at high E_T, then $K(E_T)$ can be parameterized as follows,

$$K(E_T) = 1 - e^{-a_0 - a_1 E_T} \tag{5.11}$$

For a plot of this correction see Figure 5.5.

Dijet Imbalance Correction

After making the energy scale corrections to raw jet measurements we shoulde have particle jets. This is the energy inside the cone before interactions with the

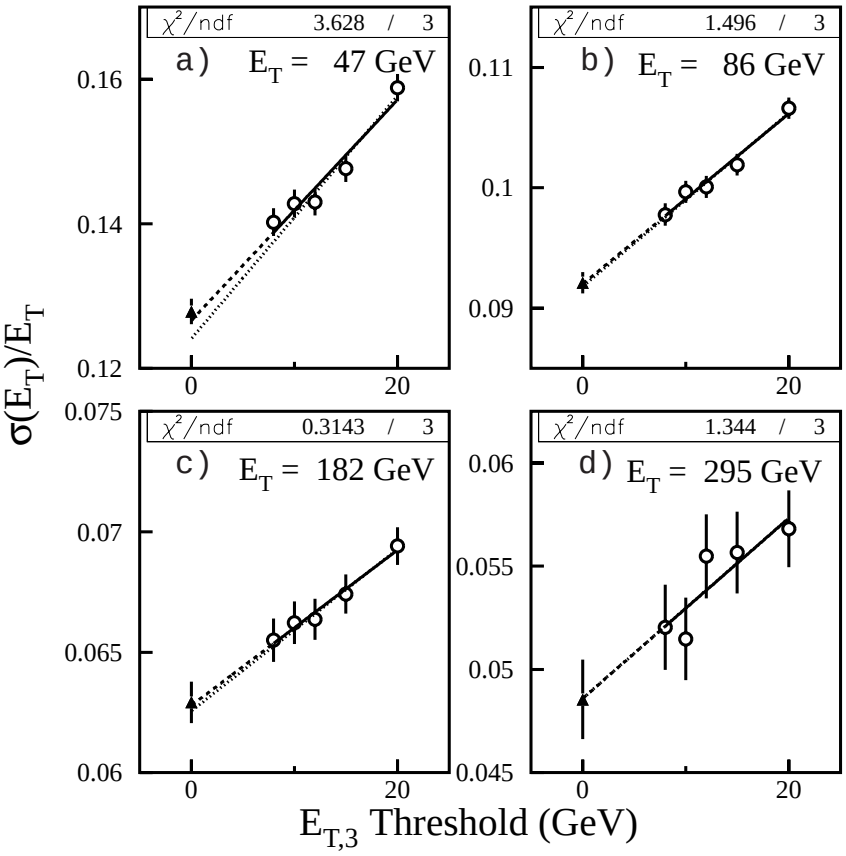

Figure 5.4. Resolutions as a function of the cut on E_T^{jet3} for different E_T bins ($|\eta| < 0.5$). The solid line shows the fit to the data points, the dashed line shows the extrapolation to $E_T^{jet3} = 0$, and the dotted line shows the fit excluding the $E_T^{jet3} < 8$ GeV point.

calorimeter. Energy carried by particles or partons outside the particle level cone does not belong to the particle jet. The total E_T of the particle jets should be zero in a dijet event. Two reconstructed jets do not necessarily balance because there could be particles emitted outside the cone.

The asymmetry method uses the principle of balancing the E_T of the two leading jets only, ie., no third jet. Then the dijet imbalance at the parton level is convoluted with the detector resolution and must be removed.

The particle imbalance contribution to the resolution $(\sigma_{E_T}|^{pjet})_{asym}$ is determined using the dijet imbalance method on particle jet Monte Carlo events,

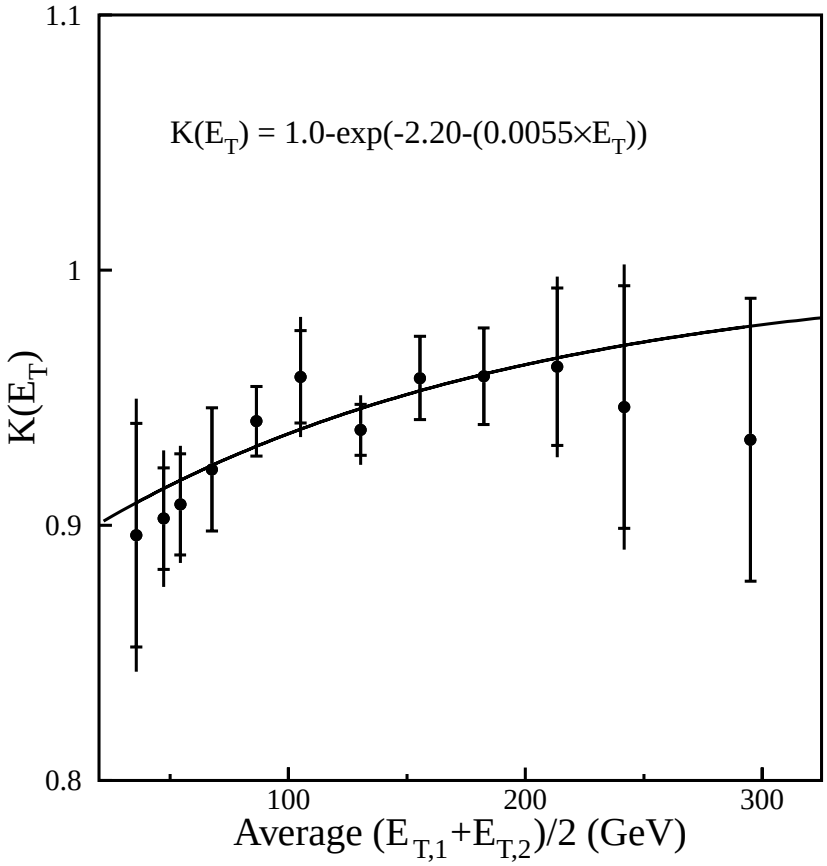

Figure 5.5. The soft radiation correction, K(E_T), as a function of E_T ($|\eta| < 0.5$). The error bars show the total uncertainty in the point-to-point correlations. The inner error bars show the uncertainty in the resolutions measured with $E_T^{jet3} >$ 8 GeV.

using HERWIG with different missing energy and $\Delta\phi$ conditions, see Figure 5.6 for results of this study.

After all of these corrections are applied, the single jet resolution is determined as shown in Figure 5.7. N, S and C fit parameters and their correlations are shown in Tables 5.4, 5.5, 5.6 and 5.7 for jets with $0.5 < |\eta| < 1.0$ and Tables 5.8, 5.9, 5.10 and 5.11 for jets with $|\eta| <$0.5.

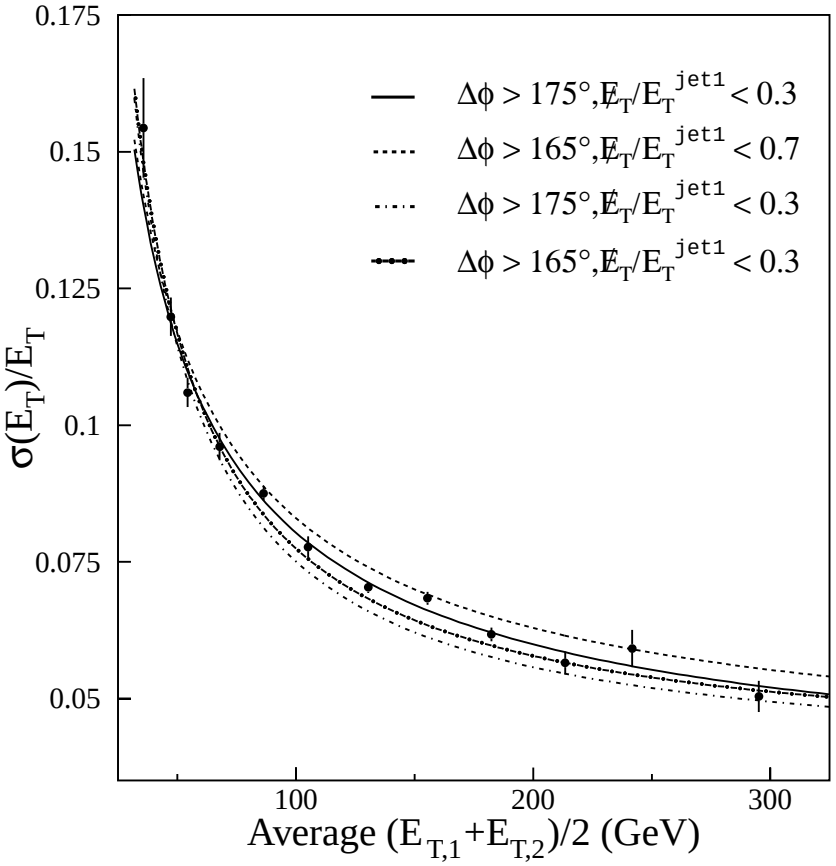

Figure 5.6. Fully corrected $\frac{\sigma_{E_T}}{E_T}$ as a function of the average E_T for $|\eta| < 0.5$ (i.e. the soft radiation correction and the particle-level dijet imbalance corrections have been applied). The data points (solid curve) show the resolution as calculated within the cuts $\frac{\not\!\!E_T}{E_T^{jet1}} < 0.7$ and the $\Delta\phi > 175°$. The dashed line shows the effect of using a cut of $\Delta\phi > 165°$. In addition, the effects of using a $\not\!\!E_T$ cut of $\frac{\not\!\!E_T}{E_T^{jet1}} < 0.3$ when $E_T^{jet1} > 100$ GeV, or $\not\!\!E_T < 30$ GeV when $E_T^{jet1} < 100$ GeV are shown (dash-dot and solid-dots lines).

5.3.1.2 Applying the Single Jet Resolutions to Signal Monte Carlo

The single jet resolutions are applied directly to signal Monte Carlo on a jet by jet basis. Uncertainties in the resolution are applied during the limit calculation. For each dijet mass bin a suite of 61 different line shapes are made. These line shapes are the signal Monte Carlo smeared at the nominal values, and at .1 σ interval values for the range of -3σ to $+3\sigma$ from the nominal values.

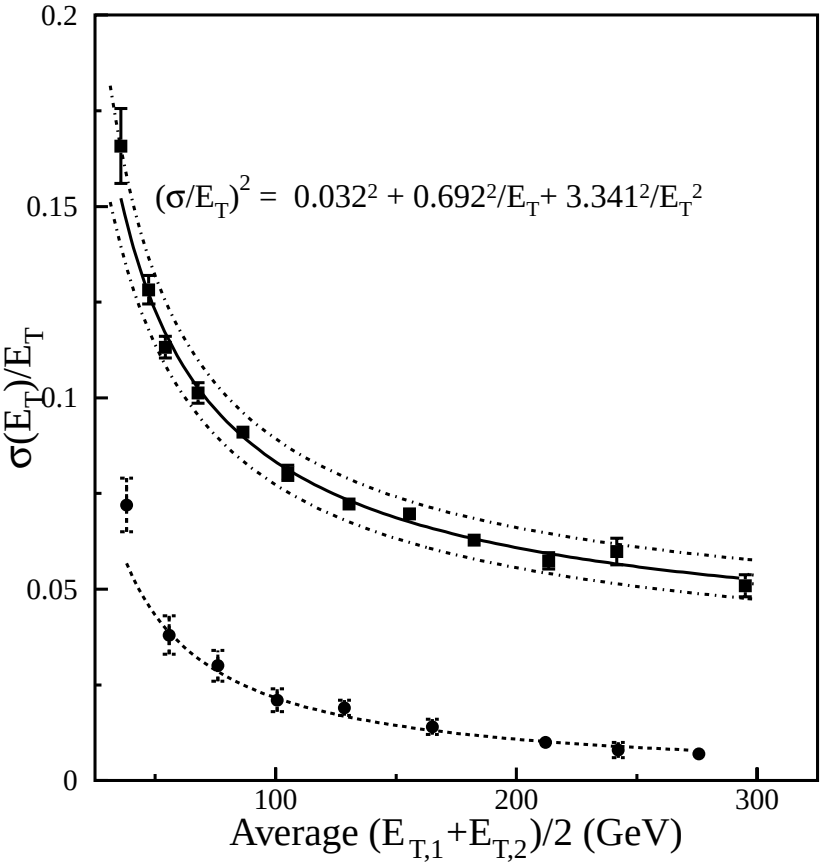

Figure 5.7. $\frac{\sigma_{E_T}}{E_T}$ as a function of average E_T for $|\eta| < 0.5$. The data points (squares) indicate the resolutions after the soft radiation correction and the solid curve shows the fit to the resolutions. The dash-dot lines show the systematic uncertainty due to the method. The dashed line is a fit to the particle-level resolutions obtained for MC points (circles).

During the limit calculation an n$\sigma(n = (-3, -2.9..., 2.9, 3))$ smearing is chosen randomly (with the appropriate Gaussian weights) for each iteration of the limit calculation.

5.3.2 Dijet Mass Resolution

In the DØ dijet mass analysis of Reference [32], the dijet data was unsmeared by the dijet mass resolutions; in other words, the data was corrected so one could compare it with the particle level Monte Carlo simulation. In this analysis we do something slightly different, the JETRAD [45] background simulation

is smeared by the resolution to model the data. In this method we need to obtain the dijet mass resolutions and then convolute with the Monte Carlo distributions. The convolution is done for a suite of 61 curves that represent the range of possible dijet mass smearings. These curves have the same purpose as the signal resolution curves, they will be applied during the limit calculation in a similar manner. Dijet mass resolutions are determined by smearing the jets in PYTHIA [40] Monte Carlo events using the single jet resolutions [43]. The smeared/unsmeared dijet mass ratio is plotted and fitted with a Gaussian distribution (see Figure 5.8). This is done for each mass point needed. The half widths obtained from these Gaussian fits are plotted. The parameterization of this plot is the dijet mass resolution [23][32]. These resolutions were recalculated for this analysis, see Figure 5.9.

The dijet mass resolutions are parameterized in terms of the dijet mass as follows:

$$\frac{\sigma(M)}{M} = \sqrt{A^2 + B^2 M + C^2 M^2 + D^2 M^3} \tag{5.12}$$

For parameters A, B, C and D obtained from the fit see Table 5.12.

5.3.2.1 The Convolution Method

Once, the dijet mass resolution is determined it is convoluted with the unsmeared Monte Carlo. Assume a trial M_{jj} spectrum, in this case a fit to the unsmeared Monte Carlo.

For example,

$$F(M') = A \cdot M'^{\alpha}(1 - \frac{M'}{\sqrt{S}})^{-\beta}. \tag{5.13}$$

This is just an example the one used in this analysis is a 6th order polynomial in dijet mass.

This will be convoluted with the measured mass resolutions:

$$f(M) = \int F(M')\sigma(M' - M, M')dM', \tag{5.14}$$

therefore, the number of events in a given mass bin is

$$F_i = \int f(M)dM. \tag{5.15}$$

The JETRAD Monte Carlo is then fitted using a binned maximum likelihood method using Minuit [48] to determine the values of A, α, and β. The smearing correction for each mass bin is given by

$$\int_{M_{min}}^{M_{max}} F(M)\, dM/F_i, \tag{5.16}$$

where

$$\int_{M_{min}}^{M_{max}} F(M)\, dM \tag{5.17}$$

is the original fitted unsmeared function. Finally, F_i is

$$F_i = \int_{M_{min}}^{M_{max}} \int_{-\infty}^{+\infty} F(M')\sigma(M' - M, M')\, dM'\, dM. \tag{5.18}$$

The dijet mass corrections are very small. See Figure 5.10 for dijet mass correction factors for various dijet mass resolution smearings. See Figure 5.11 for a plot of nominal resolution smearing of the dijet spectrum with excited quark signals superimposed.

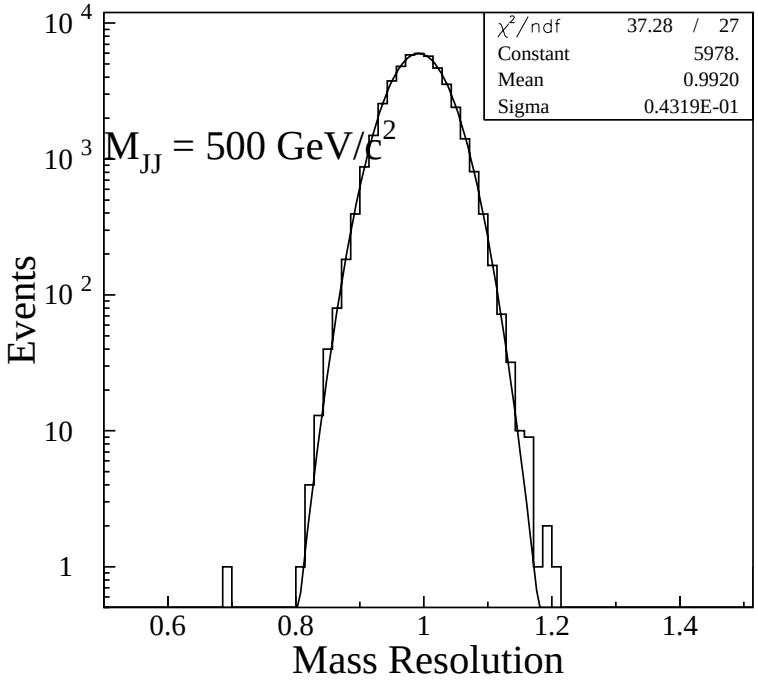

Figure 5.8. $\frac{M_{JJ}^{smeared}}{M_{JJ}^{unsmeared}}$ for the dijet mass of 500 GeV.

5.4 Summary

This chapter discussed the resolution smearing of the simulated background and signal and the agreement of data with the simulated data. The next chapter will discuss the confidence limit analysis.

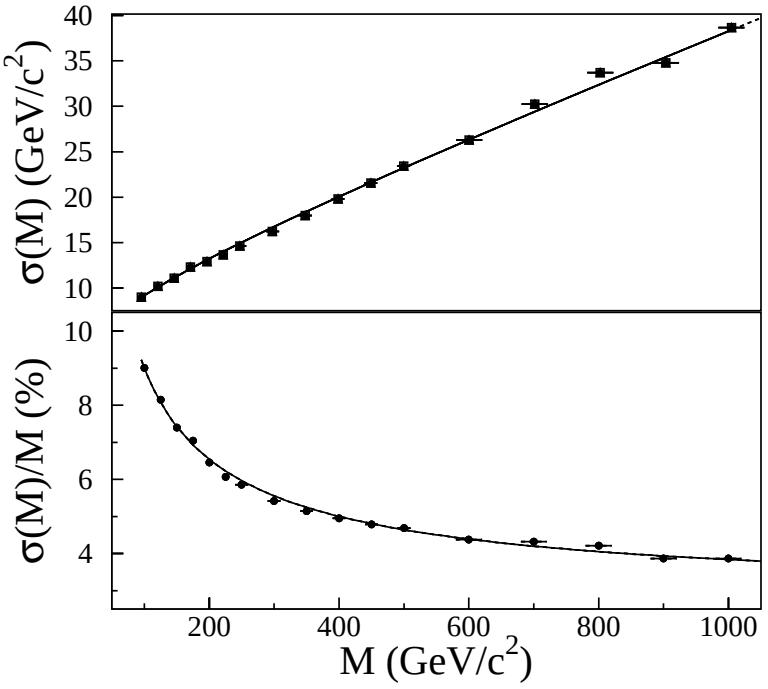

Figure 5.9. Top: $\sigma(M_{JJ})$ plotted per dijet mass for the nominal values. Bottom: $\frac{\sigma}{M_{JJ}}$ plotted per dijet mass for the nominal values. The data used is Monte Carlo.

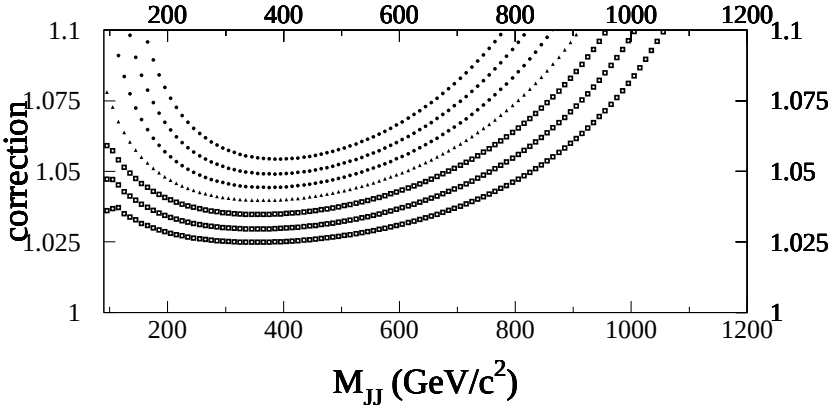

Figure 5.10. The dijet mass correction for the nominal value (middle line) and the $\pm 1, 2, 3$ σ values.

Mass (GeV/c^2)	q^* (%)	W' (%)	Z' (%)
150.	4.63 ±2.11	2.84 ±2.85	±
175.	17.43±1.08	17.73±1.13	±
200.	25.24±0.90	24.02±0.97	23.77±0.92
225.	30.82±0.81	26.29±0.92	29.98±0.83
250.	34.53±0.77	28.75±0.87	33.20±0.78
275.	38.37±0.73	30.79±0.84	35.79±0.75
300.	40.34±0.71	33.10±0.81	37.69±0.73
325.	42.78±0.69	35.91±0.78	39.47±0.72
350.	44.75±0.67	37.65±0.76	41.08±0.70
375.	46.43±0.66	39.38±0.74	42.22±0.69
400.	48.28±0.65	41.36±0.72	43.34±0.68
425.	49.64±0.64	42.81±0.71	44.86±0.67
450.	51.18±0.63	43.47±0.70	45.27±0.67
475.	52.28±0.62	44.06±0.70	46.32±0.66
500.	53.32±0.61	44.77±0.69	47.13±0.65
525.	54.60±0.61	46.14±0.68	48.19±0.65
550.	55.36±0.60	45.39±0.69	49.20±0.64
575.	56.72±0.60	46.59±0.68	49.86±0.64
600.	57.50±0.59	47.51±0.67	50.06±0.63
625.	58.30±0.59	47.33±0.67	50.41±0.63
650.	58.93±0.58	47.92±0.67	50.98±0.63
675.	59.46±0.58	48.08±0.67	51.34±0.63
700.	59.62±0.58	47.73±0.67	51.44±0.63
725.	60.41±0.58	47.72±0.67	51.83±0.62
750.	60.90±0.57	48.32±0.67	51.76±0.63
775.	60.90±0.58	47.68±0.67	51.44±0.63
800.	61.45±0.57	47.12±0.68	51.09±0.63
825.	61.53±0.57	46.47±0.68	51.01±0.63
850.	61.38±0.57	46.11±0.69	51.37±0.63
875.	61.51±0.57	44.81±0.70	50.50±0.64
900.	61.81±0.57	44.67±0.70	49.47±0.64
925.	61.73±0.57	43.24±0.72	49.20±0.65
950.	61.47±0.57	41.79±0.73	48.19±0.65
975.	61.08±0.57	41.06±0.74	47.02±0.66

Table 5.2. The acceptances for q^*, Z', W'

Mass (GeV/c^2)	q^* σ ×BR (pb)	q^* $\sigma \times \mathrm{BR} \times a$ (pb)	W' σ ×BR (pb)	W' $\sigma \times \mathrm{BR} \times a$ (pb)	Z' σ ×BR (pb)	Z' $\sigma \times \mathrm{BR} \times a$ (pb)
150.	47570.80	2202.53	2958.39	84.02	670.41	
175.	22926.90	3996.16	1768.49	313.55	433.14	
200.	11800.50	2978.45	1115.31	267.90	263.92	62.73
225.	6383.61	1967.43	738.70	194.21	180.40	54.08
250.	3628.72	1253.00	498.65	143.36	124.89	41.47
275.	2136.99	819.96	345.98	106.53	89.11	31.89
300.	1300.52	524.63	249.80	82.69	64.52	24.32
325.	796.27	340.64	179.92	64.61	47.35	18.69
350.	501.73	224.52	130.77	49.23	35.04	14.39
375.	320.55	148.83	95.01	37.42	26.11	11.03
400.	207.60	100.23	72.97	30.18	19.10	8.28
425.	135.70	67.36	54.74	23.43	15.39	6.90
450.	88.51	45.30	41.00	17.82	11.73	5.31
475.	59.86	31.29	30.41	13.40	9.26	4.29
500.	40.25	21.46	23.87	10.69	6.89	3.25
525.	27.18	14.84	17.90	8.26	5.33	2.57
550.	18.49	10.24	13.70	6.22	4.36	2.15
575.	12.49	7.09	10.21	4.76	3.14	1.56
600.	8.52	4.90	8.06	3.83	2.47	1.23
625.	5.80	3.38	6.14	2.91	1.92	0.97
650.	4.13	2.44	4.62	2.22	1.46	0.74
675.	2.72	1.62	3.53	1.70	1.13	0.58
700.	1.88	1.12	2.77	1.32	0.87	0.45
725.	1.29	0.78	2.12	1.01	0.68	0.35
750.	0.89	0.54	1.62	0.78	0.52	0.26
775.	0.61	0.37	1.24	0.59	0.40	0.21
800.	0.42	0.26	0.99	0.47	0.31	0.16
825.	0.29	0.18	0.76	0.35	0.24	0.12
850.	0.20	0.12	0.60	0.28	0.20	0.10
875.	0.14	0.09	0.47	0.21	0.15	0.07
900.	0.10	0.06	0.38	0.17	0.12	0.06
925.	0.07	0.04	0.30	0.13	0.09	0.05
950.	0.05	0.03	0.25	0.10	0.07	0.03
975.	0.03	0.02	0.20	0.08	0.03	0.01

Table 5.3. The production cross sections for excited quarks, W' and Z' using CTEQ6.

Table 5.4. The measured resolutions for $0.5 < |\eta| < 1.0$.

$(E_{T,1} + E_{T,2})/2$ (GeV)	Uncorrected Resolutions	Soft Radiation Correction	Particle Correction	Corrected Resolutions
35.1	0.175 ±0.006	0.892	0.063	0.143 ± 0.008
47.4	0.148 ±0.002	0.907	0.047	0.125 ± 0.004
54.2	0.134 ±0.002	0.914	0.042	0.115± 0.003
67.7	0.116 ±0.002	0.927	0.034	0.102± 0.003
86.7	0.108 ±0.001	0.941	0.027	0.098 ± 0.002
104.7	0.096 ±0.001	0.953	0.023	0.089 ± 0.002
130.3	0.089 ±0.001	0.965	0.019	0.084 ± 0.002
155.1	0.090 ±0.001	0.974	0.016	0.086 ± 0.003
182.0	0.069 ±0.001	0.981	0.014	0.066 ± 0.002
212.6	0.074 ±0.003	0.987	0.013	0.072 ± 0.004
256.1	0.076 ±0.004	0.992	0.011	0.075 ± 0.005

Table 5.5. Fit variables for $0.5 < |\eta| < 1.0$.

C	S	N
0.047 ± 0.008	0.783 ± 0.137	0.590 ± 9.334

Table 5.6. Correlation matrix for $0.5 < |\eta| < 1.0$.

Cor(1,1)	Cor(1,2)	Cor(1,3)	Cor(2,2)	Cor(2,3)	Cor(3,3)
1.0000	-0.9633	0.8841	1.0000	-0.9670	1.0000

Table 5.7. Soft radiation correction for $0.5 < |\eta| < 1.0$.

a_0	a_1
1.869 ± 0.274	0.0101 ± 0.0037

Table 5.8. The measured resolutions for $|\eta| < 0.5$.

$(E_{T,1} + E_{T,2})/2$ (GeV)	Uncorrected Resolutions	Soft Radiation Correction	Particle Correction	Corrected Resolutions
35.8	0.182±0.006	0.909	0.060	0.154 ± 0.009
47.3	0.140 ±0.002	0.914	0.046	0.120 ± 0.004
54.3	0.123 ±0.002	0.918	0.040	0.106 ± 0.003
67.7	0.110 ±0.002	0.924	0.032	0.096 ± 0.003
86.4	0.098 ±0.001	0.931	0.025	0.088 ± 0.001
105.1	0.086 ±0.001	0.938	0.021	0.078 ± 0.002
130.4	0.076 ±0.001	0.946	0.017	0.070 ± 0.001
155.5	0.073 ±0.001	0.953	0.014	0.068 ± 0.001
182.4	0.066 ±0.001	0.959	0.012	0.062 ± 0.001
213.4	0.059 ±0.001	0.966	0.010	0.056 ± 0.002
241.7	0.062 ±0.002	0.971	0.009	0.059 ± 0.003
295.2	0.052 ±0.002	0.978	0.007	0.050 ± 0.003

Table 5.9. Fit variables for $|\eta| < 0.5$.

C	S	N
0.033 ± 0.006	0.686 ± 0.065	2.621 ± 0.810

Table 5.10. Correlation matrix for for $|\eta| < 0.5$.

Cor(1,1)	Cor(1,2)	Cor(1,3)	Cor(2,2)	Cor(2,3)	Cor(3,3)
1.0000	-0.9292	0.7600	1.0000	-0.9231	1.0000

Table 5.11. Soft radiation correction for $|\eta| < 0.5$.

a_0	a_1
2.199 ± 0.266	0.0055 ± 0.0026

Table 5.12. Parameters for mass resolutions

Parameter	nominal	+1 σ	-1 σ
A	2.46 ± 0.19	4.99 ± 0.11	-.15E-02 ± 0.18
B	0.82 ± 0.49E-02	-.80 ± 0.57E-02	-.80 ± 0.16E-02
C	-.28E-01 ± 0.17E-03	-.32E-01 ± 0.17E-03	-.26E-01 ± 0.84E-04
D	0.00E+00 ± 0.42E-04	0.56E-06 ± 0.48E-04	0.27E-06 ± 0.22E-04

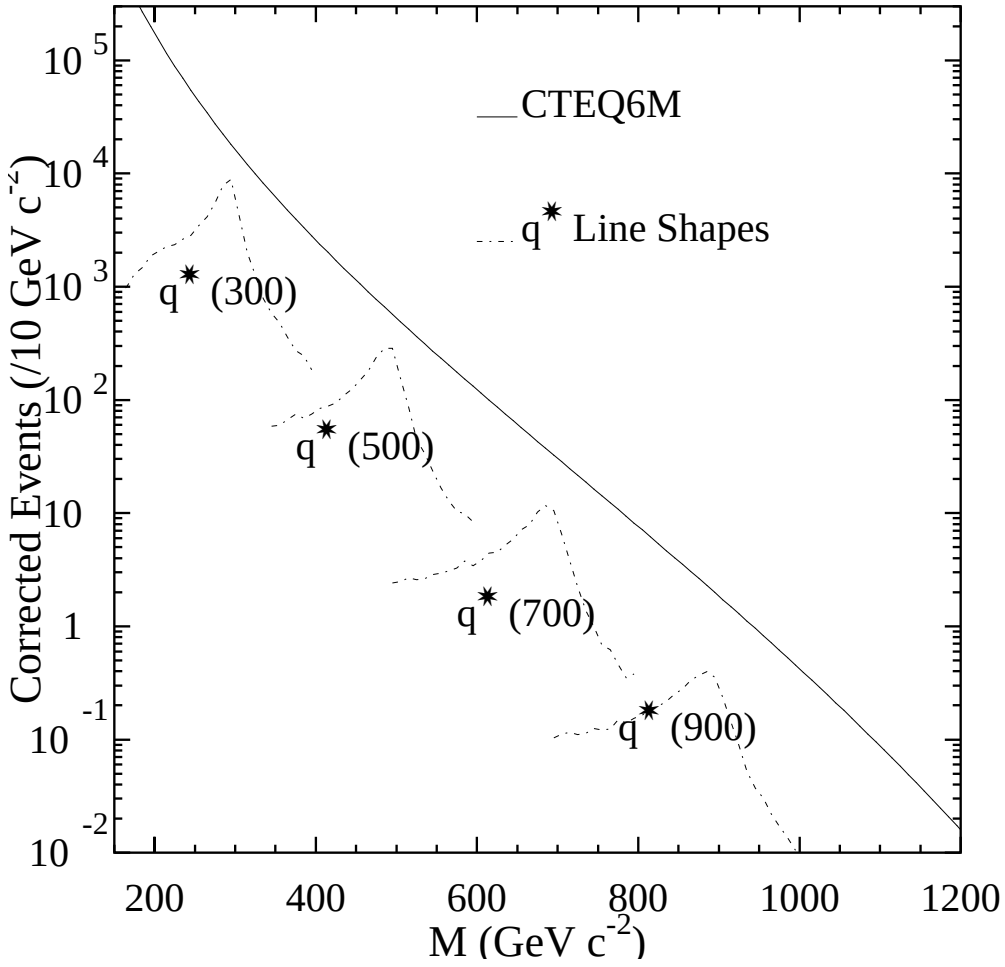

Figure 5.11. Simulated Jetrad, CTEQ6 dijet mass spectrum with excited quark signals superimposed.

CHAPTER 6

CONFIDENCE LIMIT

We have modeled the background and signal and have made the necessary corrections to the data sample. Now, it is time to put confidence limits on the excited quark, W' and Z' models.

The predicted number of events per bin (μ_i) in the mass spectrum is given by:

$$\mu_i = (\sigma_{QCD_i} + N_{X_i}\sigma_X) \times \mathcal{L}_i \times \epsilon_{\text{vert}} \times \omega_i^{-1} \times C_i, \tag{6.1}$$

where σ_{QCD_i} is the predicted JETRAD cross section for the mass bin, $\mathcal{L}_i$ is the integrated luminosity per bin, N_{X_i} is the fraction of the signal in the bin ($\sum N_{X_i} = 1$), σ_X is the signal cross section, ϵ_{vert} is the efficiency of the vertex selection, ω_i is the event weighting based on the jet quality cut efficiencies and C_i represents the energy resolution and jet energy scale corrections per bin.

The probability that N_i events were observed in a given mass bin is then given by (assuming that N_i follows Poisson statistics):

$$P\left(N_i \mid \sigma_{QCD_i}, \sigma_X, N_{X_i}, \mathcal{L}_i, \epsilon_{\text{vert}}, \omega_i^{-1}, C_i, I\right) = \frac{e^{-\mu_i}\mu_i^{N_i}}{N_i!}, \tag{6.2}$$

where I is all other prior information. The probability of observing the set of N_i events that makes up the mass spectrum is given by the product of these probabilities:

$$P\left(N_1,\ldots,N_n \mid \sigma_{QCD_i},\sigma_X,N_{X_i},\mathcal{L}_i,\epsilon_{\rm vert},\omega_i^{-1},C_i,I;(i=1\ldots n)\right)=\prod_{i=1}^{n}\left(\frac{e^{-\mu_i}{\mu_i}^{N_i}}{N_i!}\right). \tag{6.3}$$

We are interested in determining the probability distribution for σ_X, so application of Bayes' theorem to Equation 6.2 yields [49]:

$$P(\sigma_X,\zeta)=\frac{\int_{(\zeta)}P(N_1,\ldots,N_n \mid \zeta,I;(i=1\ldots n))}{\int_{(\sigma_X,\zeta)}P(N_1,\ldots,N_n \mid \sigma_X,\zeta,I;(i=1\ldots n))}. \tag{6.4}$$

where $\zeta=\sigma_{QCD_i},N_{X_i},\mathcal{L}_i,w_i^{-1},C_i$.

When solving this equation we make the following assumptions about the prior probability distributions: σ_X has a flat prior; σ_{QCD_i}, $\epsilon_{\rm vert}$, $\mathcal{L}_i$, ω_i^{-1} and C_i all have Gaussian priors; N_{X_i} has a Poisson prior. The integral equation will be solved using standard numerical integration techniques.

6.1 Confidence Limit Algorithm

The confidence limit algorithm incorporates the principles described in the previous section. Specifically, a numerical integration is performed with n steps, where n can range from 100-250 depending on the mass point being studied. The integration is conducted from $\sigma_1=0$ to σ_n, where σ_n is a cross section expected to be above the 95 % confidence level. The numerical integration takes the form of

$$\sum_{i}^{n}P(\sigma_i), \tag{6.5}$$

where $\sigma_i=i*\Delta\sigma$ and $\Delta\sigma=\frac{\sigma_n}{n}$.

Nested within this numerical integration, the uncertainties are incorporated into the limit by varying values randomly within the uncertainties then determining the predicted number of events for each bin using Eqn. 6.1, determining

the probability for each bin and summing up the probabilities for all bins. This is repeated 1×10^6 times and all the probabilities are added and divided by the total number of iterations (1×10^6). The average probability is stored for that particular step.

After the numerical integration has stepped through all of the cross section values and determined the average probability for each step, then the probabilities are added. The cross section at which the summed probabilities add to 0.95 is taken as the 95% confidence level, σ_x.

6.2 Uncertainties

The uncertainty in integrated luminosity ($\mathcal{L}$) is 5.8% , and the uncertainty in the event weights is 1% . Uncertainties in the signal line shapes are determined by the size of the sample. The energy scale errors are incorporated using the energy scale error matrix in Table 6.1. All other errors are given in Tables 4.6, 4.7 and 6.3. These uncertainties are incorporated into the limit calculation using the method discussed in the previous section. The uncertainties in the energy scale are by far the largest source of uncertainty (see Figure 3.9 and Table 6.3).

The uncertainties in the dijet mass resolution corrections to the JETRAD background model and the single jet resolutions to the signal models are incorporated into the confidence limit using parameterizations of the resolution curves shown in Figures 5.7 and 5.9 to smear the nominal values. A total of 61 curves for the signal and 61 curves for the background are used that represent the nominal smearing and deviations from the nominal up to $\pm 3\sigma$ in increments of 0.1σ. The limit calculator chooses a curve in each iteration using a Gaussian weighted random number. The resolution smearing values are determined by the dijet mass resolutions for the JETRAD background and by the single jet

1	2	3	4	5	6	7	8	9	10	11	12	13	14	15	16	17	18	19	20	21	22	23	24
1.00	0.99	0.96	0.94	0.92	0.90	0.87	0.85	0.82	0.80	0.77	0.74	0.71	0.68	0.64	0.61	0.57	0.54	0.50	0.47	0.43	0.39	0.34	0.30
	1.00	0.98	0.97	0.95	0.93	0.90	0.88	0.86	0.83	0.81	0.78	0.75	0.72	0.68	0.65	0.61	0.58	0.54	0.51	0.47	0.43	0.38	0.34
		1.00	0.99	0.98	0.96	0.94	0.92	0.90	0.88	0.85	0.83	0.81	0.77	0.74	0.70	0.67	0.64	0.60	0.57	0.53	0.49	0.44	0.40
			1.00	0.99	0.98	0.96	0.95	0.93	0.92	0.89	0.87	0.85	0.81	0.78	0.75	0.72	0.69	0.65	0.62	0.58	0.54	0.50	0.45
				1.00	0.99	0.98	0.97	0.96	0.94	0.92	0.90	0.88	0.85	0.82	0.79	0.76	0.73	0.69	0.67	0.63	0.59	0.55	0.50
					1.00	0.99	0.98	0.97	0.96	0.94	0.92	0.90	0.88	0.85	0.83	0.80	0.77	0.73	0.71	0.68	0.63	0.59	0.55
						1.00	0.99	0.99	0.97	0.96	0.95	0.93	0.91	0.88	0.86	0.83	0.81	0.78	0.75	0.72	0.68	0.64	0.60
							1.00	0.99	0.99	0.98	0.97	0.95	0.94	0.92	0.90	0.87	0.85	0.82	0.80	0.77	0.74	0.70	0.66
								1.00	1.00	0.99	0.98	0.97	0.95	0.94	0.92	0.90	0.88	0.85	0.83	0.81	0.77	0.74	0.70
									1.00	1.00	0.99	0.98	0.97	0.95	0.94	0.92	0.90	0.88	0.86	0.84	0.80	0.77	0.74
										1.00	0.99	0.99	0.98	0.97	0.95	0.94	0.92	0.90	0.88	0.86	0.83	0.80	0.77
											1.00	1.00	0.99	0.98	0.97	0.95	0.94	0.92	0.91	0.89	0.86	0.83	0.80
												1.00	1.00	0.99	0.98	0.97	0.96	0.94	0.93	0.91	0.88	0.86	0.83
													1.00	0.99	0.99	0.98	0.97	0.95	0.94	0.93	0.91	0.88	0.86
														1.00	1.00	0.99	0.98	0.97	0.96	0.95	0.93	0.91	0.89
															1.00	1.00	0.99	0.98	0.97	0.96	0.95	0.93	0.91
																1.00	1.00	0.99	0.98	0.97	0.96	0.95	0.93
																	1.00	1.00	0.99	0.98	0.97	0.96	0.95
																		1.00	1.00	0.99	0.98	0.97	0.96
																			1.00	0.99	0.99	0.98	0.97
																				1.00	0.99	0.99	0.98
																					1.00	0.99	0.99
																						1.00	0.99
																							1.00

Table 6.1. The correlations for the uncertainty due to energy scale response for $|\eta| < 1.0$. The numbers 1-24 correspond to 24 mass bins, see Table 6.2 for a list of bins. Not shown is the 190 to 210 bin.

$mass_{min}$ Gev/c^2	$mass_{max}$ Gev/c^2
190.	210.
210.	230.
230.	250.
250.	270.
270.	290.
290.	320.
320.	340.
340.	360.
360.	380.
380.	400.
400.	420.
420.	440.
440.	470.
470.	500.
500.	530.
530.	560.
560.	590.
590.	630.
630.	660.
660.	700.
700.	750.
750.	800.
800.	850.
850.	1400.

Table 6.2. Bins used in the uncertainty matrix table.

resolutions for the PYTHIA signal models. Typical correction values are plotted in Figure 5.10.

6.3 Fitting the Data with the Inclusive QCD Dijet Mass Spectrum

The data are fitted to the QCD NLO prediction by using the above method with σ_X set to zero. The QCD prediction is effectively normalized to the background data. This is done to avoid the uncertainties QCD predictions for the inclusive jet cross section and the dijet mass spectrum which can vary as much as 30% depending on choice of parton distribution function (PDF) or renormalization scale (μ) [50–51]. Currently, measurements of uncertainties in the theory are not well understood. This is changing now that the new PDF's,

Uncertainty	(%)
Jet energy scale	7.5-28.4
Luminosity RunIa,b	5.8
Trigger matching	4.9
Event weighting (ω)	1.
ϵ_{vert}	.68-.73
Luminosity matching RunIa/b	0.08

Table 6.3. Uncertainties

starting with CTEQ6 are including more meaningful uncertainty information. Variations in PDF's and the renormalization factorization scale of the QCD prediction result in a smooth change in the normalization of the cross section curve; because our analysis does not interpret normalization differences as evidence of a resonance it is therefore insensitive to such parameter changes. To illustrate what a signal would look like, simulated 500 GeV/c^2 excited quark was added to the data and the result can be seen in Figure **??**.

The JETRAD data are generated using the theoretical NLO prediction in which the coupling constant α_s is renormalized each event by $\mu = 0.5E_T$ of the most energetic jet, E_T^{max}. Additionally, we chose $\mu_f = \mu$, where μ_f is the factorization scale and isolates the non-perturbative cross section contributions from the perturbative, calculable, hard scattering cross section contributions. The standard choice of $\mu = \mu_f = 0.5E_T^{max}$ appears to be a saddle point, meaning that larger and smaller choices of μ result in smaller values for the cross section [9].

A comparison between JETRAD and the data is given in Figures 6.1, 6.2, 6.3 and 6.4 for four different PDF's. All four PDF's give acceptable agreement with the data as indicated by the displayed χ^2 statistic for 24 degrees of freedom (25

data points - 1 for absolute normalization). CTEQ4 and below do not include inclusive jet data from CDF or DØ which means information about jets at higher energies is incomplete. A closer look at agreement at higher energies shows that CTEQ4HJ fits better than CTEQ4 but the problem with this PDF is that it weighted the higher energy jet information. CTEQ6M gives a comparable fit at higher energies but does not need to weight the jet information at higher energies. The CTEQ6 [42] PDF is based on the most recent assessment of input data, namely CDF and DØ inclusive jet cross section results, and is considered here as representative of the best current knowledge of the theoretical QCD prediction.

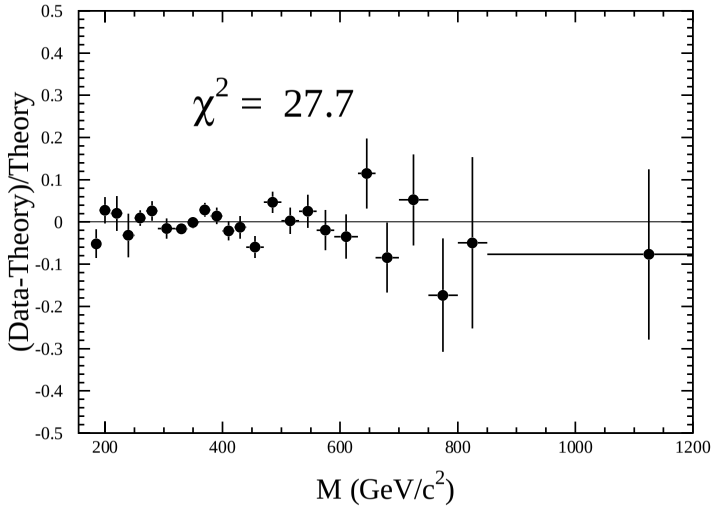

Figure 6.1. The difference between the data and the smeared JETRAD NLO QCD prediction normalized to the theoretical prediction ((Data − Theory)/Theory) using the CTEQ3M PDF and a renormalization scale $\mu = 0.5E_T$. The errors are statistical.

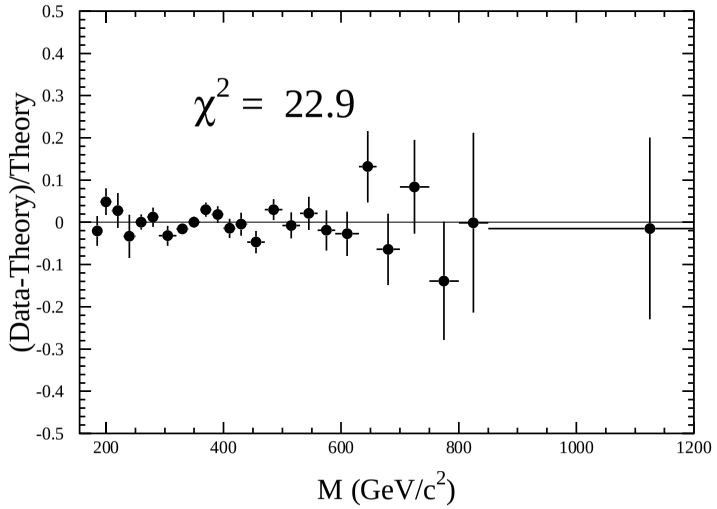

Figure 6.2. The difference between the data and the smeared JETTRAD NLO QCD prediction normalized to the theoretical prediction ((Data − Theory)/Theory) using the CTEQ4M PDF and a renormalization scale $\mu = 0.5E_T$. The errors are statistical.

6.4 Extraction of Signal Limits

Confidence limits σ_X are reported at the integrated probability distribution value of 0.95 or the 95% confidence level:

$$0.95 = \int_0^{U_L} P(\sigma_X) d\sigma. \tag{6.6}$$

The 95% confidence limit is the upper limit(U_L) at which the integral is 0.95. See Figure 6.6 for an example of how the limit is determined for one dijet mass point.

The cross section limits for the q^*, $W'$and Z' are given in Table 6.4 and are depicted in Figure 6.7.

The 95% confidence limits and theoretical production cross sections for the q^*, W' and Z' models are plotted in Figures 6.8, 6.10 and 6.11. The dashed lines

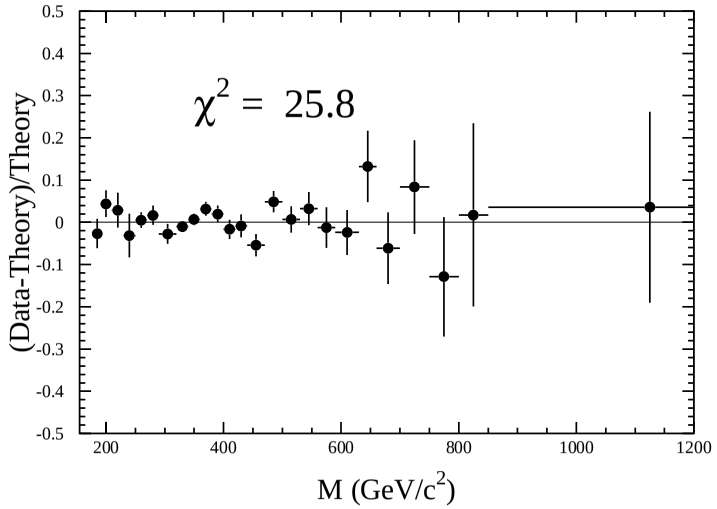

Figure 6.3. The difference between the data and the smeared JETTRAD NLO QCD prediction normalized to the theoretical prediction ((Data−Theory)/Theory) using the CTEQ4HJ PDF and a renormalization scale $\mu = 0.5E_T$. The errors are statistical.

for each plot are the theoretical production cross sections adjusted for detector acceptance and branching ratio ($\sigma \times \mathrm{BR} \times a$), discussed in section 5.1.3. The 95% confidence limits and theoretical production cross sections for the fictional q^* at 500 GeV/c^2 are plotted in Figure 6.9.

The DØ 95% Confidence Limits on the production cross section ($\sigma_X \times \mathrm{BR} \times a$) for q^* in terms of the excited quark coupling parameters (f') are compared to those limits measured by UA2 [52] and CDF [53] in Figure 6.12.

6.5 Conclusion

A search for new particles decaying to dijets in the DØ detector has been carried out. Using Figures 6.8, 6.10 and 6.11, we exclude at the 95% confidence level the production of excited quarks with masses below 770 GeV, the W' is excluded between 300 GeV and 830 GeV and the Z' is excluded between 420 GeV and 620 GeV, respectively.

Table 6.4. The 95% Confidence Limits on the production cross section ($\sigma_X \times \mathrm{BR} \times a$) for the q^*, $W'$and Z'.

Mass (GeV)	q^* (pb)	W' (pb)	Z' (pb)
200.	161.00	144.00	143.00
225.	196.00	143.00	145.00
250.	159.00	146.00	146.00
275.	126.00	146.00	145.00
300.	52.50	115.00	116.00
325.	27.00	27.00	30.00
350.	14.00	18.00	15.00
375.	12.50	17.00	13.00
400.	9.20	14.00	10.00
425.	4.80	6.99	5.66
450.	3.00	4.00	3.00
475.	2.40	3.33	2.66
500.	2.00	3.00	2.33
525.	1.80	2.66	2.00
550.	1.40	2.33	1.66
575.	1.00	1.66	1.33
600.	1.00	1.33	1.00
625.	0.80	1.26	1.00
650.	0.80	0.79	1.02
675.	0.60	1.08	0.93
700.	0.60	0.93	0.78
725.	0.60	0.64	0.69
750.	0.40	0.27	0.60
775.	0.40	0.52	0.48
800.	0.20	0.30	0.44
825.	0.20	0.28	0.39
850.	0.20	0.41	0.31
875.	0.20	0.33	0.27
900.	0.20	0.24	0.33
925.	0.20	0.34	0.g33
950.	0.20	0.39	0.30
975.	0.20	0.33	0.30
1000.	0.20	0.00	0.30

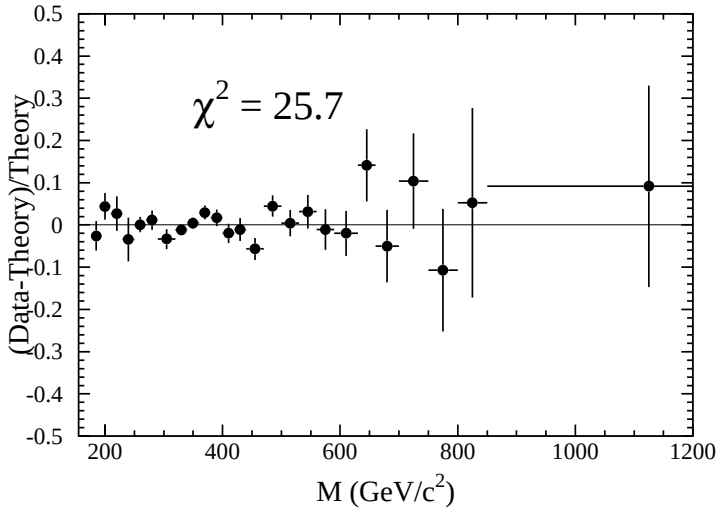

Figure 6.4. The difference between the data and the smeared JETTRAD NLO QCD prediction normalized to the theoretical prediction ((Data − Theory)/Theory) using the CTEQ6M PDF and a renormalization scale $\mu = 0.5E_T$. The errors are statistical.

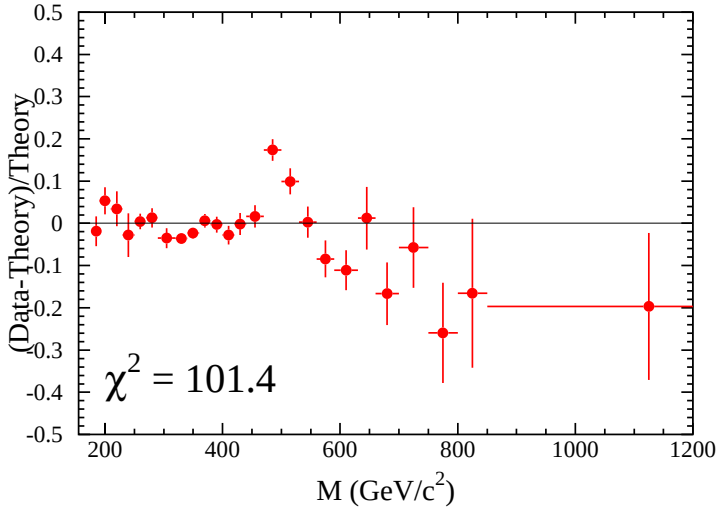

Figure 6.5. The difference between the data and the smeared JETTRAD NLO QCD prediction normalized to the theoretical prediction ((Data − Theory)/Theory) using the CTEQ6M PDF and a renormalization scale $\mu = 0.5E_T$ with an excited quark signal at 500 GeV/c^2. The errors are statistical.

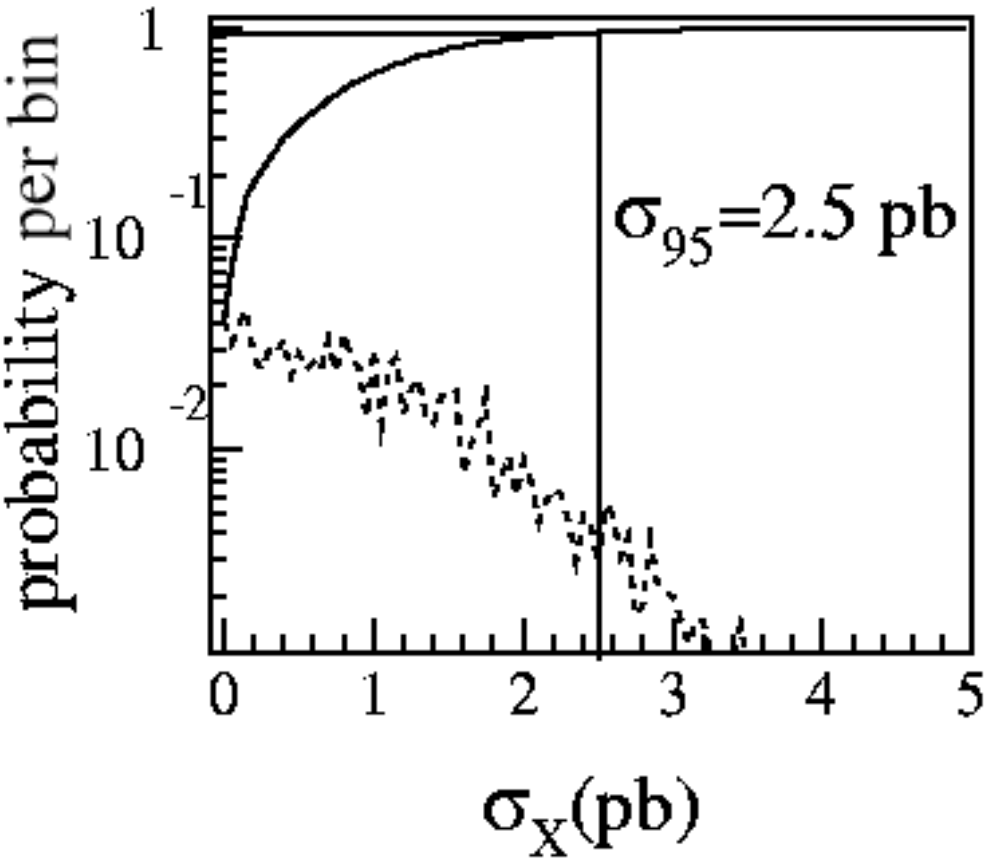

Figure 6.6. The probability distribution for an excited quark of mass 500 GeV as a function of σ_X. The dashed line shows the probability distribution as a function of σ_X and the solid line shows the integrated probability distribution as a function of σ_X. The point at which the solid curved line reaches .95 probability determines σ_X to the 95% confidence level. In this case it is 2.5 pb.

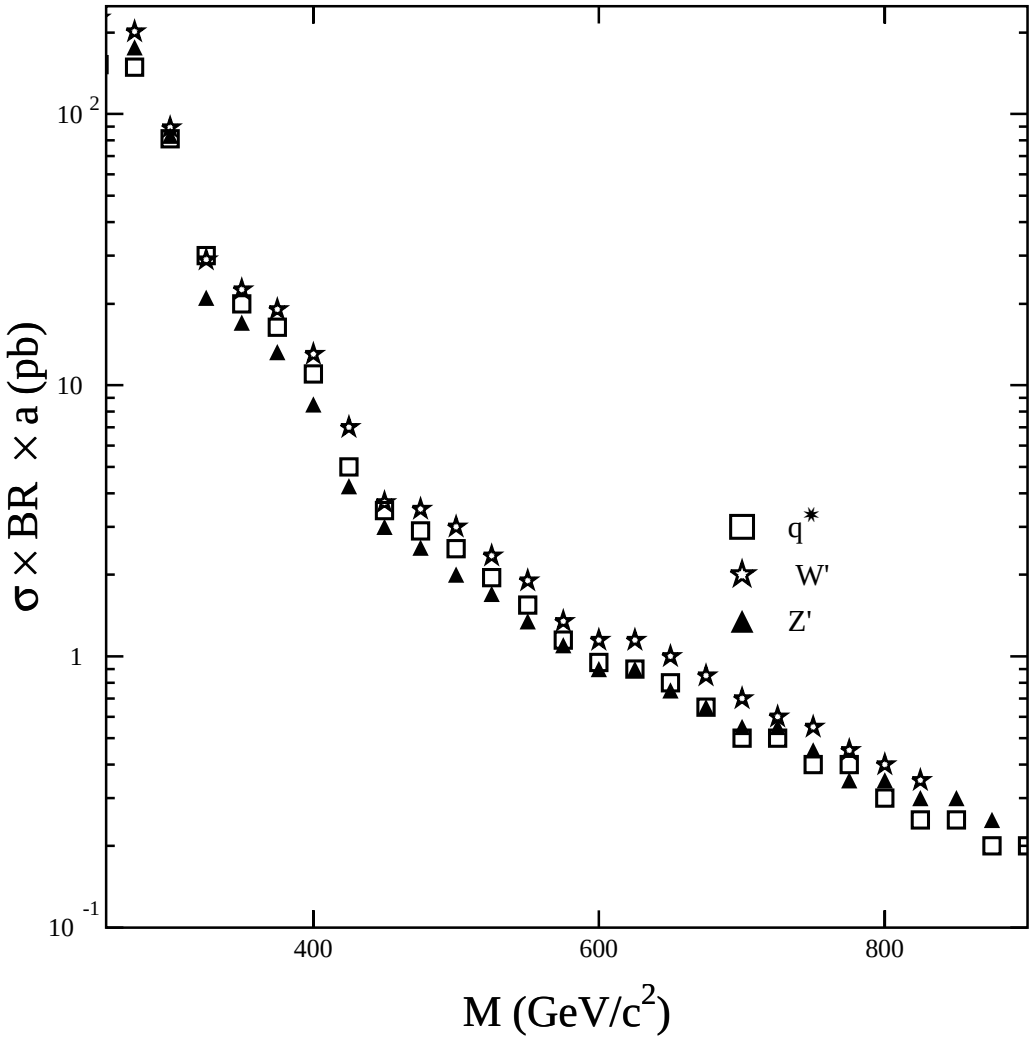

Figure 6.7. The 95% Confidence Limits on the production cross section ($\sigma_X \times \mathrm{BR} \times a$) for the q^*, Z' and W' models.

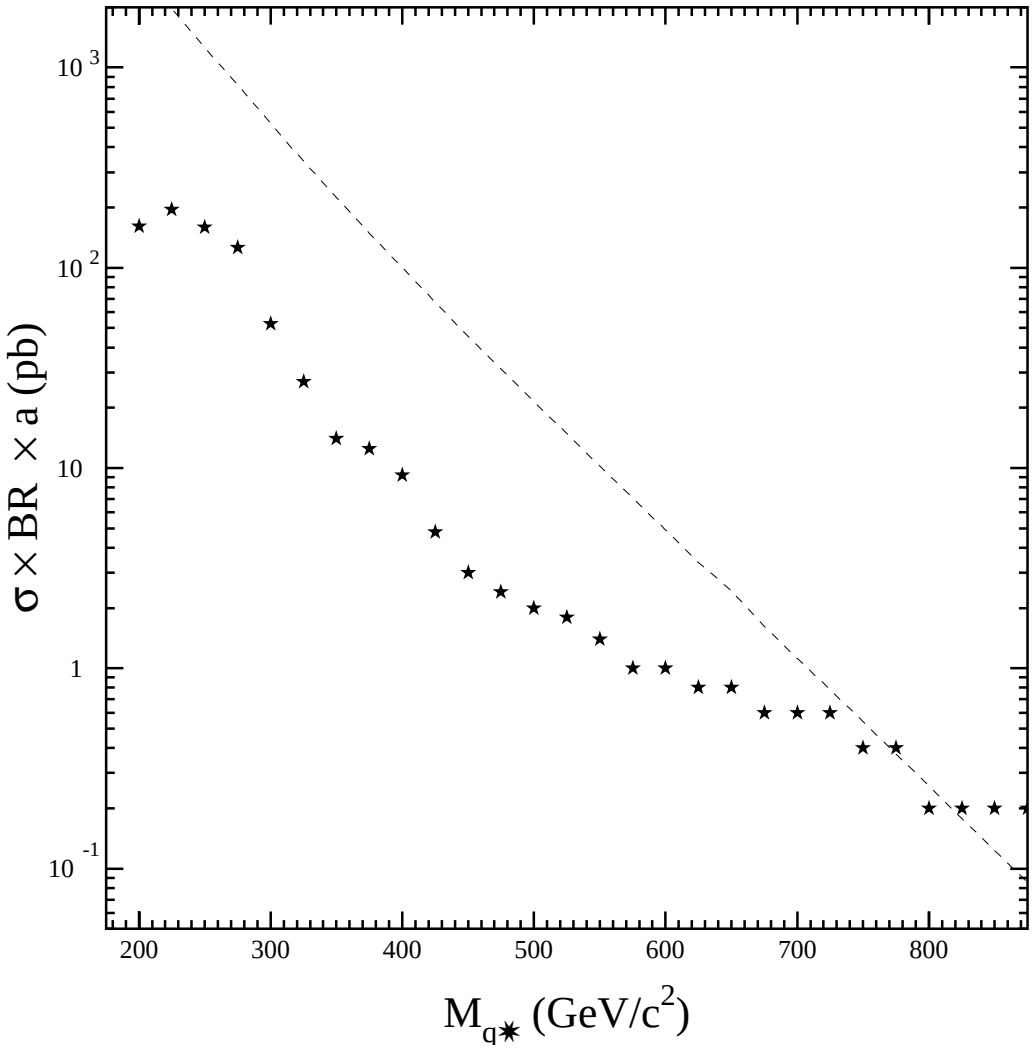

Figure 6.8. The 95% Confidence Limits on the production cross section ($\sigma_X \times \mathrm{BR} \times a$) for the q^* (solid squares) compared with the predicted cross section (dashed line). Values of $M_{q^*} < 770$ GeV are excluded at the 95% confidence level.

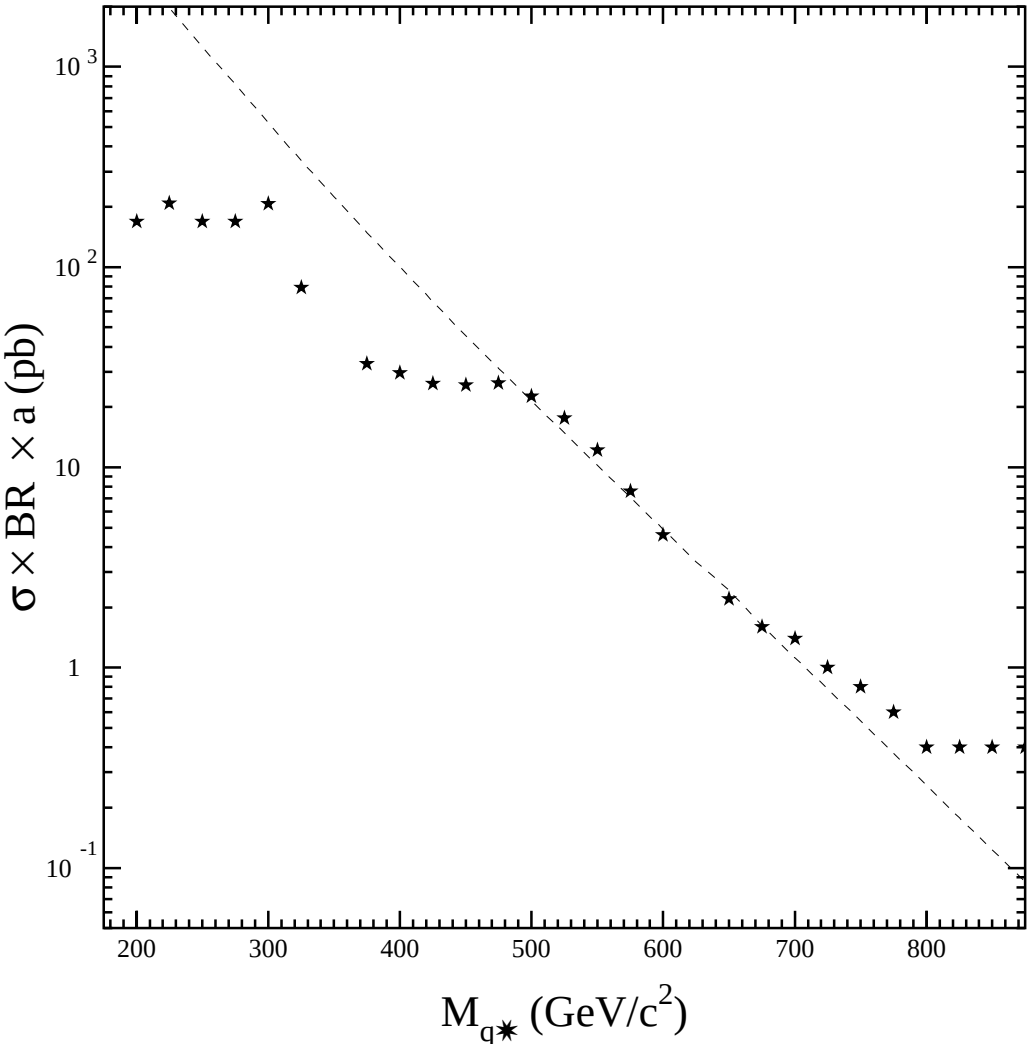

Figure 6.9. Confidence Limits on the production cross section ($\sigma_X \times \mathrm{BR} \times a$) for the q^* (solid squares) with a fictional excited quark signal at 500 GeV/c^2 compared with the predicted cross section (dashed line). Notice we can not exclude theory above around 475 GeV/c^2.

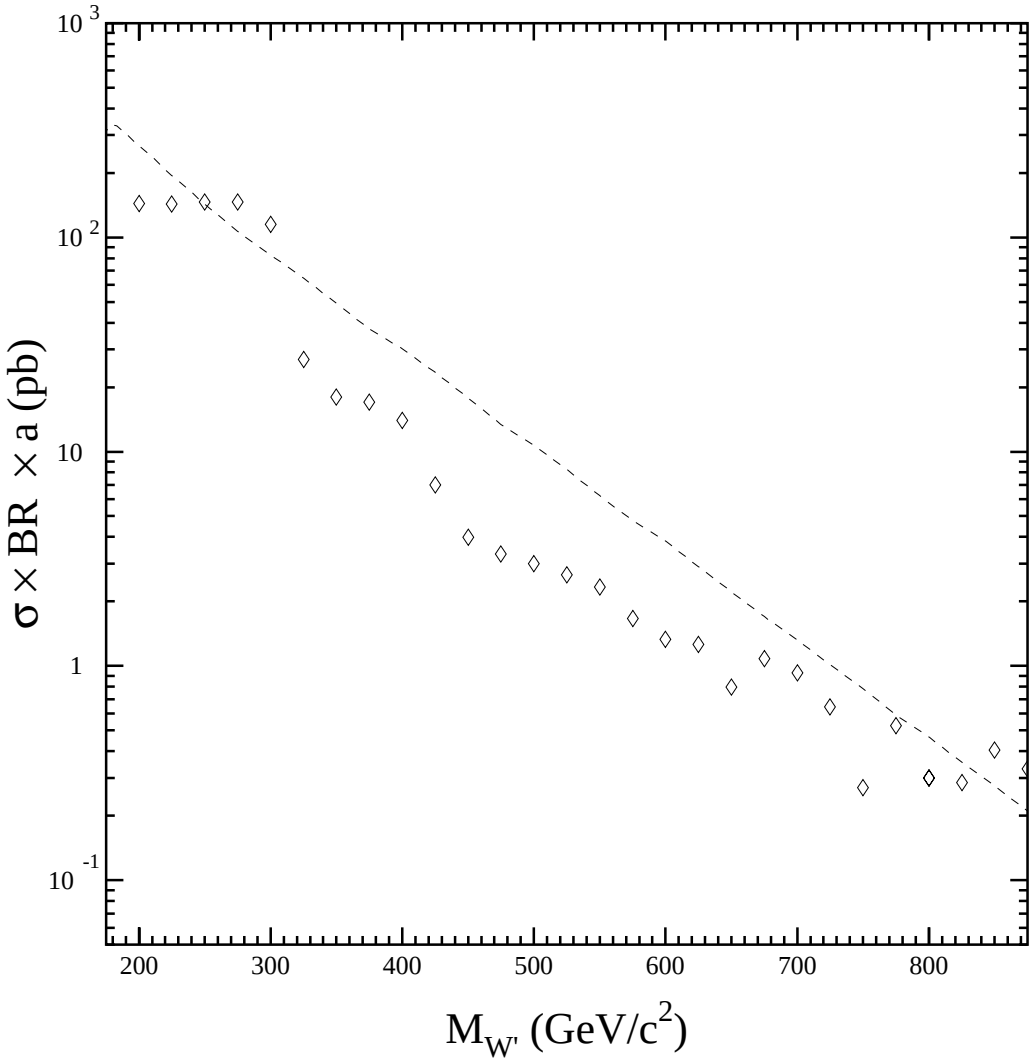

Figure 6.10. The 95% Confidence Limit on the production cross section ($\sigma_X \times \mathrm{BR} \times a$) for the W' (solid stars) compared with the predicted cross section (dashed line). Values of $300 < M_{W'} < 830$ GeV are excluded at the 95% confidence level.

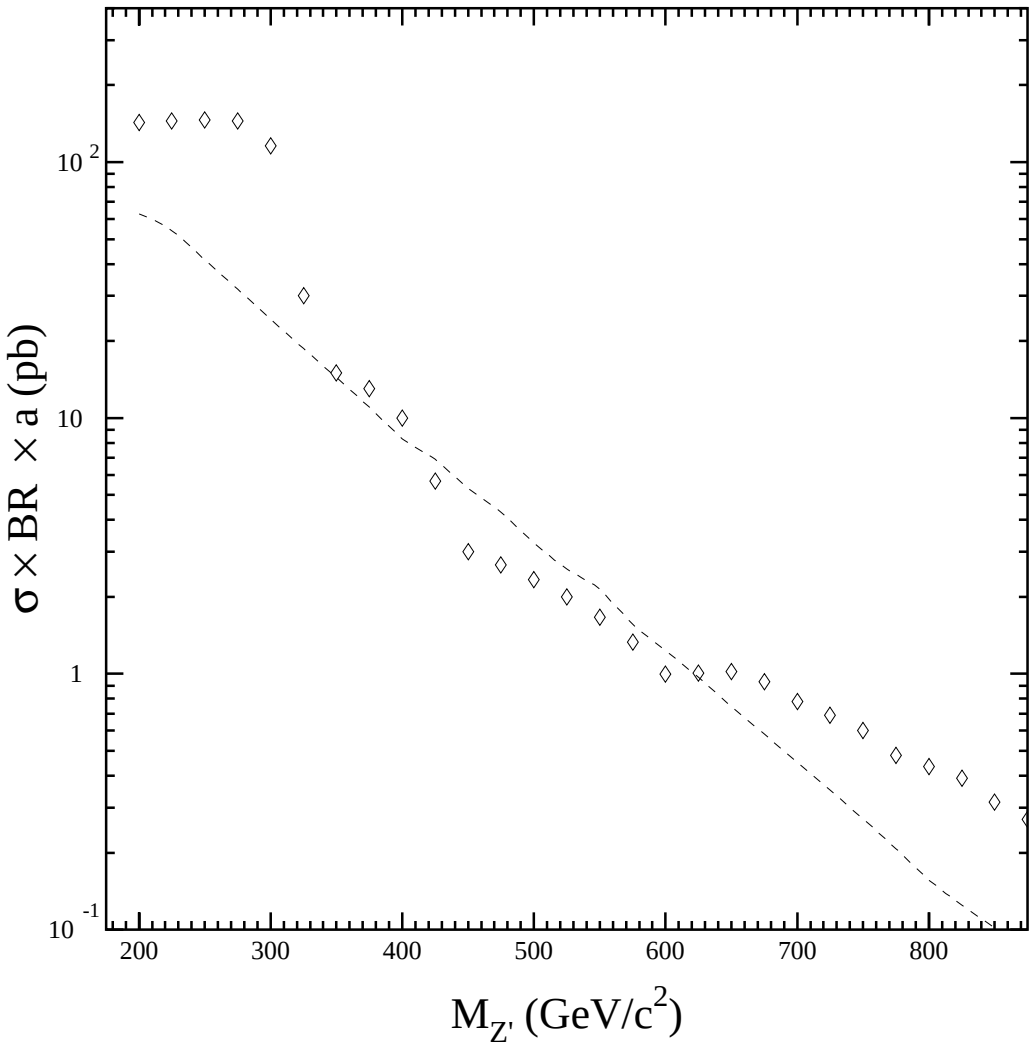

Figure 6.11. The 95% Confidence Limit on the production cross section ($\sigma_X \times \mathrm{BR} \times a$) for the Z' (solid triangles) compared with the predicted cross section (hashed line). Values of $420 < M_{Z'} < 620$ GeV are excluded at the 95% confidence level.

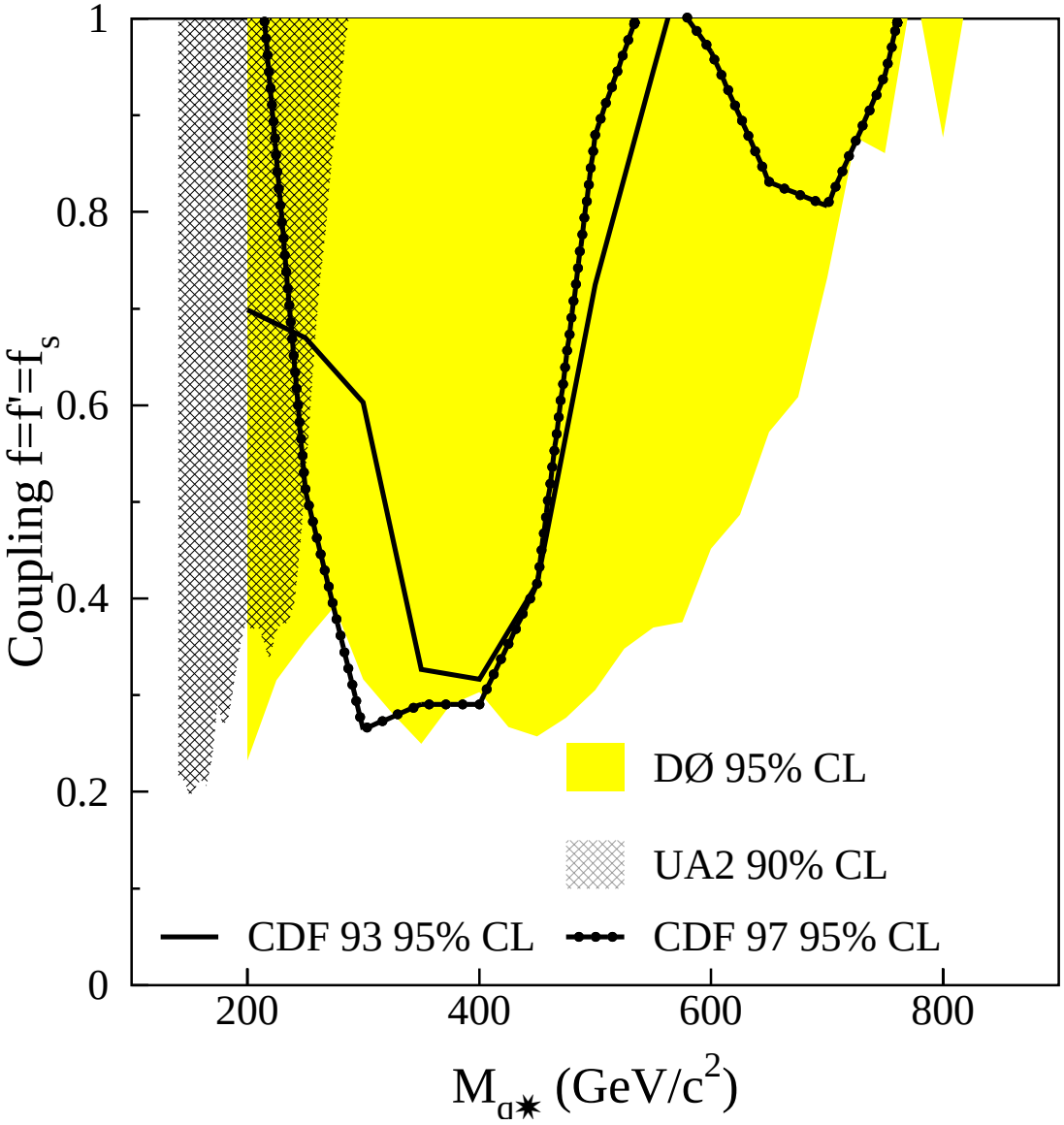

Figure 6.12. A comparison of the DØ 95% Confidence Limit on the production cross section ($\sigma_X \times \mathrm{BR} \times a$) for q^* in terms of the excited quark coupling parameters to those limits measured by UA2 [52] and CDF [53]

BIBLIOGRAPHY

[1] J. J. Thomson. "Cathode Rays," Philosophical Magazine, **44**, 293 (1897).

[2] K. Hagiwara *et al.*, Particle Data Group Collaboration, "Review of Particle Physics," Phys. Rev. D **66**, 010001 (2002).

[3] "http://particleadventure.org/particleadventure/" "http://www.aip.org/history/".

[4] D. Griffiths, "Introduction to Elementary Particles," John Wiley and Sons, Inc., 1987.

[5] V. D. Barger and R. J. N. Phillips, "Collider Physics, Updated Edition," Addison-Wesley Publishing Company, Inc., 1997.

[6] J. McDonald, "Search for Single Top Production with the DØ Detector at the Fermilab Tevatron Collider," Ph.D. Thesis (1999), Florida State University.

[7] I. Bertram, "A Search for New Intermediate Vector Bosons and Excited Quarks decaying to Two-Jets at the CERN $p\overline{p}$ Collider," Ph.D. Thesis (1993), University of Melbourne.

[8] R.K. Ellis, W.J. Stirling, and B.R. Webber, "QCD and Collider Physics," Cambridge University Press, 1996.

[9] J. Krane, "The Ratio of Inclusive Jet Cross Sections at $\sqrt{s} = 630$ GeV and $\sqrt{s} = 1800$ GeV," Ph.D. Thesis (1998), University of Nebraska.

[10] M. Schmelling, "Status of the strong coupling constant," arXiv:hep-ex/9701002.

[11] V.N. Gribov, "Lectures at the 12th Winter School of the Lenningrad Nuclear Physics Institute," SLAC-TRANS-176 (1977).

[12] J. Hewett and T. Rizzo, "Low-Energy Phenomenlogy of Superstring-Inspired E_6 Models," Phys. Rep. 183 (1989).

[13] G. Altarelli, B. Mele, M. Ruiz-Altaba, "Searching for new heavy vector bosons in $p\overline{p}$ colliders," Z. Phys. **C45** 109 (1989).

[14] B. Abbott *et al.*, DØ Collaboration, "Measurement of Dijet Angular Distributions and Search for Quark Compositeness," Phys. Rev. Lett. **80**, 4 (1998).

[15] U. Baur, I. Hinchcliffe and D. Zeppenfeld, "Excited-quark and -lepton production at hadron colliders," Int. J. Mod. Phys. **A2**, 1285 (1987);
U. Baur, M. Spira and P.M. Zerwas, "Excited Quark and Lepton Production at Hadron Colliders," Phys. Rev. **D42**, 815 (1990).

[16] J. Thompson. "Introduction to Colliding Beams at Fermilab," Fermilab Tech. Memo, TM-1909 (1994).

[17] S. Abachi, *et al.*, DØ Collaboration, "The DØ Detector," Nucl. Intr. Methods **A338** 185-253 (1994).

[18] D. A. Edwards and M. J. Syphers, "An Introduction to the Physics of High Energy Accelerators," John Wiley and Sons, NY, 1993.

[19] Main Ring Rookie Book,
"http://www-bdnew.fnal.gov/operations/rookie_books/mainring/intro.html".

[20] Antiproton Rookie Book,
"http://www-bdnew.fnal.gov/operations/rookie_books/pbar_book/contents.html".

[21] M. D. Church and J. P. Marriner, "The Antiproton Sources: Design and Operation," Annu. Rev. Nucl. Part. Sci. **43** 253-95 (1993).

[22] R. Wigmans, "Calorimetry: Energy Measurement in Particle Physics," Claredon, Oxford, 2000.

[23] B. Abbott *et al.*, DØ Collaboration, "High-p_T Jets in $p\bar{p}$ Collisions at $\sqrt{s} = 630$ and 1800 GeV," Phys. Rev. **D64**, 032003 (2001).

[24] J. Huth, *et al.*, in Proceedings of the "Research Directions for the Decade," Snowmass, 1990, edited by E.L. Berger, World Scientific, Singapore (1992).

[25] B. Abbott, *et al.*, "Fixed cone jet definitions at DØ and R(sep)," Fermilab-Pub-97/242-E.

[26] B. Abbott, *et al.*, "Jet Energy Scale," DØ Internal Note #3287 (1997).

[27] B. Abbott, *et al.*, DØ Collaboration, "Determination of the Absolute Jet Energy Scale in the DØ Calorimeters," Nucl. Instr. and Meth. **A424** 352 (1999).

[28] J. Krane, "Jet Energy Scale at DØ for $\sqrt{s} = 630$ GeV," DØ internal note #3288 (1997).

[29] Jet Energy Scale Group,"Jet Energy Scale (Cafix 5.1)," DØ Internal Note #3139 (1996).

[30] J. Bantly *et al.*, "Improvement to the DØ Luminosity Monitor Constant," Fermilab-TM-1930.

[31] K. Frame, T. Geld, and K. Fatyga, "Trigger Efficiencies for Run 1B Inclusive Jet Trigger," DØ Internal note #3178 (1997).

[32] I. Bertram, *et al.*, "The Dijet Mass Spectrum at DØ," DØ Internal note # 3412 (1998).

[33] J. Bantly, *et al.*, "DØ Luminosity Monitor Constant for the 1994-1996 Tevatron Run," Fermilab-TM-1995.

[34] M. Albrow, *et al.*, "Comparison of the Total Cross Sections Measurements of CDF and E811," Fermilab-TM-2071.

[35] N. Amos, *et al.*, DØ Collaboration, "A Luminosity Independent Measurement of the $p\overline{p}$ Total Cross Section at $\sqrt{s} = 1.8$ TeV," Phys. Lett. **B242**, 158 (1990).

[36] F. Abe, *et al.*, CDF Collaboration, "Measurement of the $p\overline{p}$ Total Cross Section at $\sqrt{s} = 546$ and $\sqrt{s} = 1800$ GeV," Phys. Rev. **D50**, 5550 (1994).

[37] C. Avila *et al.*, E811 Collaboration,"A Measurement of the Proton-Antiproton cross-section at $\sqrt{s} = 1.8$ TeV," Phys. Let **B445**, 419 (1999).

[38] V. A. Elvira, "Measurement of the Inclusive Jet Cross Sections at $\sqrt{s} = 1.8$ TeV with the DØ Detector," Ph.D. Thesis (1994), Universidad de Buenos Aires.

[39] L. Babukhadia, *et al.*, "Standard Jet Cuts and their Efficiencies for the Run 1 B DØ Collider Data," DØ Internal Note #3407 (1998).

[40] T. Sjostrand, P. Eden, C. Friberg, L. Lonnblad, G. Miu, S. Mrenna and E. Norrbin, "High-Energy Physics Event Generation with Pythia 6.1," Computer Physics Commun. **135** 238 (2001).

[41] J. Botts, J. G. Morfin, J. F. Owens, J. W. Qiu, W. K. Tung and H. Weerts, CTEQ Collaboration, "CTEQ Parton Distributions And Flavor Dependence Of Sea Quarks," Phys. Lett. **B304**, 159 (1993) [arXiv:hep-ph/9303255].

[42] J. Pumplin, *et al.*, "New Generation of Parton Distributions with Uncertainties from Global QCD Analysis," HEP-PH/0201195 (2002).

[43] I. Bertram, *et al.*, "Single Jet Resolutions at DØ," DØ internal note # 3414 (1998).

[44] R. Hamberg, W. L. van Neerven and T. Matsuura, "A Complete Calculation of the Order α_s^2 Correction To The Drell-Yan K Factor," Nucl. Phys. B **359**, 343 (1991) [Erratum-ibid. B **644**, 403 (2002)].

[45] W. T. Giele, E. W. Glover and D. A. Kosower, "Higher Order Corrections To Jet Cross-Sections In Hadron Colliders," Nucl. Phys. B **403**, 633 (1993) [arXiv:hep-ph/9302225].

[46] V. Elvira et al., "A Study of Standard Jet Cuts and their Efficiencies Using DØ Collider Data," DØ Internal note #1763 (1993).

[47] L. Babukhadia, "Talk presented to the QCD Meeting," DØ Internal note #3373 (1997).

[48] F. James and M. Roos, "'Minuit, A System For Function Minimization And Analysis Of The Parameter Errors And Correlations," Comput. Phys. Commun. **10**, 343 (1975).

[49] I. Bertram *et al.*, "A Recipe for the Construction of Confidence Limits," DØ Internal Note #2775A (1995).

[50] B. Abbott, *et al.*, DØ Collaboration, "Dijet Mass Spectrum and a Search for Quark Compositemess in $p\overline{p}$ Collsions at $\sqrt{s} = 1.8$ TeV," Phys. Rev. Lett. **82**, 2457 (1999).

[51] B. Abbott, *et al.*, DØ Collaboration, "Inclusive Jet Cross Section in $p\overline{p}$ collisions at $\sqrt{s} = 1.8$ TeV," Phys. Rev. Lett. **82**, 2451 (1999).

[52] J. Alitti *et al.*, UA2 Collaboration, "A Search for New Intermediate Vector Mesons and Excited Quarks Decaying to Two Jets at the CERN $p\overline{p}$ Collider," Nucl. Phys. **B400**, 3 (1993).

[53] F. Abe *et al.*, CDF Collaboration, "Search for New Particles Decaying to Dijets in $p\overline{p}$ Collisions at $\sqrt{s} = 1.8$ TeV," Phys. Rev. Lett. **74**, 3538 (1995).